**Department of Chemistry**

# Magnetite and its Galvanic Effect to the Corrosion of Carbon Steel under Carbon Dioxide Environments

**Emilyn Wai Lyn Chan**

**This thesis is presented for the Degree of**
**Doctor of Philosophy**
**of**
**Curtin University**

**December 2011**

# DECLARATION

To the best of my knowledge and belief this thesis contains no material previously published by any other person except where due acknowledgment has been made.

This thesis contains no material which has been accepted for the award of any other degree or diploma in any university.

Signature: …….

Date: ……...

# ABSTRACT

Carbon dioxide corrosion, which can cause premature failure of oil and gas pipelines, is an imperative health, safety and environmental issue in the oil and gas industry. Extensive studies have been conducted to understand the formation and role of iron carbonate scale, which is the most probable scale formation under $CO_2$ corrosion. This scale can be protective toward the carbon steel pipelines. However, many post failure studies and ex-situ corrosion product scale analyses have shown the presence of thick corrosion product scale that consists mainly of black magnetite scale. The formation of magnetite scales from carbon dioxide corrosion of oil and gas carbon steel pipelines at temperatures below 100$^{o}$C has not been studied or investigated comprehensively despite the fact that magnetite is often found in pipelines. The observation of rapid corrosion failures and the associated corrosion product scale on the ruptured pipelines has instigated this PhD research to determine the mechanism of the formation of corrosion product scale and the galvanic effect of the magnetite scale in causing an accelerated corrosion.

Consequently, the mechanism of the formation of corrosion product scale on carbon steel under anaerobic conditions was studied. Preliminary studies on the corrosion product scales were conducted in an autoclave at 150$^{o}$C. The morphology and the properties of the corrosion product scales were analysed using Raman spectroscopy, Scanning Electron Microscopy (SEM) and Energy Dispersive Spectroscopy (EDS). Ex-situ analysis showed that the scale formed in a pH 5.5 anaerobic brine solution saturated with a low partial pressure of carbon dioxide gas comprised a mixture of magnetite ($Fe_3O_4$) and iron carbonate ($FeCO_3$). Whereas, the scale formed under the same temperature and solution pH, but in the absence of carbonate or bicarbonate species, consists only of magnetite. However, results from ex-situ analysis cannot be relied upon to conclusively prove the state of the surface in-situ. Therefore, a jet impingement cell that incorporates the capability of applying electrochemical measurements was used as an autoclave. The autoclave tests were replicated with in-situ electrochemical monitoring in the jet impingement cell to study the corrosion process and the scale development. The test temperature was set at 80$^{o}$C to closely simulate the operating temperature in most oil and gas production fields. The

morphology of the scales was examined under a Field Emission Scanning Electron Microscope (FESEM) since the SEM was not able to resolve nanometer structures on the surface. The FESEM clearly resolved the porous lath-like structure of chukanovite ($Fe_2(OH)_2CO_3$), iron carbonate and ultrafine nanometer crystals on the scale surface formed under low partial pressure of carbon dioxide. On the other hand, the carbon steel surface, which was corroded in the absence of carbonate species at pH 5.5, was fully covered with nanometer crystalline magnetite that was only detectable under the FESEM. The identity of the iron compounds was confirmed using Synchrotron Radiation Grazing Incidence X-ray Diffraction (SR-GIXRD).

An in-situ SR-GIXRD study on the corrosion of carbon steel under low partial pressure of carbon dioxide gas was carried out, incorporating EIS. This combined approach showed a strong correlation of the phase development as detected on the SR-GIXRD to the electrochemical behaviour on the impedance spectra. The development of the porous chukanovite and magnetite was found in association with a higher corrosion rate of the carbon steel before the steel was passivated by the combined corrosion product scale. Both in-situ and ex-situ studies have shown that magnetite ($Fe_3O_4$) and chukanovite ($Fe_2(OH)_2CO_3$) are formed at the early stage of scale development via electrochemical and hydrolysis reactions in mildly acidic conditions before iron carbonate exceeds it solubility limit and precipitates rapidly over the carbon steel surface.

The galvanic effect of coupling the magnetite to carbon steel was studied. The coupling was found to cause galvanic corrosion of the carbon steel. The cathode to anode surface area ratio of the magnetite/mild steel couple and the solution pH, inter-related to the partial pressure of carbon dioxide, were investigated and found to be contributing factors to the rate of galvanic corrosion. The galvanic corrosion was cathodically controlled by magnetite. The self corrosion rate of the carbon steel was reduced with increasing pH but the galvanic corrosion rate did not seem to be affected by the high pH. This prompted the suggestion of the possibility of magnetite itself partaking in self reduction and contributing to the galvanic current.

Following the hypothesis that magnetite undergoes reductive dissolution in acidic carbon dioxide solution, studies were carried out to study on the reductive behaviour

of magnetite. Cyclic voltammetry was used to investigate the reductive-oxidative behaviour of magnetite at different solution pH. The results show that magnetite does undergo reduction when it is polarized cathodically. Ferric ion in the magnetite lattice reduces to ferrous ion that can diffuse from the solid lattice in acid solution or form hydroxide compounds. The semiconductivity of magnetite was investigated using the Mott-Schottky technique, illustrating a conversion from an n-type semiconductor to a p-type semiconductor when the magnetite was reduced cathodically.

In view of the galvanic effect from the magnetite scale, corrosion inhibitors that are commonly used to control carbon dioxide corrosion in the oil and gas industries were tested for their inhibition efficiency against this galvanic corrosion. Generic inhibitors as well as industrial formulated inhibitors were tested. Some inhibition was observed, but all materials failed to achieve a confidence level of at least 90% of inhibition efficiency.

# PUBLICATIONS

Chan, E., John, D., Bailey, S., & Kinsella, B. (2007). *Effect of corrosion product scale on galvanic carbon dioxide corrosion.* Paper presented at the Australasian Corrosion Association, Sydney.

Chan, E., John, D., Bailey, S., & Kinsella, B. (2008). *Galvanic corrosion of carbon steel in carbon dioxide caused by magnetite.* Paper presented at the 17th International Corrosion Congress, Las Vegas.

Chan, E., John, D., Bailey, S., Kinsella, B., & Nesic, S. (2009). *Formation of magnetite scale under anaerobic conditions at low temperatures.* Paper presented at the Australasian Corrosion Association, Coffs Harbour.

# ACKNOWLEDGEMENTS

I would like to express my sincere gratitude to my fellow supervisors, Dr. Douglas John and Dr. Stuart Bailey, for their constant guidance, patience, encouragement and support. Their strong faith in me has shifted my perception from that of an ordinary engineer to a scientist, who strives for details and perfection. I also like to acknowledge Adjunct Professor Brian Kinsella for creating many opportunities in the last four years for me to develop my skills and knowledge in the field of corrosion. I am indeed very grateful to him and Professor Srdjan Nesic for providing me the invaluable experience to work with their Corrosion group at the Ohio University.

My appreciation to Professor Roland De Marco for giving me the golden opportunity to use the Australian Synchrotron. I really appreciate the assistance of Professor Roland De Marco and Dr. Katerina Lepkova at the Synchrotron for making a great success in the development of a novel experiment. Also, a special thanks to Dr. Robert Hart from the Physics department for his help in operating the FESEM to achieve fantastic resolution at nanometer scale. I want to extend my gratitude to Dr. Marek Odziemkowski for his generosity in gifting his special Raman electrochemical cell to me which has enabled me to prove my hypothesis from the in-situ Raman analysis technique. I also want to thank Emeritus Professor Bill van Brownswijk, Peter Chapman and Professor Hugh Richardson for their technical support and assistance on their Raman instrument.

This PhD project was funded by the Curtin University Postgraduate Scholarship, along with the supplementary scholarship from the Western Australian Energy Research Alliance and Western Australian Corrosion Research Group.

Last and not least, I would like to thank my family for their everlasting love and moral support all these years.

Finally, this dissertation is my dedication to all of you who have always shown your care, understanding, love and moral support to me.

# TABLE OF CONTENTS

**DECLARATION** i

**ABSTRACT** ii

**TABLE OF CONTENTS** v

**PUBLICATIONS** viii

**ACKNOWLEDGEMENTS** ix

Chapter 1 Introduction ..... 1

1.1. Research aims and objectives ..... 3

Chapter 2 Formation of Corrosion Product Scales ..... 5

2.1. Introduction ..... 5

2.1.1. Corrosion product scales in oil and gas pipelines ..... 5

2.1.2. Properties of corrosion product scales ..... 11

2.1.2.1. Magnetite ($Fe_3O_4$) ..... 11

2.1.2.2. Iron carbonate ($FeCO_3$) ..... 13

2.1.2.3. Chukanovite ($Fe_2(OH)_2CO_3$) ..... 13

2.1.2.4. Ferrous hydroxide ($Fe(OH)_2$) ..... 15

2.1.2.5. Wustite (FeO) ..... 15

2.2. Experimental ..... 16

2.2.1. Ex-situ anaerobic autoclave test ..... 16

2.2.2. In-situ electrochemical autoclave test at 80$^oC$ ..... 18

2.2.3. In-situ SR-GIXRD incorporating EIS ..... 20

2.3. Results and Discussion ..... 23

2.3.1. Ex-situ anaerobic autoclave test ..... 23

2.3.1.1. Autoclave test at 150$^oC$ under low $P_{CO_2}$ ..... 23

2.3.1.2. Autoclave test at 150$^oC$ under $N_2$ ..... 26

2.3.1.3. Autoclave test at 80$^oC$ under low $P_{CO_2}$ ..... 28

2.3.2. In-situ electrochemical autoclave test ..... 29
2.3.2.1. Electrochemical autoclave test at 80°C under low $P_{CO_2}$ ..... 29
2.3.2.2. Electrochemical autoclave test at 80°C under $N_2$ ..... 41
2.3.3. In-situ SR-GIXRD study of scale development ..... 50
2.4. Conclusions ..... 61
Chapter 3 Galvanic Corrosion of Carbon Steel Caused by Coupling Magnetite ... 63
3.1. Introduction ..... 63
3.1.1. Galvanic corrosion ..... 63
3.1.2. Electronic properties of corrosion products ..... 64
3.1.3. Factors governing galvanic corrosion ..... 66
3.1.3.1. Carbon dioxide partial pressure ..... 67
3.1.3.2. Cathode to anode surface area ratio ..... 67
3.1.4. Inhibition of galvanic corrosion ..... 69
3.2. Experimental ..... 71
3.3. Results and Discussion ..... 73
3.3.1. Galvanic corrosion from magnetite ..... 73
3.3.1.1. Effect of cathode to anode surface area ratio ..... 73
3.3.1.2. Effect of carbon dioxide partial pressure ..... 77
3.3.2. Inhibition of galvanic corrosion ..... 80
3.3.2.1. Inhibition from generic inhibitors ..... 80
3.3.2.2. Inhibition from commercial inhibitors ..... 86
3.4. Conclusions ..... 89
Chapter 4 Reduction of Magnetite ..... 90
4.1. Introduction ..... 90
4.2. Experimental ..... 93
4.2.1. Electrochemical setup ..... 93
4.2.2. In-situ Raman setup ..... 94
4.3. Results and discussion ..... 97
4.3.1. Cyclic voltammetry study of the reductive-oxidative behaviour of magnetite under carbon dioxide ..... 97
4.3.1.1. Effect of carbonic acid ..... 97
4.3.1.2. Effect of acid ..... 100
4.3.1.3. Effect of bicarbonate species ..... 102

4.3.1.4. Reduction at high cathodic potential ..... 105
4.3.2. Effect of reduction on the semiconductor behaviour of magnetite .. 107
4.3.3. In-situ study of magnetite reduction ..... 113
4.3.4. Ex-situ study of magnetite reduction ..... 117
4.4. Conclusions ..... 120
Chapter 5 Conclusions ..... 121
5.1. Suggestions for further work ..... 122
Chapter 6 Reference List ..... 124

# CHAPTER 1 INTRODUCTION

Corrosion is a major concern in the oil and gas industry. Moreover, its link to disastrous explosions and oil spills as a result of ruptured pipelines, poses significant impact to health, safety, environment and economy. The Varanus Island explosion for example, is one of the most recent oil and gas catastrophes in Australia due to pipeline corrosion which has caused production loss and downtime to the operator company and also affected many domestic industries and production loss to the state's mining and processing industry. As a result of the explosion, there was more than 30% loss of capacity in Western Australia's gas supply (Fitzgerald, 2008).

Carbon dioxide corrosion is a common form of internal pipeline corrosion in the oil and gas industry. In 2002, a serious carbon dioxide corrosion problem occurred in one of Western Australia's biggest offshore oil platforms which resulted in premature pipeline failure (Weir, 2002). The root cause of such catastrophic event is often not disclosed until a series of lengthy investigations and failure analyses are carried out. In the end, the case is generally concluded as failure in corrosion control with limited information of the main factor causing the accelerated corrosion event. However, thick black scales are frequently seen in post failure analysis of the ruptured pipelines with minimum consideration of any association with the black scale that mainly consists of magnetite, not iron carbonate. Moreover, much modelling and simulation software predicts the formation of protective iron carbonate scale under field operating conditions but fails to clarify what has caused premature pipeline corrosion if iron carbonate scale is protecting the pipeline.

Figure 1-1 Magnetite scales on corroded carbon steel surfaces from the field.

The presence of magnetite scale, resulting in galvanic corrosion of carbon steel pipelines, has never previously drawn significant attention from the oil and gas industry. This is largely due to the fact that magnetite has always been thought of as an artefact of ex-situ examination of corrosion product scale upon retrieval from anaerobic operating conditions. Besides, a common perception is that magnetite may be formed from low levels of oxygen introduced into the system through the injection of treatment chemicals. Magnetite scale is inevitably present on pipelines either from mill scale or corrosion product scale. Although, mill scale can be removed by acid pickling and pigging operations, this practice is often not completed due to the additional costs and complexity. In addition, the formation of magnetite in oil and gas pipelines is poorly understood.

In the pressurized water reactor (PWR) industry, extensive studies show the formation of magnetite scale under high temperature, high pressure anaerobic environments and the subsequent galvanic corrosion of carbon steel (Al-Mayouf, 2006; Al-Mayouf, Al-Mobarak, & Al-Swayih, 2007; Allen, Hampson, & Bignold, 1978) since magnetite is electrically conductive and more noble than carbon steel in the electrochemical series. It is therefore conceivable that the presence of magnetite scale in oil and gas pipelines may also cause galvanic corrosion. However, there is very little literature in the scientific community to support the formation of magnetite scales under low temperature and low carbon dioxide partial pressure environments despite the fact that magnetite is often found on the internal walls of carbon steel pipelines from field applications in the oil and gas industry. For this reason, the mechanism of corrosion product scale formation and the associated corrosion behaviour was investigated in this work.

Carbon steel, despite being highly susceptible to corrosion, is widely used in the oil and gas industry, in preference to corrosion resistant alloys, due to economic reasons (López, Schreiner, De Sánchez, & Simison, 2004). The usage of carbon steel has engendered numerous challenges in the mitigation of oil and gas corrosion. One of the most cost effective methods in corrosion prevention is to employ chemical treatments by the injection of corrosion inhibitors (S. Ramachandran & V. Jovancicevic, 1999a). However, there are limitations to the chemical stability and compatibility with the operating conditions and environments. Most corrosion

inhibitors are specially formulated to target specific applications, but variations such as metal surface condition, galvanic couples and flow regimes associated with turbulence, droplet or particle impact might not be taken into consideration for general corrosion control. Therefore, the process of design, selection and evaluation of corrosion inhibitors is essential to achieve optimum inhibition efficiency in each application. Since the mechanism of galvanic corrosion from magnetite coupling can be different from general carbon dioxide corrosion, it is necessary to elucidate the factors causing the galvanic corrosion to initiate the development of superior corrosion inhibitors and/or methods to control the severe localized corrosion resulting from magnetite scales.

## 1.1. RESEARCH AIMS AND OBJECTIVES

Many oil and gas fields are experiencing a gradual drop in carbon dioxide partial pressure that is interrelated with the increase in solution pH due to the reduction of production rate in the production pipelines. With the variations in operating conditions, the corrosion rate of the carbon steel pipeline and the mechanism of the scale formation would be expected to change. Since magnetite is known for its galvanic effect on carbon steel corrosion, it is necessary to find out how corrosion product scales are formed and their influence on corrosion. Therefore the objectives of this PhD research are to:

- determine the mechanism of corrosion product scale formation under low partial pressure of carbon dioxide
- identify the constituents of the related corrosion products using different surface and chemical analyses
- deduce the mechanistic pathways to the formation of corrosion product scales based on thermodynamic calculations and compare with experimental results
- study the factors of cathode to anode surface area ratio that contribute to higher galvanic corrosion of the magnetite/carbon steel couple
- verify the occurrence of reductive dissolution of magnetite in acidic conditions and to determine the factors controlling the galvanic corrosion

- determine if the galvanic corrosion from magnetite coupling can be inhibited by generic inhibitors and commercially available inhibitors which have been commonly used in oil and gas carbon dioxide corrosion.

# CHAPTER 2 FORMATION OF CORROSION PRODUCT SCALES

## 2.1. INTRODUCTION

Corrosion product scales formed on carbon steel consist of various iron compounds depending on the conditions of the environment such as temperature, pressure, solution pH and dissolved anions in the fluid. Corrosion product scales can be formed during the manufacturing process of the steel under high temperature, which leaves a layer of black oxide scale known as mill scale. This mill scale consists of three layers of oxide: outermost hematite ($Fe_2O_3$) layer; intermediate magnetite ($Fe_3O_4$) layer and the inner wüstite (FeO) layer (Gleeson, Hadavi, & Young, 2000). The scale structure and composition is primarily dependent on temperature and oxygen level during its formation (Gleeson et al., 2000). However, the mechanism of the formation of corrosion product scales in anaerobic oil and gas production pipelines can be completely different due to the distinctive nature of the scale development reactions. The scale formation in the production pipelines is a wet corrosion process involving a direct reaction with an aqueous solution whereas the formation of the mill scale is via a high temperature dry corrosion reaction with gas. Since the oilfield corrosion is the focal point of this Ph.D. study, a comprehensive study on the development of wet corrosion product scales was carried out.

### 2.1.1. Corrosion product scales in oil and gas pipelines

Carbon dioxide corrosion plays a prominent role in oil and gas pipeline corrosion. The pressure in the reservoir varies with production rate and life. Often, the corrosiveness of the gas condensate well is related to the partial pressure of carbon dioxide as the solubility of carbon dioxide depends on temperature, pressure and the compositions of water (Farshad, Garber, & Polaki, 2000). The co-produced carbon dioxide gas in the oil and gas production pipelines reacts with the water phase to form carbonic acid and dissolved carbonate species via the following reaction pathways that are corrosive to the steel.

$$CO_{2(g)} \rightleftharpoons CO_{2(aq)}$$ Reaction 2-1

$$CO_{2(aq)} + H_2O_{(l)} \rightleftharpoons H_2CO_{3(aq)}$$ Reaction 2-2

$$H_2CO_{3(aq)} \rightleftharpoons H^+_{(aq)} + HCO^-_{3\,(aq)}$$ Reaction 2-3

$$HCO^-_{3\,(aq)} \rightleftharpoons H^+_{(aq)} + CO^{2-}_{3\,(aq)}$$ Reaction 2-4

Corrosion of ferrous metals is a redox reaction which primarily involves the oxidation of iron (Reaction 2-5) and the reductions of carbonic acid (Reaction 2-6 and Reaction 2-7) and hydronium ion (Reaction 2-8) under carbon dioxide environments. Carbonic acid, despite being a weak acid, is found to be several times more aggressive than strong mineral acids at the same pH (De Waard & Milliams, 1975b; Moiseeva, 2005). This anomaly is due to the combined reduction reactions of the carbonic acid and the hydronium ion.

$$Fe_{(s)} \rightarrow Fe^{2+}_{(aq)} + 2e^-$$ Reaction 2-5

$$2H_2CO_{3(aq)} + 2e^- \rightarrow H_{2(g)} + 2HCO^-_{3\,(aq)}$$ Reaction 2-6

$$2HCO^-_{3\,(aq)} + 2e^- \rightarrow H_{2(g)} + 2CO^{2-}_{3\,(aq)}$$ Reaction 2-7

$$2H^+_{(aq)} + 2e^- \rightarrow H_{2(g)}$$ Reaction 2-8

The extensive electrochemical pathways of iron dissolution were explained by Bockris (Bockris, Drazic, & Despic, 1961) but the subsequent process leading to the development of corrosion product scales is still ambiguous and sometimes the theories are conflicting. The development of corrosion product scales on carbon steel is known to depend on the operating conditions such as solution pH, temperature, carbon dioxide gas partial pressure, constituents in the formation water, dissolved oxygen level, hydrodynamics and the steel microstructure (Baboian, 1976b; Cabrini, Hoxha, Kopliku, & Lazzari, 1998). Owing to the variation in the conditions of the production wells, problems associated with corrosion in the pipelines as well as the corrosion product scales can be very different. In fact, ex-situ chemical analysis of the field samples often shows the presence of various types of corrosion products which may comprise akaganeite (FeOOH), magnetite ($Fe_3O_4$), cementite ($Fe_3C$), iron carbonate ($FeCO_3$) and calcium carbonate ($CaCO_3$) under different field conditions (Cabrini et al., 1998). However, analyses based on scanning electron microscopy

(SEM) and energy dispersive spectroscopy (EDS) of the corrosion product scales that are formed in the laboratory which closely simulate the oilfield conditions always report iron carbonate scale as the dominant corrosion product (Chokshi, Sun, & Nesic, 2005; Ruzic & Nesic, 2001; Ruzic, Veidt, & Nesic, 2006a, 2006b, 2007; Sun & Nesic, 2006, 2008). Many mechanistic models are derived to simulate the effect of temperature, pH, $Fe^{2+}$ concentration and carbon dioxide partial pressure on iron carbonate scale formation in the sweet corrosion process (Nesic & Lee, 2003; Nesic, Nordsveen, Nyborg, & Stangeland, 2003). Nonetheless, the advancement and improvement of technology has led to high resolution in-situ surface and chemical studies which can elucidate the progression of the scale development.

Fundamentally, the mechanism of corrosion product scale development still follows the basic theories of electrochemistry and chemistry. The foremost development process of the corrosion products begins with the dissolution of iron. Then, the ferrous ion undergoes hydration reaction. These processes have been described chemically and electrochemically. The chemists from the 1950's studied the hydration of cations and derived the hydration pathway of iron as follows leading to the formation of ferrous hydroxide, $Fe(OH)_2$ (Baes & Mesmer, 1976, 1981; Leussing & Kolthoff, 1953; Tremaine, Masscow, & Shierman, 1977).

$$Fe^{2+}{}_{(aq)} + H_2O_{(l)} \rightarrow FeOH^{+}{}_{(aq)} + H^{+}{}_{(aq)} \qquad \text{Reaction 2-9}$$

$$FeOH^{+}{}_{(aq)} + H_2O_{(l)} \rightarrow Fe(OH)_{2(s)} + H^{+}{}_{(aq)} \qquad \text{Reaction 2-10}$$

On the other hand, the electrochemists defined the hydration process from the electrochemical pathways of water adsorption on the steel surface which ended up having the same final product, $Fe(OH)_2$ (Bockris et al., 1961).

$$Fe_{(s)} + H_2O_{(l)} \rightarrow FeOH_{ads} + H^{+}{}_{(aq)} + e^{-} \qquad \text{Reaction 2-11}$$

$$FeOH_{ads} + H_2O_{(l)} \rightarrow Fe(OH)_{2,ads} + H^{+}{}_{(aq)} + e^{-} \qquad \text{Reaction 2-12}$$

$$Fe(OH)_{2,ads} + OH^{-}{}_{(aq)} \rightarrow HFeO^{-}_{2,ads} + H^{+}{}_{(aq)} + e^{-} \qquad \text{Reaction 2-13}$$

$$HFeO^{-}_{2,ads} + H_2O_{(l)} \rightarrow Fe(OH)_{2(s)} + OH^{-}{}_{(aq)} \qquad \text{Reaction 2-14}$$

Subsequent to the hydration reaction, it is proposed that the unstable $Fe(OH)^{+}$ species combines with the carbonate in equilibrium with carbonic acid to form the stable chukanovite, $Fe_2(OH)_2CO_3$ (Heuer & Stubbins, 1999; Rémazeilles & Refait, 2009):

$$2FeOH^{+}_{(aq)} + CO^{2-}_{3(aq)} \rightarrow Fe_2(OH)_2CO_{3(s)}$$ Reaction 2-15

The presence of chukanovite was first discovered in 1976 as a corrosion product scale by Erdös and Altorfer (Erdös & Altorfer, 1976) in a corroded water pipeline. Recently, this product was identified by De-Marco et al. (De Marco, Jiang, Pejcic, & Poinen, 2005) in an in-situ synchrotron radiation grazing incidence x-ray diffraction (SR-GIXRD) study of carbon dioxide corrosion on carbon steel. Throughout the 24 hours experiment, the x-ray diffraction patterns showed essentially the formation of chukanovite and no other corrosion products.

Apart from the formation of stable chukanovite, the transformation of the metastable hydroxide to magnetite has been reported in the anaerobic Fe-$H_2O$ corrosion system (Castle & Mann, 1966; Cornell & Schwertmann, 1996). This reactive hydroxide phase tends to transform to a thermodynamically stable compound. The prediction of corrosion behaviour of systems such as Fe-$H_2O$ is often represented graphically on a potential-pH diagram as shown in Figure 2-1.

If the pH and potential fall in the region of stable magnetite according to the pH-potential diagram, either the ferrous ion or the metastable ferrous hydroxide can be oxidised to magnetite via the Schikorr reactions (Baes & Mesmer, 1976; Bignold, Garnsey, & Mann, 1972; Lee, Odziemkowski, & Shoesmith, 2006):

$$3Fe(OH)_{2(s)} \rightleftharpoons Fe_3O_{4(s)} + H_{2(g)} + 2H_2O_{(l)}$$ Reaction 2-16

$$3Fe^{2+}_{(ads)} + 4H_2O_{(l)} \rightleftharpoons Fe_3O_{4(s)} + 8H^{+}_{(aq)} + 2e^{-}$$ Reaction 2-17

This transformation was observed in an in-situ surface enhanced Raman study of anaerobic iron oxidation in water under nitrogen atmosphere, from 22$^{o}$C to 288$^{o}$C by Kumai and Devine (Kumai & Devine, 2005). The test results showed a broad ferrous hydroxide peak at 550 cm$^{-1}$ was observed at the initial stage as the autoclave was heating up. The broad peak suggests that the layer was not crystalline but could be amorphous. As the temperature continued to rise to 75$^{o}$C, the hydroxide peak disappeared and the magnetite peak at around 660 cm$^{-1}$ appeared on the Raman spectra. Magnetite was the only product detected as the autoclave continued to heat up to 288$^{o}$C. Moreover, the presence of magnetite has been discovered in either high

pH (Peulon, Antony, Legrand, & Chausse, 2004) or high temperature carbon dioxide corrosion (Videm & Dugstad, 1989).

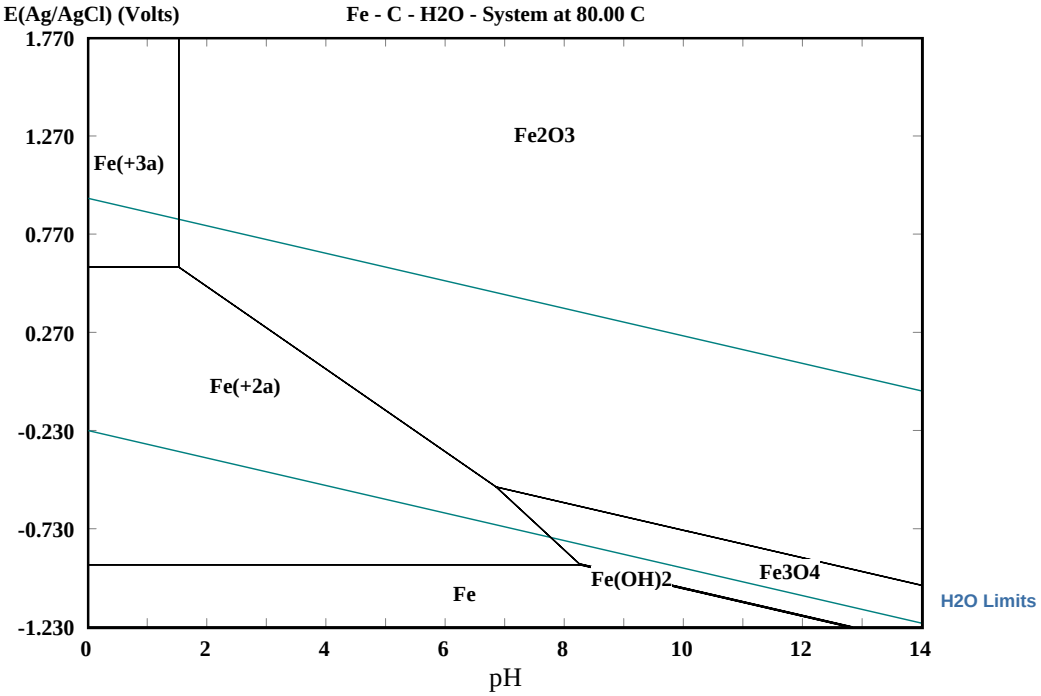


Figure 2-1 Potential-pH diagram for Fe-$H_2O$ system at 80°C, generated by HSC Chemistry software.

Subsequent to the hydration and electrochemical reactions, an extended corrosion process leads to the precipitation of iron carbonate when the concentration of $Fe^{2+}$ and $CO_3^{2-}$ ions at equilibrium exceed the solubility product limit of iron carbonate.

$$Fe^{2+}_{(aq)} + CO_3^{2-}{}_{(aq)} \rightleftharpoons FeCO_{3(s)} \qquad \text{Reaction 2-18}$$

$$K_{sp} = [Fe^{2+}][CO_3^{2-}] \qquad \text{Equation 2-1}$$

The solubility of iron carbonate is temperature dependent and the value of the solubility product, $K_{sp}$ decreases with increasing with temperature. The solubility product of iron carbonate can be predicted using the empirical model derived by Braun (Braun, 1991) in Equation 2-2 which is well correlated to the theoretical thermodynamics calculations. This predictive temperature dependent model gives the estimation of the solubility product of iron carbonate in the temperature range of 30°C to 80°C:

$pK_{sp} = 0.0314T + 10.20$ Equation 2-2

Where T is temperature expressed in degree Celsius.

Studies of carbon dioxide corrosion have found that the formation of a protective iron carbonate scale depends on the nature of the base alloy (composition and microstructure of the metal) and the condition of the environment such as temperature, pH, $Fe^{2+}$ concentration, $CO_2$ partial pressure and flow velocity (López, Pérez, & Simison, 2003; Moiseeva, 2005). Besides, the availability of the carbonate species is essentially a function of temperature and pH according to the carbon dioxide equilibria in Reactions 2-2 to 2-4. Therefore the precipitation reaction to form a protective iron carbonate scale is highly dependent on temperature and pH. An elevated temperature increases the kinetics of the precipitation reaction due to lower solubility of the iron carbonate; an increase in pH shifts the equilibrium of Reaction 2-4 to the right, forming more carbonate ions for the precipitation reaction. Moreover, studies have found that a dense and protective iron carbonate scale can be achieved at temperature range of 60$^{o}$C to 90$^{o}$C (Nesic et al., 2003) and pH range of 6 to 8 (Videm & Dugstad, 1989). The iron carbonate formation from a Fe-$CO_2$-$H_2O$ system can also be represented on pH-potential diagram shown in Figure 2-2.

The corrosion rate of carbon steel depends primarily on solution pH and temperature according to the predictive model derived by DeWaard and Milliams (De Waard & Milliams, 1975a). The microstructure of carbon steel can also play a significant role in the corrosion process. Carbon steel microstructure consists of the ferrite ($\alpha$-Fe) and the pearlite (lamellar structure containing cementite, $Fe_3C$ with some $\alpha$-Fe) phase. When the steel is corroding at a high corrosion rate, the ferrite phases dissolves out, and would leave behind the $Fe_3C$ layer from the pearlite phases. This $Fe_3C$ layer accumulates on the surface as the corrosion process continues (Mora-Mendoza & Turgoose, 2002).

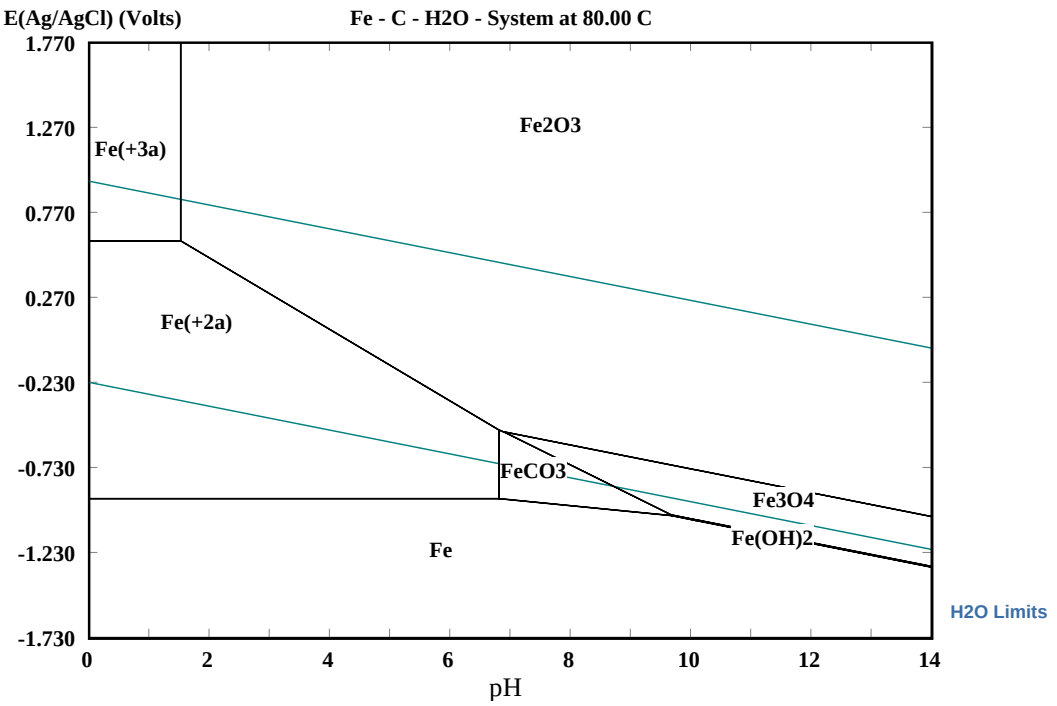


Figure 2-2 Potential-pH diagram for Fe-$CO_2$-$H_2O$ system at 80°C, generated by HSC Chemistry software.

### 2.1.2. Properties of corrosion product scales

Corrosion product scales contain a variety of iron compounds with unique structure, physical and chemical properties. The unique properties of an iron compound can influence the corrosion reaction. Hence, the crystal structures of iron compounds that are likely to be formed under anaerobic carbon steel carbon dioxide corrosion such as magnetite, iron carbonate, ferrous hydroxide, chukanovite and wustite are reviewed.

#### 2.1.2.1. Magnetite ($Fe_3O_4$)

Magnetite is an oxide which contains iron in both ferrous and ferric states. It falls into the mineral class of spinel (general formulation of $A^{2+}B^{3+}{}_2O^{2-}{}_4$) in which Fe ions of different oxidation states are coordinated octahedrally and tetrahedrally with the oxide anions and crystallized in a cubic spinel crystal system (space group Fd3m) (Weller, 1994). There are two types of spinel structures which are either normal

spinel or inverse spinel. The type of spinel is governed by the stabilized state of the transition metals present. This stabilized energy is termed the crystal field stabilisation energy (CFSE). In the normal spinel structure, the cubic closed-packed oxide consists of one octahedral and two tetrahedral sites per oxide. The $A^{2+}$ ions occupy $1/8^{th}$ of the tetrahedral holes and the $B^{3+}$ ions occupy half of the octahedral holes because of the charge factor to maximise the lattice energy. Magnetite is however formed in an inverse spinel structure because the $Fe^{2+}$ ($A^{2+}$) ions of $d^6$ high spin have greater CFSE in the octahedral sites (17 kJ $mol^{-1}$), the $Fe^{2+}$ ions force their way into the octahedral sites and displace part of the $Fe^{3+}$ ($B^{3+}$) ions to the tetrahedral site. Since $Fe^{3+}$, as a high spin ion, contains an electron in each of the d-orbitals, it produces zero CFSE for both octahedral and tetrahedral coordination, it has no preference for either type of coordination (Weller, 1994). Therefore, the tetrahedral site is occupied nominally by $Fe^{3+}$, while the octahedral sites are occupied by equal numbers of randomly distributed $Fe^{3+}$ and $Fe^{2+}$ ions (Wenzel & Steinle-Neumann, 2007).

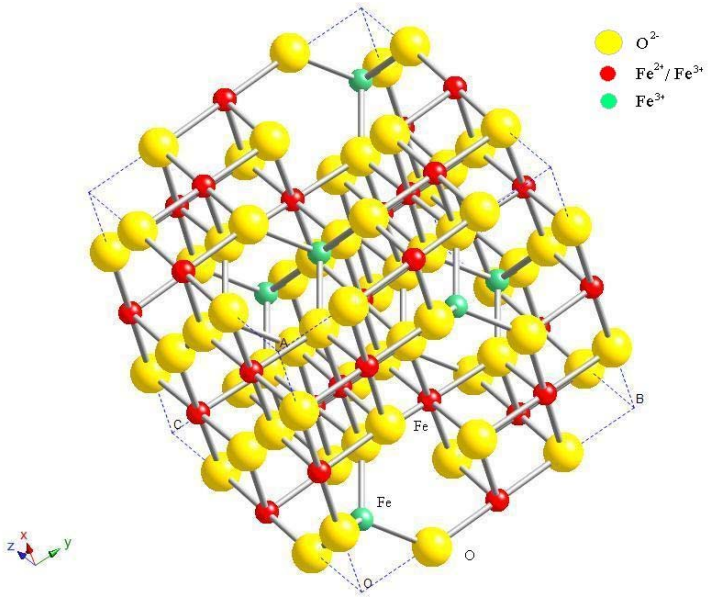


Figure 2-3 Crystal structure of $Fe_3O_4$ generated by CrystalMaker® software. $Fe^{3+}$ and $Fe^{2+}$ ions occupy the octahedral (red) sites; $Fe^{3+}$ ions occupy the tetrahedral (green) sites; $O^{2-}$ ions occupy the cubic (yellow) sites.

Magnetite in its magnetically ordered phase is ferrimagnetic with its magnetic moments of all the octahedral sites aligned in one direction and those on the tetrahedral sites in the opposite direction (Weller, 1994). The charge transfer of electrons from $Fe^{2+}$ in the lower valence state to $Fe^{3+}$ in the higher state in the d-d

orbitals transition which involves the absorption of light energy in the visible region resulting in the dark intense black colour of magnetite (Schwertmann & Cornell, 1991).

### 2.1.2.2. Iron carbonate ($FeCO_3$)

Iron carbonate has a well defined crystalline rhombohedral structure as shown in Figure 2-4 (Hirnyi, 2001). The colour of pure iron carbonate in its precipitate form is light gray to brown with a yellowish tint. Whereas, the iron carbonate formed as a corrosion product scale is dark greyish to black in colour. The colour difference of the electrochemically formed iron carbonate scale could be caused by the reflection of a thin external layer which is chemically different from iron carbonate as hypothesized by Hirnyi (Hirnyi, 2001).

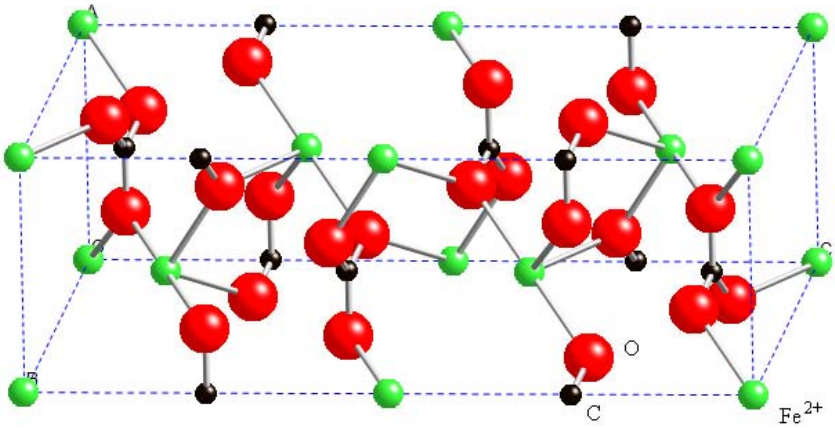


Figure 2-4 Crystal structure of $FeCO_3$ generated by CrystalMaker® software.

### 2.1.2.3. Chukanovite ($Fe_2(OH)_2CO_3$)

Ferrous hydroxide carbonate, $Fe_2(OH)_2CO_3$ also known as chukanovite was first discovered as a corrosion product scale by Erdös and Altorfer (Erdös & Altorfer, 1976). There is limited literature on this product and still not many corrosion scientists are aware of its existence. Chukanovite was found recently as a preliminary corrosion product on carbon steel under carbon dioxide corrosion on an in-situ synchrotron grazing incidence x-ray diffraction (SR-GIXRD) (De Marco et al., 2005). The structure of this corrosion product as shown in Figure 2-5 appears to be

acicular to fibrous. The aggregates are usually porous and brittle. The colour of the aggregates varies from brownish-green to brown with yellowish streak (Pekov et al., 2007).

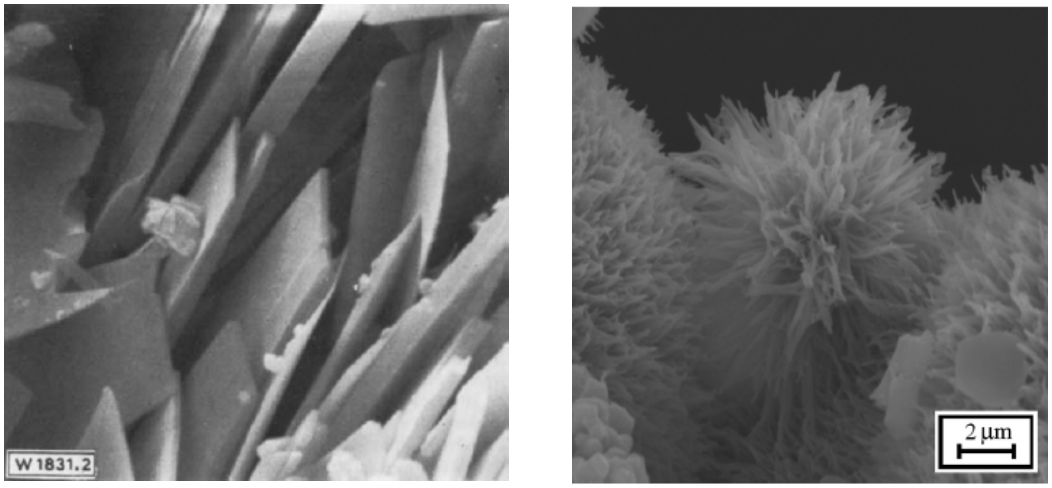


Figure 2-5 SEM image of Chukanovite obtained from Erdös (Erdös & Altorfer, 1976) and Pekov (Pekov et al., 2007).

The structure type of this chukanovite was categorised in the group of rosasite-malachite. The crystal structure of chukanovite is simulated based on the crystallography data obtained from Pekov et al. (Pekov et al., 2007) and presented in Figure 2-6. Since the recognition of this geological mineral or corrosion product is fairly new, there is still no thermodynamics data reported in the literature. The simulated unit cell structure does not show a well-defined crystalline structure and may suggest that chukanovite grows laterally in a plane direction.

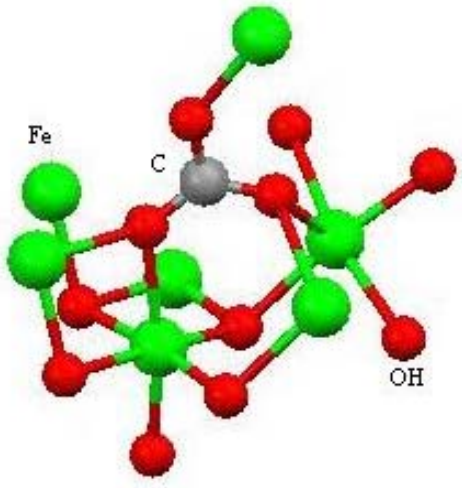


Figure 2-6 Crystal structure of $Fe_2(OH)_2CO_3$ generated by Mercury 2.3 software.

### 2.1.2.4. Ferrous hydroxide ($Fe(OH)_2$)

Ferrous hydroxide does not exist as a mineral but it can be synthesized chemically or electrochemically. At room temperature, $Fe(OH)_2$ is paramagnetic in which magnetism only occurs in the presence of an externally applied magnetic field. $Fe(OH)_2$ has a layer structure similar to brucite which is based on hexagonal anion packing with the cation in the divalent state as shown in Figure 2-7 (Cornell & Schwertmann, 1996). $Fe(OH)_2$ is relatively unstable in air and readily oxidised to green rust which appears to be greenish-blue and further oxidation will transform it into black magnetite (Cornell & Schwertmann, 1996).

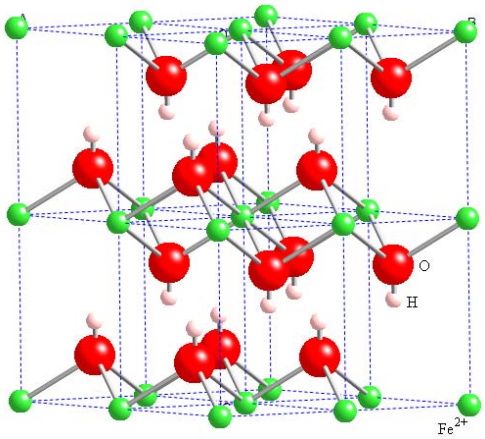


Figure 2-7 Crystal structure of $Fe(OH)_2$ generated by CrystalMaker® software.

### 2.1.2.5. Wustite (FeO)

Wustite is normally present in mill scale. Wustite is metastable at room temperature and it is formed only at high temperature and quenched to room temperature so that the iron and oxygen atoms are locked into the $Fe_{1-x}O$ structure (Weller, 1994). It has a defective NaCl structure consisting of two interpenetrating face-centered cubic structrures of $Fe^{2+}$ and $O^{2-}$ as shown in Figure 2-8 (Cornell & Schwertmann, 1996).

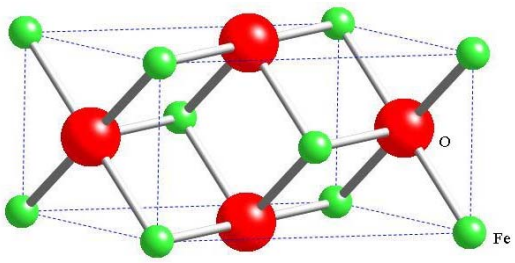


Figure 2-8 Crystal structure of FeO generated by CrystalMaker® software.

## 2.2. EXPERIMENTAL

### 2.2.1. Ex-situ anaerobic autoclave test

The study of the corrosion product scales on the X-65 carbon steel coupon was carried out by corroding the coupon in a deaerated brine solution containing 10 g/L of NaCl in deionised water under anaerobic conditions at 150$^{o}$C in a 316 stainless steel autoclave that was electrically isolated from the coupon. The autoclave was filled with 250 mL of brine solution and purged with nitrogen for an hour. An X-65 carbon steel coupon with the surface area of 9.8 cm$^{2}$ was used because it is a common grade used in the oil and gas industry. The sample coupon was bead blasted with 60 μm glass beads to remove the oxide layer on the coupon surface. The coupon was then polished with 600 grit SiC paper, rinsed and ultrasonically cleaned with iso-propanol for one minute. The coupon was then dried in nitrogen gas before inserting into the deaerated brine solution in the autoclave.

The nitrogen gas was kept purging while placing the X-65 carbon steel coupon together with the plastic coupon mount which provided electrical isolation from the stainless steel autoclave body into the autoclave, with the coupon fully submerged in the brine solution. Once the coupon was in place, the autoclave was then secured and deaeration with nitrogen continued for another 15 minutes. The autoclave was then pressurised and depressurised 3 times with nitrogen to make sure that any oxygen that could have introduced into the autoclave during coupon insertion was removed. Then, 0.17 bar of carbon dioxide gas was injected into the autoclave, followed by an addition of 1.55 bar of nitrogen gas. The pressure of the autoclave was held at a total pressure of 1.72 bar for five minutes. The injection valve of the autoclave was then sealed and the autoclave was placed in the heater, and held at 150$^{o}$C for 48 hours.

After 48 hours, the autoclave was cooled to 50$^{o}$C and then the coupon sample was removed and rinsed with deoxygenated deionised water followed by iso-propanol. The coupon was then dried with nitrogen gas and preserved in a desiccator before performing chemical and morphology analysis using the SEM/ EDS and Raman spectroscopy techniques.

The test was repeated with the same brine solution containing 10 g/L NaCl but with pH adjusted to 4.6 with the addition of hydrochloric acid (HCl) and the autoclave was pressurised with $N_2$ gas only to 1.72 bar without $CO_2$. The third test was done under nitrogen purge at atmospheric conditions at 80$^o$C. The general conditions of the tests are summarised in Table 2-1. The total gas pressure was kept constant at 1.72 barg in the autoclave before being heated up. Once each test was heated up to the test temperatures at 150$^o$C and 80$^o$C, the solubility of $CO_2$ in the liquid phase decreased as the temperature rose. The $CO_2$ partial pressures at test temperatures were not measurable but the solution pH was calculated from its $CO_2$ solubility at 80$^o$C and 150$^o$C with the value of 4.55 and 4.75 respectively.

Table 2-1 Autoclave test matrix

| Test No. | T ($^o$C) | *$PCO_2$ (barg) | *$PN_2$ (barg) | Vessel | Solution |
|---|---|---|---|---|---|
| 1 | 150 | 0.17 | 1.55 | Autoclave | 10 g/L NaCl |
| 2 | 150 | - | 1.72 | Autoclave | 10 g/L NaCl (pH adjusted to 4.6 with the addition of 0.1 M HCl |
| 3 | 80 | 0.17 | 1.55 | Autoclave | 10 g/L NaCl |

*Pressure measured at atmospheric temperature before the autoclave was heated up to test temperature.

Raman spectra were obtained using the UHTS300 Raman spectroscopy system. Excitation was provided by a frequency doubled Nd:YAG laser with the wavelength of 532 nm through a Plan 100x Nikon objective lens mounted on the WiTec Raman/near-field scanning optical microscope. The incident laser power output on the analysed surface was maintained below 0.5 mW as magnetite is sensitive to laser heating and transforms to hematite through the common phenomenon known as martilization (De Faria, Silva, & De Oliveira, 1997; Odziemkowski, Flis, & Irish, 1994). The spectrometer was operated by using the 1800 g/mm gratings. Data acquisition was obtained using the WiTec Scan Control Spectroscopy Plus software.

### 2.2.2. In-situ electrochemical autoclave test at 80°C

The study of the corrosion product scales formed on the X-65 carbon steel was carried out in the Jet Impingement Cell (JIC) under stagnant conditions (D. John, Kinsella, Bailey, & De Marco, 2003). The jet impingement cell was used because it has the capability to apply electrochemical measurements on the carbon steel surface in the cell under pressure. A silver/silver chloride (Ag/AgCl) reference electrode was installed in the JIC. The body of the JIC was used as a counter electrode. A carbon steel stub was coated with a non conductive cathodic polymer coating. The top surface of the coating was then ground off with 600 grit SiC paper, leaving an exposed steel surface area of 1.78 $cm^2$. The stub was then polished with 1200 grit SiC paper on a polishing machine. The stub was rinsed with milliQ water followed by ethanol, dried with nitrogen and stored in a dessicator.

A brine solution containing 30 g/L of NaCl and 0.1 g/L of $NaHCO_3$ in MilliQ water was prepared. The JIC was filled with 1.5 L of the standard brine solution and deaerated with the carbon dioxide / nitrogen gas mixture which was produced by adjusting the flow rate of the respective gases to 1: 10 ratio using an Allborg gas flow meter. The solution was deaerated and allowed to equilibrate for at least 2 hours. The pH of the solution was measured using a pH meter and the pH was maintained at pH 5.5 by gently regulating the proportion of the $N_2$ and $CO_2$ gas flow. The dissolved oxygen (DO) level in the system was monitored using an Orbisphere dissolved oxygen meter (model 3655) from the gas outlet through the JIC. The solution was sparged for 2 hours with recirculation of the fluid in the JIC with the pump operating to ensure full deaeration in the JIC. Once the DO level dropped below 0.8 ppb, the pump was changed to a reverse pumping mode to reduce the fluid level in the jet compartment to avoid fluid splashing out of the JIC during the change over of the electrode. The pump was then turned off. The plug in the electrode socket was quickly replaced with the previously prepared disc electrode. A pre-check of the electrochemical system was conducted by measuring the open circuit potential (OCP), linear polarisation resistance (LPR) and electrochemical impedance spectroscopy (EIS) on a PAR 263A/99 potentiostat. After confirming a smooth run in the system, the gas outlet was then sealed off, followed by the gas inlet, leaving 1 barg pressure of gas in the cell and the DO level maintained below 0.8 ppb so when

the test was heated up, the anticipated DO level in the system will be lower than 0.8 ppb as the solubility of $O_2$ decreases with temperature increase. The JIC was then heated up to 80$^{o}$C and allowed to run the test for 40 hours.

The open circuit potential was measured every 30 minutes followed by LPR and EIS. The potential range used for LPR measurement was ±10 mV versus open circuit potential and at a scan rate of 0.125 mV/s and the EIS measurement used an AC potential of 5 $mV_{rms}$ applied over a frequency range from 10 kHz 0 to 0.01 Hz. Data collection and instrument control were achieved using the Scribner software, Corrware and Zplot.

After 40 hours, the test was stopped and the coupon was removed from the JIC. The coupon was rinsed with deaerated milliQ water, which had been deaerated with nitrogen for an hour, to remove any salt from the test solution. The coupon was dried immediately with nitrogen and stored in a dessicator for surface and chemical analysis by the Neon® 45 field emission scanning electron microscope (FESEM), Raman spectroscope and Synchrotron radiation grazing incidence x-ray diffraction (SR-GIXRD).

The test was repeated in the absence of carbonate using a brine solution containing only 30 g/L of NaCl, to identify differences in the scale composition and corrosion mechanism. The solution was adjusted to pH 6 with the addition of 0.1 M hydrochloric acid (HCl) and deaerated with $N_2$ gas only.

### 2.2.3. In-situ SR-GIXRD incorporating EIS

The in-situ SR-GIXRD and electrochemical study of the carbon steel corrosion in mildly acidic carbon dioxide was performed on the Powder Diffraction Beamline at the Australian Synchrotron in Melbourne, Australia. A double crystal monochromator with interchangeable double Si(111) flat crystal pair was employed to deliver a wavelength of 1.000 Å. A specially designed GIXRD electrochemical flow cell as shown in Figure 2-9 was used (Veder et al., 2010). Silver/silver chloride (Ag/AgCl) was used as the reference electrode, which was inserted into the fluid compartment of the flow cell. Five platinum counter electrodes were placed at the periphery of the flow cell. An X-65 carbon steel working electrode with an exposed surface area of 2.58 $cm^2$ was housed in the centre of the cell. The electrodes were connected to an EG&G PAR 273A potentiostat.

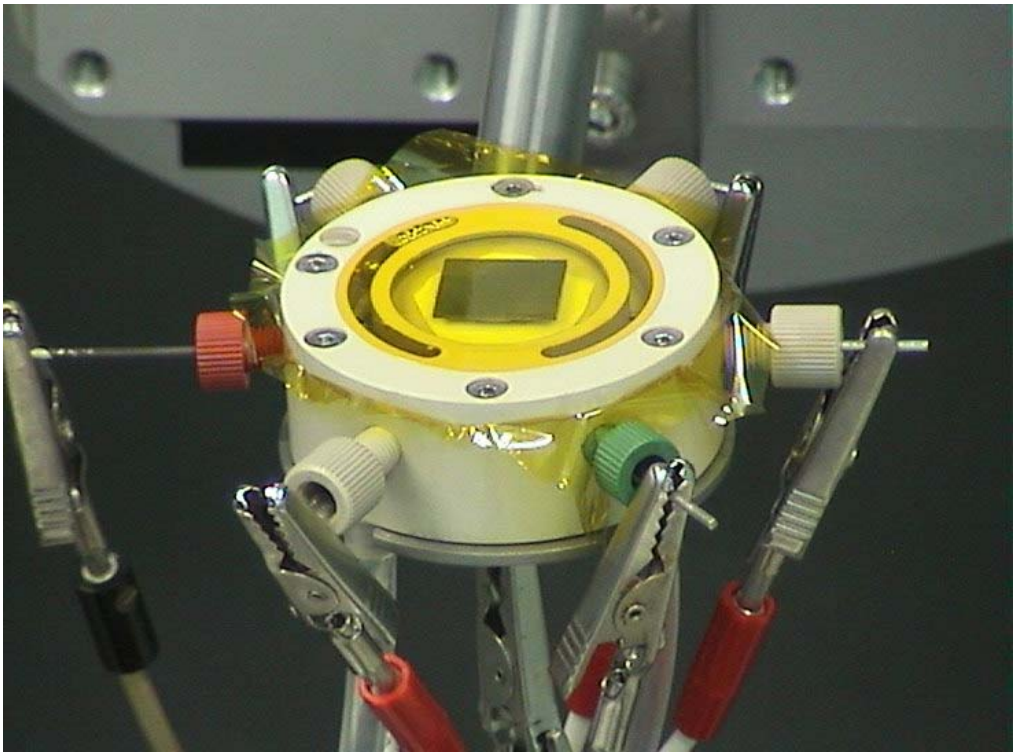

Figure 2-9 GIXRD electrochemical flow cell (Veder et al., 2010).

The complete experimental setup is shown in Figure 2-10. A special glass cell was filled with 0.2 L of standard brine solution containing 30 g/L of NaCl and 0.1 g/L of $NaHCO_3$. The electrolyte reservoir was deaerated for 2 hours with carbon dioxide / nitrogen gas mixture which was produced by proportioning the flow rate of the

respective gases in 10 to 60 graduations on the Allborg gas flow meter. Tubing for fluid recirculation (Tygon 2275) into the GIXRD electrochemical cell was attached to the reservoir. The solution pH was maintained at pH 6 by carefully adjusting the flow rate of the carbon dioxide gas. The solution was maintained at 45$^{o}$C using a temperature feedback control hotplate as the maximum operating temperature of the high purity, plasticizer free and low oxygen permeability Tygon 2275 tubing was limited to 45$^{o}$C.

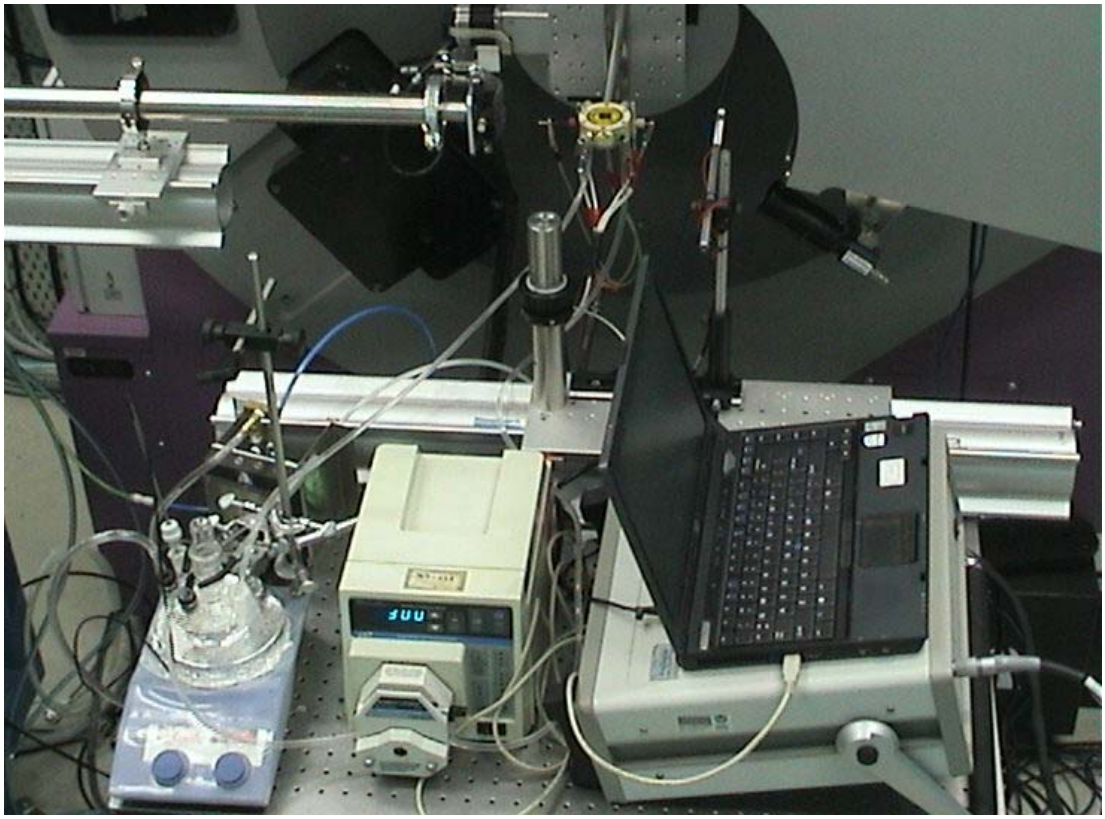

Figure 2-10 Experimental setup for in-situ GIXRD incorporating EIS of carbon steel corrosion in a standard brine solution at 45$^{o}$C under low partial pressure of $CO_2$ (pH 6).

The X-65 carbon steel electrode was inserted in the GIXRD electrochemical cell and mounted on the diffractometer. A serial alignment of the sample positioning was carried out to optimise the diffraction signal from the blank carbon steel. Once the optimum alignment was achieved, a 20 μm thick kapton window was attached to the cell to seal off the cell completely. Diffraction data were then obtained of the sample with the kapton window in place.

Once the detector was properly aligned, the tubing, which was deaerated together with the reservoir system, was then attached to the cell and the Masterflex peristaltic pump and pumped at a speed of 300 rpm. Electrochemical measurements were started immediately with an open circuit potential measurement for 30 minutes followed with EIS measured in a frequency of 10 kHz to 0.01 Hz and perturbation amplitude of ±5 mV. Upon completion of an EIS measurement, the pump was stopped and the SR-GIXRD data was obtained on the carbon steel at an incidence angle of $0.5^{o}$ with data collection time of 20 minutes. The pumping was resumed after the collection of x-ray diffraction pattern. The measurement steps were repeated except that every fifth hour, a depth profiling of the corroding surface was acquired at incidence angles of 0.5°, 0.85°, 1.85° and 3.85°. The beam size in the vertical direction was continuously altered at the different angles of incidence to ensure a constant beam footprint size of 11.459 mm. The corrosion test monitoring was continued for 25 hours.

## 2.3. RESULTS AND DISCUSSION

Ex-situ surface analysis results based on SEM and EDS results are often not conclusive to identify different iron products in the corrosion product scales. EDS is good for elemental analysis but it cannot provide definitive identification of the compound. Therefore, additional techniques such as Raman spectroscopy and SR-GIXRD, incorporating with EIS were adopted in this research to provide detailed information of the corrosion product scale composition and to elucidate the scale development process.

### 2.3.1. Ex-situ anaerobic autoclave test

#### 2.3.1.1. Autoclave test at 150$^{o}$C under low P $CO_2$

An ex-situ study of the corrosion product scale formed on the X-65 carbon steel coupon at 150$^{o}$C under low partial pressure of $CO_2$ was conducted. The composition and morphology of the scale were examined under the SEM together with EDS. The secondary electron (SE) mode on the SEM provides better resolution of the crystal structure for morphology study. Whereas, the phase variations of the scale were imaged using backscattered electron (BSE) mode which allows the identification of any compositional difference of the corrosion product scales based on the contrast caused by variations in the atomic density. The BSE image together with the elemental analysis from EDS is shown in Figure 2-11a and Figure 2-11b, illustrating two different types of chemical compounds. EDS confirmed that the brighter, smaller crystals produce peaks due primarily to Fe, O and relatively low C peaks in comparison to the O intensity. The darker, larger crystals have similar elemental composition as detected by EDS but with a higher relative intensity in the C peak. These EDS results suggest that the smaller crystals could be magnetite whereas the larger crystals could be iron carbonate. However, these compounds cannot be accurately confirmed by EDS alone, as the detection window of EDS limits the detection of any elements with the atomic weight lower than boron. Hence, EDS cannot verify the presence of hydrogen, and so the presence of $Fe(OH)_2$ and $Fe_2(OH)_2CO_3$ could not be accurately identified.

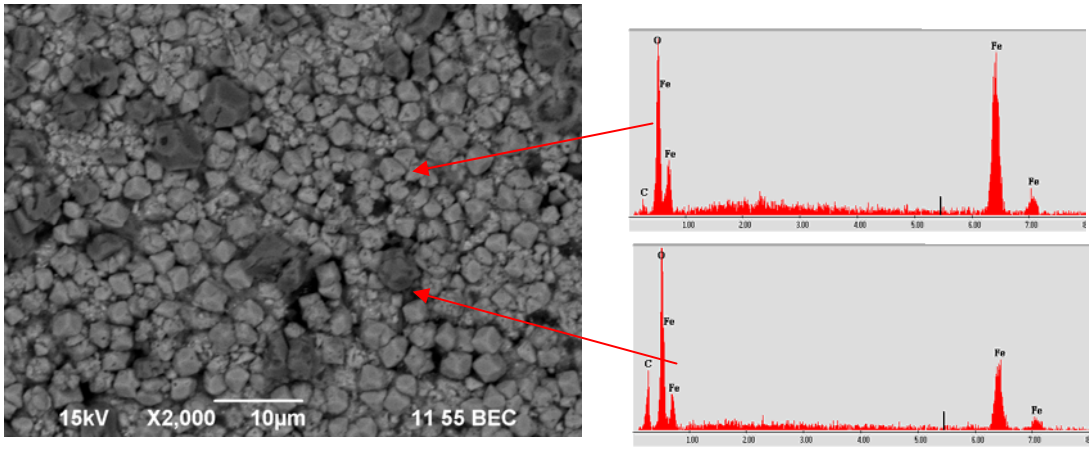


a) b)

Figure 2-11 (a) BSE image and (b) EDS spectra of the scale sample formed at 150°C.

In order to confirm the identity of the chemical compounds in the scale sample, Raman spectroscopy was adopted to identify the compounds by obtaining the vibrational mode that is specific to the chemical bonds in molecules. The optical microscope image in Figure 2-12a clearly shows the presence of two different sizes of crystals in the scale. The smaller crystals had greater reflections of light under the light microscope and they were at a deeper depth of focus.

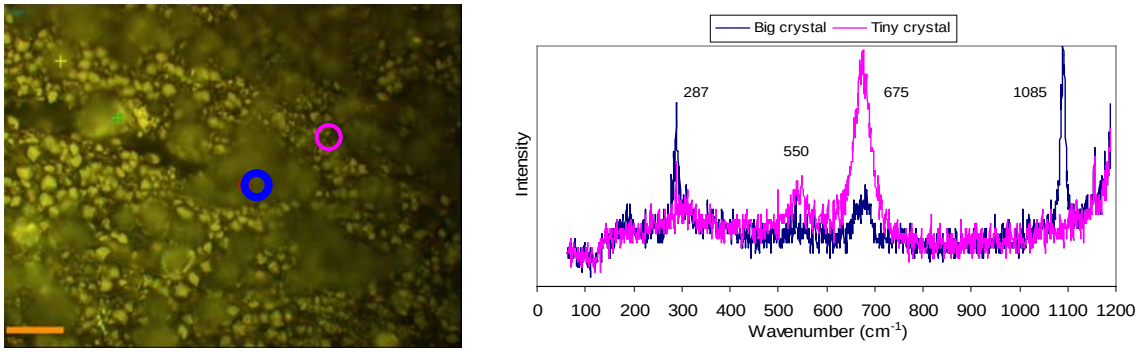


a) b)

Figure 2-12 a) Raman optical image (on 10 µm scale bar) and b) Raman spectra of the crystals formed in autoclave at 150°C with $CO_2$.

The Raman spectra from the small crystals as shown in Figure 2-12b had peaks at 675, 550 and 298 $cm^{-1}$ and no carbonate stretch was detected. The main peak at 675 $cm^{-1}$ is the characteristic Fe-O symmetric stretch of magnetite. There is literature that suggest the stretches at 298 and 550 $cm^{-1}$ are the asymmetric bend of Fe-O and

could also be the $A_1$ mode of Fe-OH symmetrical stretch of $Fe(OH)_2$ (Gui & Devine, 1991; Thanos, 1986). Therefore, the assignment of the 550 $cm^{-1}$ stretch suggests that $Fe_3O_4$ and / or $Fe(OH)_2$ may be present in the scale.

The larger crystals, on the other hand, showed the characteristic internal modes of $CO_3^{2-}$ showing the strongest symmetric stretching mode at 1085 $cm^{-1}$ and the external lattice vibrational modes at 192 $cm^{-1}$ and 287 $cm^{-1}$ (Lee, Odziemkowski, & Shoesmith, 2006). Low intensity magnetite and ferrous hydroxide spectra were also observed. The Raman results have clearly confirmed that both iron carbonate and magnetite are present in the corrosion product scale, as suggested by EDS. However, the presence of ferrous hydroxide could not be conclusively ascertained as the characteristic OH stretch at 3600 $cm^{-1}$ was excluded in the detection range because the Raman technique is highly sensitive to the presence of moisture and it was difficult to differentiate the influence of moisture on the specimen.

As iron carbonate, magnetite and possibly ferrous hydroxide were identified in the scale, the growth of the crystals was also studied by examining the morphology of the scale as shown in Figure 2-13 and Figure 2-14. Images of the scale were taken in both BSE and SE mode. The BSE image (Figure 2-13a and Figure 2-14a) conveys the impression of the inclusion of the larger iron carbonate crystals between the magnetite crystals. However, when the morphology was examined under the SE mode (Figure 2-13b and Figure 2-14a), it showed that iron carbonate crystals were lying on top of the magnetite.

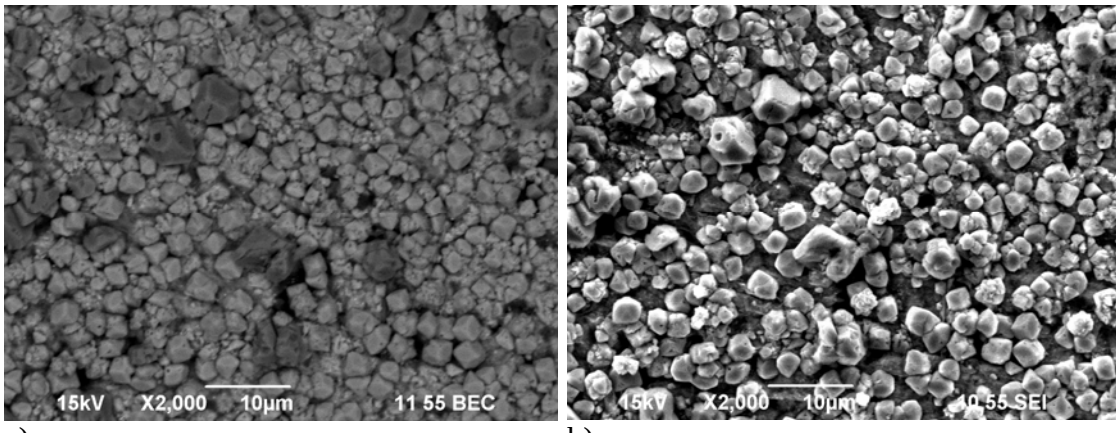


a) b)

Figure 2-13 a) BSE and b) SE micrographs at 2000 times magnification of scaled coupon from autoclave test at 150$^{o}$C.

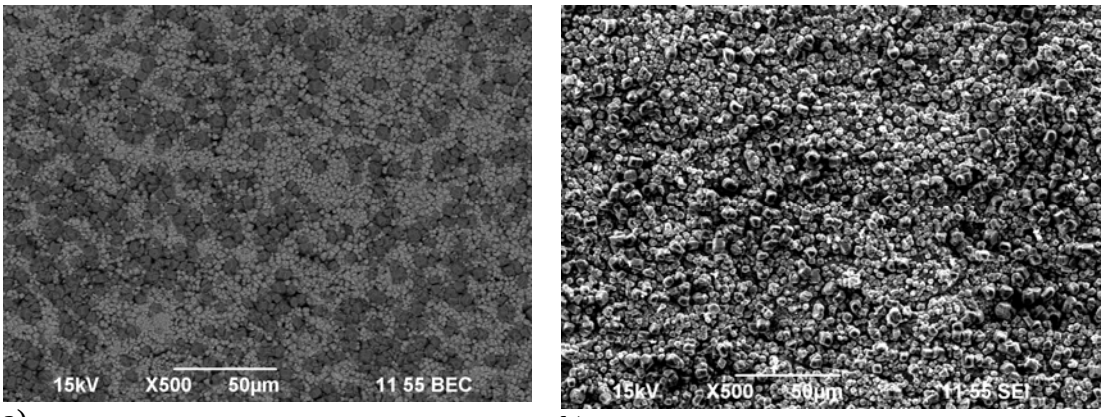


a) b)

Figure 2-14 a) BSE and b) SE micrographs at 500 times magnification of scaled coupon from autoclave test at 150$^{o}$C.

The 3D projection image suggests that magnetite, ferrous hydroxide and iron carbonate co-exist as the corrosion product scales with the magnetite scale which forms at the early stage on the carbon steel surface, formed by the redox reactions, and iron carbonate which forms later in the process after it reached its solubility limit and precipitates over the scale surface.

#### 2.3.1.2. Autoclave test at 150$^{o}$C under $N_2$

The autoclave test was repeated in the absence of carbon dioxide (under nitrogen atmosphere) with the initial pH of the solution adjusted to 4.6 with a small amount of 0.1 M HCl, to give a similar pH (pH 5.5) to when low partial pressure of carbon dioxide was injected. The scale was analysed under SEM and was observed to be composed of single species crystals (Figure 2-15) which were identified as magnetite using the Raman technique as shown in Figure 2-16. The crystals were not noticeable under low magnification in SEM (Figure 2-15a), but the appearance of the unique octahedral shape magnetite crystals of about 1µm size or less on the carbon steel surface became clearer as the magnification was increased to 10,000 times as shown in Figure 2-15b. The scale was more porous and patchy than the scale formed in the presence of carbon dioxide.

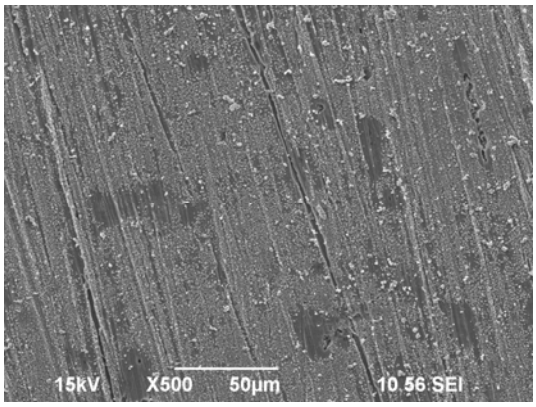


a) 500x magnification

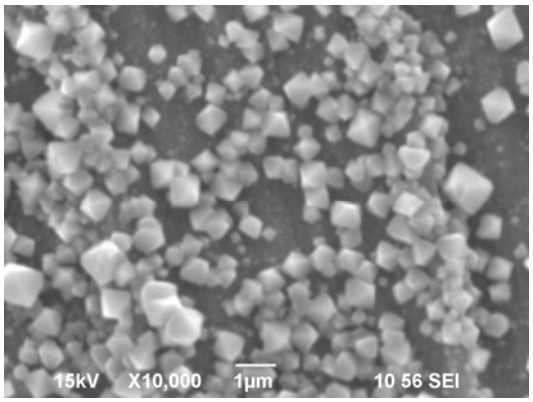


b) 10,000x magnification

Figure 2-15 SEM micrographs of scaled coupon from autoclave test at 150°C without $CO_2$ taken at different magnifications.

Analysis of the Raman results confirmed that the products on the X-65 carbon steel consist of magnetite with its characteristic stretch at 675 $cm^{-1}$ and two weak stretches at 298 and 550 $cm^{-1}$ (Legodi & de Waal, 2007). The micrograph image from a 100 times objective lens in Figure 2-16a shows the relatively stable crystals, less than a micrometer, on the coupon surface which were not readily oxidized to hematite upon exposure to air. Magnetite scale was formed even though the solution is acidic because HCl is not a strong buffer and the pH of the solution, especially at the coupon surface layer, changes significantly as corrosion takes place with the consumption of $H^+$ during the corrosion reaction.

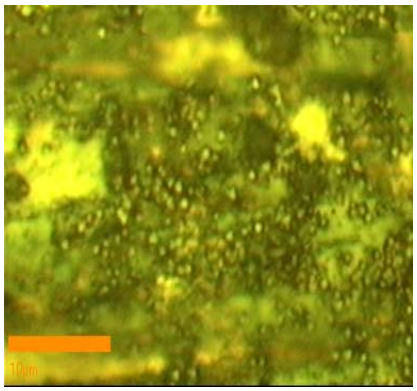

a)

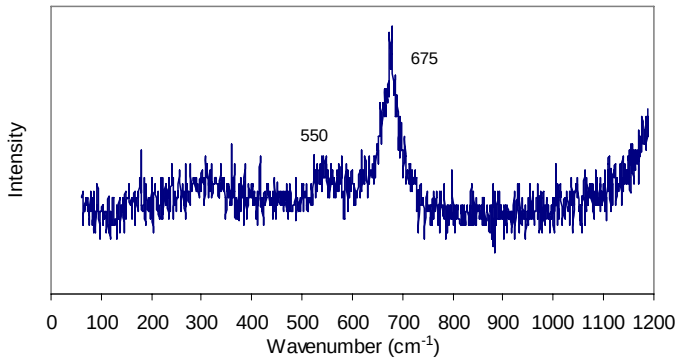


b)

Figure 2-16 a) Raman optical microscope image (with 10 µm scale bar) and b) Raman spectra of the crystals formed in autoclave at 150°C under nitrogen.

### 2.3.1.3. Autoclave test at 80°C under low P $CO_2$

The autoclave test at 80°C in the presence of low partial pressure carbon dioxide for 48 hours did not produce much corrosion product scale on the carbon steel coupon surface. The corrosion products were not readily detected on SEM as shown in Figure 2-17.

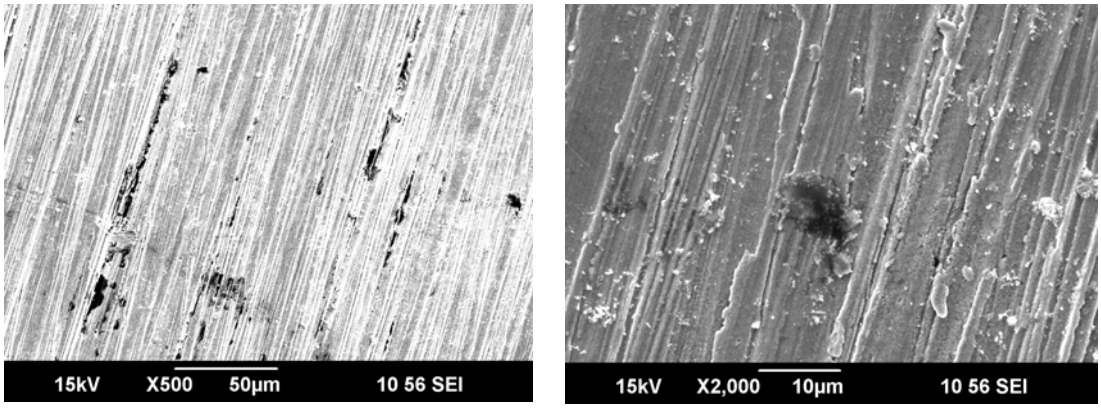


a) 500x magnification b) 2000x magnification

Figure 2-17 SEM micrographs of scaled coupon from autoclave test at 80°C with $CO_2$ taken at a) 500 and b) 2000 times magnifications.

Small patches of agglomerated crystals were detected under careful investigation of the coupon sample under the light microscope at 100x magnifications as shown in Figure 2-18a. The crystals were confirmed by Raman analysis as magnetite. Overall, the surface appears fairly clear with little evidence of corrosion on the surface.

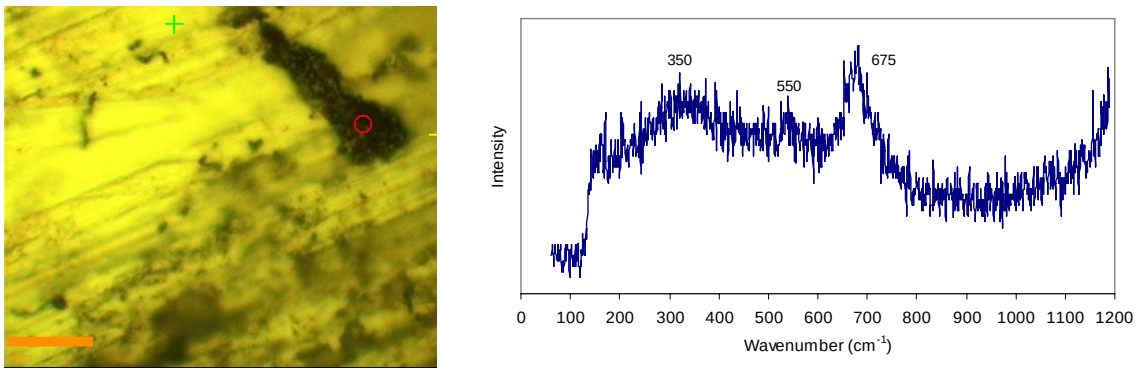


a) b)

Figure 2-18 a) Optical image (on 10 µm scale bar) and b) Raman spectra of the crystals formed in autoclave at 80°C under low partial pressure $CO_2$.

### 2.3.2. In-situ electrochemical autoclave test

#### 2.3.2.1. Electrochemical autoclave test at 80°C under low $P_{CO_2}$

The ex-situ autoclave test results clearly showed the presence of corrosion product scales on the carbon steel surface but the mechanism of the formation could not be deduced. Therefore, the jet impingement cell (JIC), which has the capability of applying electrochemical measurements on the electrode, was used as an autoclave to study the electrochemistry of the scale formation in-situ. Since the scale formation had to be closely correlated to the oil and gas field operating conditions, the in-situ electrochemical study of the scale formation was conducted at 80°C in a standard brine solution deaerated under low partial pressure of $CO_2$ gas, with the measured pH of 5.5. The open circuit potential of the X-65 carbon steel electrode and its polarisation resistance from the LPR method, recorded over a period of 40 hours are shown in Figure 2-19.

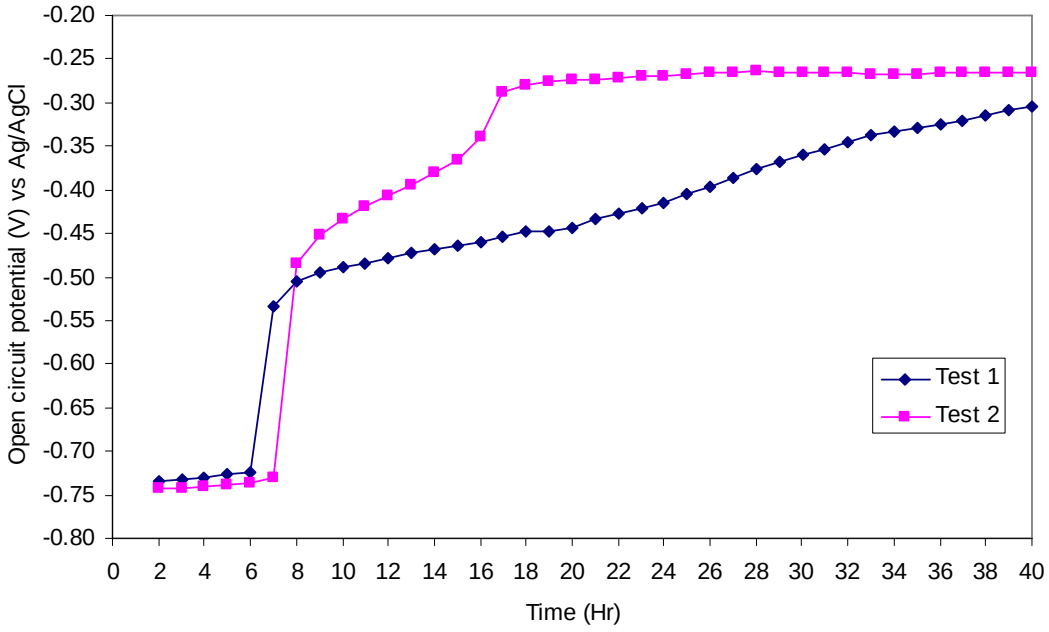


Figure 2-19 Open circuit potential (OCP) of carbon steel corroding in low partial pressure of $CO_2$ at 80°C and at pH 5.5.

The open circuit potential of the electrode remained consistent at about -0.73 V vs Ag/AgCl throughout the first 7 hours. At the 7$^{th}$ hour, a sudden potential increase to around -0.53 V was recorded. The potential increased gradually after the leap point to around -0.3 V. The anodic shift in potential (towards positive potential) was

ascribable to preferential suppression of the anodic half-reaction owing to the formation and build-up of the corrosion product which retarded the diffusion of the reductive species to the steel surface (Cornell & Schwertmann, 1996; De Marco et al., 2005). The consistency of the sudden potential shift in both sets of results verified that it was not a spike due to instrumentation error but an indication of a surface change from a newly formed corrosion product scale that has a different redox potential to that of the carbon steel. The changes observed in the open circuit potential alone are not sufficient to allow definitive conclusions to be made, so a combination of other supporting electrochemical measurements was employed. LPR and EIS techniques were used to further elucidate the corrosion mechanism. The polarisation resistance, Rp, of the carbon steel from the LPR measurements are presented in Figure 2-20.

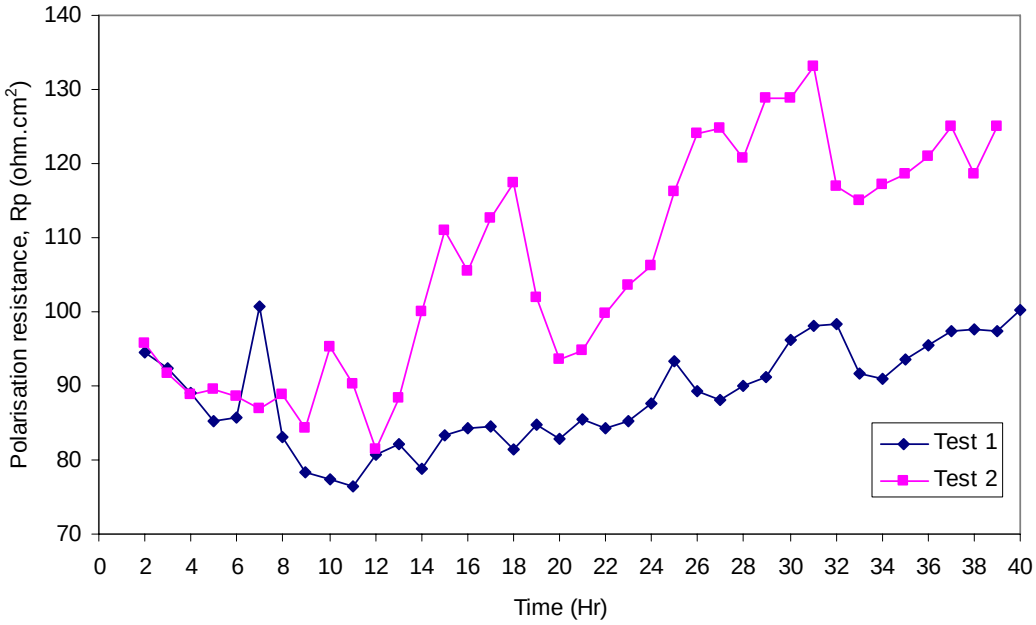


Figure 2-20 LPR results of carbon steel in standard brine solution under low partial pressure of carbon dioxide at 80$^{o}$C, pH 5.5.

The polarisation resistance of the duplicate tests does not show a sharp increase on the Rp at the 7$^{th}$ hour as seen on the OCP results but a continuous fluctuation of Rp values. A sharp chance in measured polarisation resistance values was not observed as the LPR technique, in general measures the overall resistance of a system. Individual resistivity components from the solution, electrode, pores and the scale layer, if they are present, cannot be resolved using the LPR technique. As such, it

was important to clarify the occurrence of any discrepancy in the measured resistance by comparing the polarisation resistance with the impedances measured from the EIS technique. The progressive impedance spectra of the corroded carbon steel from test 1, in the form of Nyquist and Bode representations, are presented in Figure 2-21, Figure 2-22 and Figure 2-23. Each impedance spectrum as displayed on the Nyquist plots consists of two capacitive loops. The emergence of the double capacitive loops often correlates to the formation of a surface layer on the corroding surface.

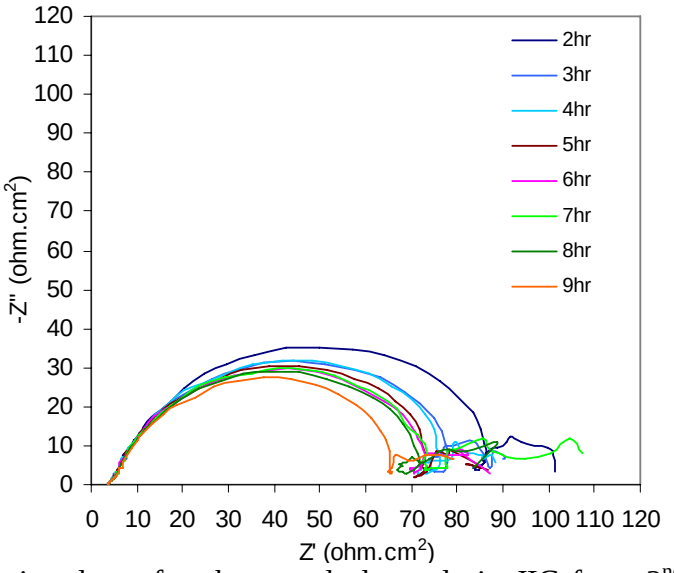


Figure 2-21 Nyquist plots of carbon steel electrode in JIC from 2nd to 9th hour of test 1.

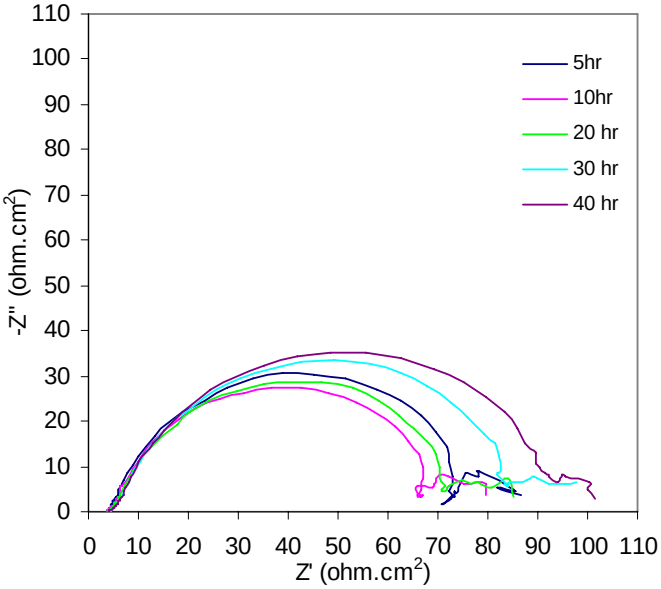

Figure 2-22 The progressive Nyquist plots of carbon steel electrode over 40 hours of test 1.

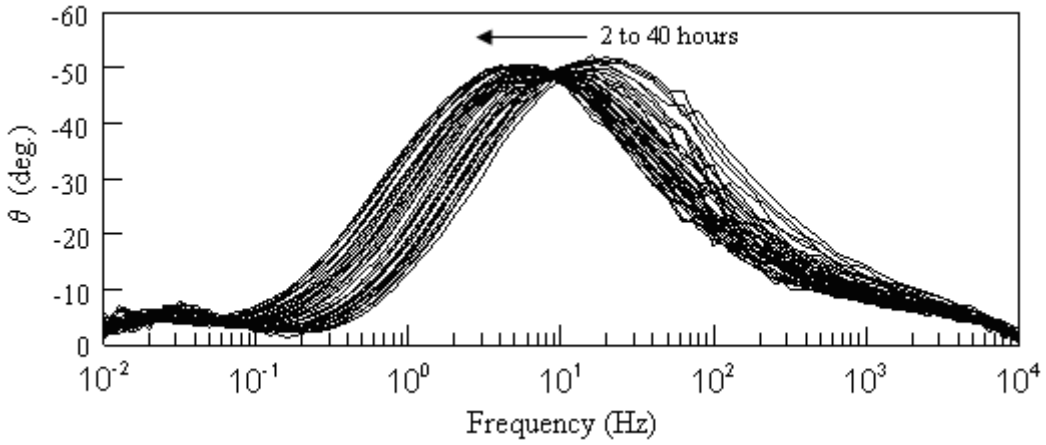


Figure 2-23 The progressive Bode phase plots of carbon steel corrosion over 40 hours from test 1 with 39 plots overlaid.

The larger semicircle (capacitive loop) on the Nyquist plot represents the corrosion resistance of the carbon steel. As such, the corrosion rate of the carbon steel as exhibited in Figure 2-21 was increasing slowly in the first 8 hours. Whereas, the second time constant which is ascribable to the formation of a surface layer was ill defined. At the 7th hour, the measurement collected at low frequency was extraordinarily noisy. This abrupt change coincided with the instantaneous spike in the OCP as well as the LPR results. The spike on the LPR result actually confirmed that the expansion of the second time constant was not an artefact of the instrument noise but likely a response of a phase transformation. After the abrupt changes, the charge transfer resistance of the electrode dropped significantly which suggested that the developing phase appeared to result in accelerated corrosion. It is hypothesized that the reaction occurring was likely to be the transformation of an amorphous phase to a porous crystalline phase. Since the disappearance of the hydroxide phase and appearance of the magnetite phase was detected in Kumai and Devine's in-situ surface enhanced Raman corrosion monitoring test of carbon steel in water at elevated temperature (Kumai & Devine, 2005), it is likely that this transformation reaction in the present work also involves the hydroxide phase converting to magnetite. With the presence of carbonate species in carbon dioxide environments, the reacting species in this experiment may be different from their work. However, the transformation was unlikely to be the iron carbonate formation as both iron and

carbonate concentrations were below the solubility limit for the precipitation reaction to proceed at an early stage of corrosion.

Subsequent to the extended period of iron dissolution and the continual build-up of a secondary layer, a state of partial passivation was achieved when the active carbon steel was fully covered with the corrosion product scale which suppressed the anodic process. As such, the polarisation resistance of the carbon steel began to increase gradually after 20 hours as shown in Figure 2-22. On the other hand, the second capacitive loop became more defined and the resistivity of the second time constant remained relatively constant throughout.

The small capacitive loop is normally observed in the high frequency region in the studies of coated metals and is fitted in an equivalent circuit model as shown in Figure 2-24. The pore resistivity, Rpo is represented by the small capacitive loop at the high frequency region followed by the resistivity of the charge transfer of the metal, Rct (a larger capacitive loop) at the low frequency region. However, the sequence of the two capacitive loops on the Nyquist plots measured in this test was reversed. The reversal of these features has never been clearly justified using an equivalent circuit model but this type of impedance behaviour has been seen in several studies on metal dissolution and prepassivation. Turgoose and Cottis (Turgoose & Cottis, 1993) claimed that the appearance of this secondary capacitive loop at low frequency region was due to an event of a reversible anodic process of iron dissolution and formation of a surface film that restricted diffusion of ions through the surface film. However, detailed justifications were made using a rigorous reaction model simulation based on metal-passivation kinetics instead of the equivalent circuit model. An extensive EIS study on iron dissolution at pH ranging from 0 to 5 was carried out by Keddam et al. (Keddam, Mottos, & Takenouti, 1981a, 1981b) and the results interpreted based on simulated reaction models. Iron dissolution and prepassivation with the emergence of double capacitive loops were observed at pH higher than 4. The appearance of a second high-frequency capacitive loop was claimed to be associated with the passivation process.

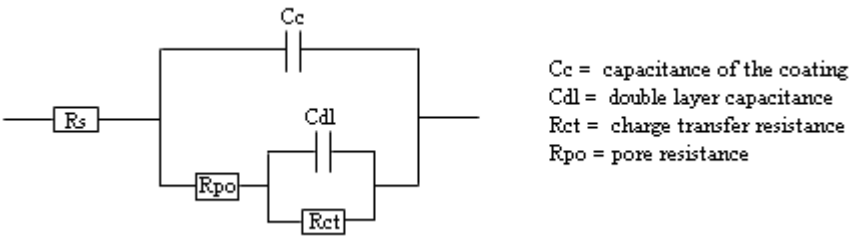


Figure 2-24 Equivalent circuit of a coated metal (Macdonald, 1987).

In order to justify the event of passivation as indicated by the EIS results, an advanced surface morphology analysis was adopted to examine the surface film since the previous SEM results did not reveal any corrosion product on the steel surface. Therefore, a FESEM was used because it can resolve nano scale particles if they are present by lowering the accelerating voltage of the electron gun. A comparison of the surface morphology captured at two different accelerating voltages (20 kV and 3 kV) is presented in Figure 2-25.

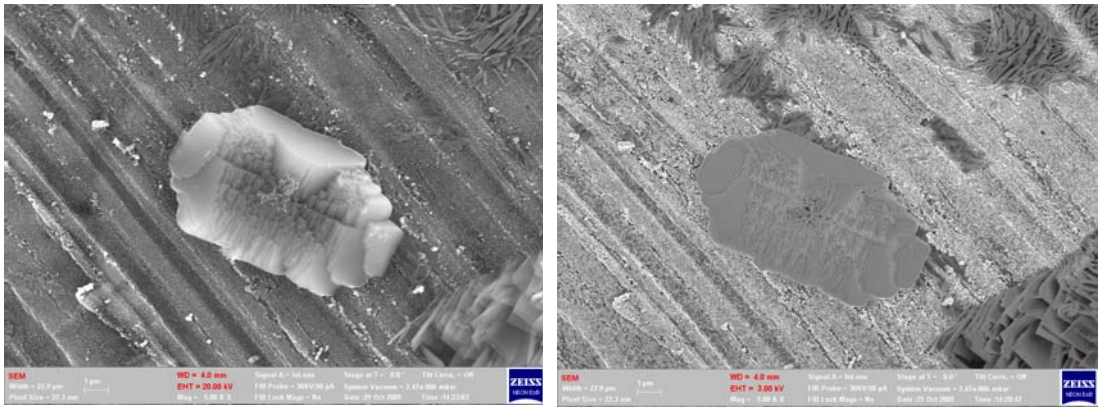

a) Image acquired at 20 kV b) Image acquired at 3 kV

Figure 2-25 Comparison of FESEM image at 5000x magnification acquired at a) 20 kV; b) 3 kV.

At 5000x magnification and high accelerating voltage on the FESEM (Figure 2-25a), some corrosion products were projected, but not clear. The carbon steel surface seems to look dull and clear from any corrosion product except for few crystals dispersed over the surface. However, when the accelerating voltage was dropped to 3 kV (Figure 2-25b), it revealed all the bright ultrafine nano crystals, covering the carbon steel surface. These ultrafine nano crystals were not present on the as-prepared polished carbon steel coupon with smooth surface before corrosion. Besides, the fuzzy needle-like structure as seen at higher accelerating voltage was

actually plate-like or better described as lath-like fibrous structure that grows laterally. This microcrystalline fibrous habit signified the feature of the mineral group of rosasite with the general formula of $A_2(OH)_2CO_3$ similar to the chukanovite ($Fe_2(OH)_2CO_3$) structure (Pekov et al., 2007; Ray, 2006). On the other hand, Figure 2-25b clearly shows a contrast in brightness with the variation of structures that suggests there were three different phases on the steel surface.

A widespread of the fibrous structures was clearly displayed on the same test specimen but at a randomly selected spot shown in Figure 2-26. This structure was definitely different from the iron carbonate crystals and was likely chukanovite as this product was reported by De Marco et al. (De Marco et al., 2005) in their in-situ GIXRD synchrotron experiments on $CO_2$ carbon steel corrosion. Further EDS and GIXRD analysis was undertaken in order to confirm the identity of this product.

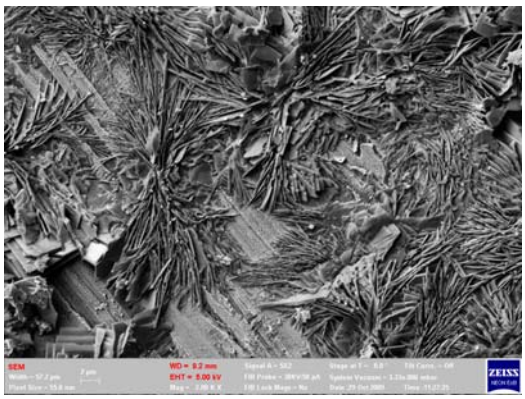

a) 2000x magnification

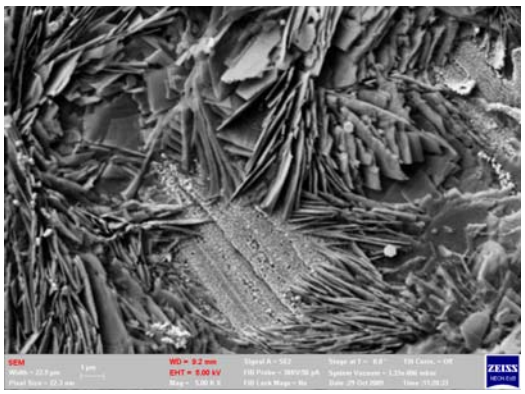

b) 5000x magnification

Figure 2-26 FESEM image from secondary electron detector 5 kV under a) 2000x magnification; b) 5000x magnification.

The carbon steel surface seems to be covered by polycrystalline material. Therefore, a higher magnification of the scale morphology was obtained to confirm if the bright surface was a scale layer and not the bare steel surface. In fact, a 20,000 times magnification surface image as depicted in Figure 2-27 clearly shows that the steel surface was covered by nano size crystals.

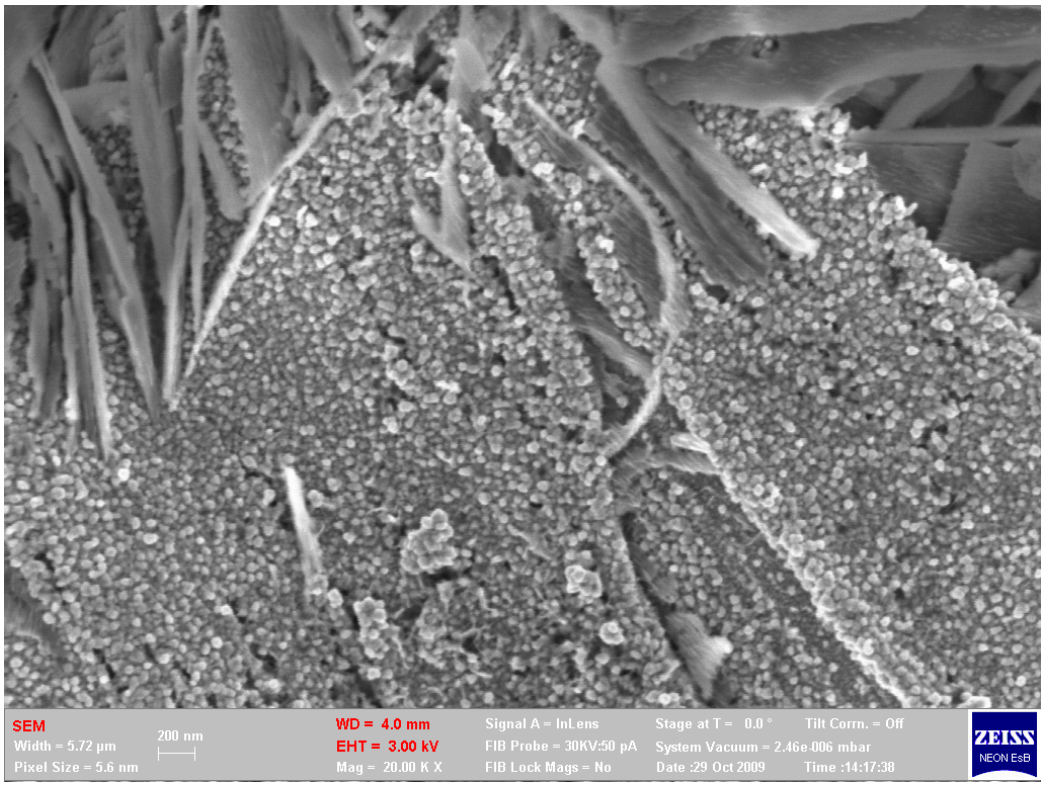


Figure 2-27 FESEM image from InLens detector 3 kV under 20,000x magnification.

Different crystal structures were clearly projected under the FESEM at low accelerating voltage. However, the elemental analysis from the EDS detector could not be performed at low accelerating voltage but at 20 kV as most elements lie within this energy range. The surface scale morphology in Figure 2-28 from the back scattered electron detector was slightly fuzzy. The actual lath-like fibrous structure was unclear under the normal SEM operating condition. A fuzzy image of a needle-like structure is visible in many published papers on iron carbonate scale (Han, Yang, Brown, & Nesic, 2008; Yang, Brown, & Nesic, 2008) but this peculiar structure under the iron carbonate scale has not been identified and was not subject of the investigation. Since the actual scale morphology was identified earlier on, an EDS analysis was targeted at the different structures to investigate if the elemental compositions were different. The composition of the different structure is presented in Table 2-2. The results clearly show a variation in the atomic percentages of carbon, oxygen and iron which suggests that the scale comprises different iron compounds, which could be $Fe_2(OH)_2CO_3$, $Fe_3O_4$ and $FeCO_3$. Based on the ratio of Fe:O:C in the results, the lath-like structure was probably chukanovite. However, EDS could not distinguish the compound accurately since the detection window

excluded the detection of hydrogen. Moreover, chukanovite is a new mineral in corrosion science and mineralogy; it was indeed difficult to obtain a pure sample as a standard for calibration.

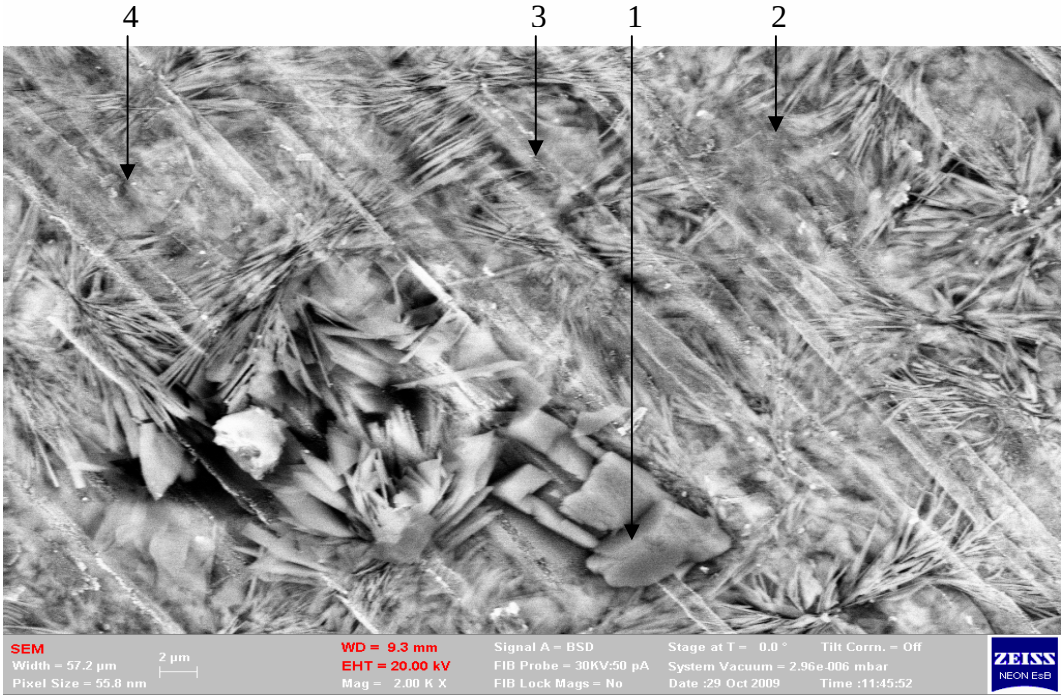


Figure 2-28 FESEM image from backscatter detector at 20 kV and 2,000x magnification.

Table 2-2 Elemental analysis of the crystals.

| Spectrum | Fe | C | O | S | Mn | Ni | Cu | Total | Possible compounds |
|---|---|---|---|---|---|---|---|---|---|
| 1 | 14.5 | 20.9 | 64.4 | 0.0 | 0.3 | 0.0 | 0.0 | 100 | $FeCO_3$ |
| 2 | 38.3 | 8.8 | 49.8 | 0.0 | 0.4 | 0.8 | 2.0 | 100 | $Fe_3O_4$ |
| 3 | 20.7 | 13.9 | 61.8 | 0.5 | 0.0 | 0.7 | 2.4 | 100 | $Fe_2(OH)_2CO_3$, $Fe_3O_4$ |
| 4 | 23.9 | 13.7 | 59.4 | 0.5 | 0.0 | 0.7 | 1.7 | 100 | $Fe_2(OH)_2CO_3$, $Fe_3O_4$ |

Owing to the uncertainty in the EDS results, SR-GIXRD was adopted to justify the presence of chukanovite in the lath-like fibrous structure. The diffraction pattern of the scale surface as shown in Figure 2-29 was taken at two different incidence angles of $0.5^o$ and $3.85^o$. At the incidence angle of $3.85^o$, a higher depth of penetration of the sample was achieved, which showed high intensity of the steel substrate as strong

α-Fe peaks at the 2-theta angles of 28.5, 40.8, 50.6, 59.1, 67.0 and 74.3. The diffraction data of 2-theta angle below 25 (7.67, 9.34, 11.17, 12.21, 15.34, 15.42, 18.97, 19.06, 19.24, 19.75, 20.21, 21.77 21.85, 22.47, 22.86, 23.22, 24.34 and 24.60) were all matched up with the chukanovite peaks. In fact, the lath-like fibrous structure was indeed chukanovite. On the other hand, iron carbonate was evident at incidence angle of $0.5^{o}$ with peaks at 18.55, 20.29, 22.33, 24.28, 26.59, 27.51, 27.62, 31.36, 31.85, 33.38, 33.68, and 35.52. These peaks appeared at the incidence angle of $0.5^{o}$ but not at $3.85^{o}$ which suggest that the disappearance of this peak at higher incidence angle was in accord with the previous hypothesis that the iron carbonate was formed later in the corrosion process via the precipitation reaction, upon exceeding its solubility limit. Perhaps chukanovite is one of the underlying porous and brittle corrosion product scales that would eventually be covered up by the deposition of iron carbonate which was detected at incidence angle of $0.5^{o}$. Of all the peaks observed, it was very difficult to identify the presence of magnetite peaks. There was a tiny broad peak at $22.8^{o}$ which could be magnetite but the signal to noise ratio from this tiny peak was too low to confirm the presence of magnetite using SR-GIXRD. Besides, amorphous or poorly crystalline structures cannot be accurately detected by XRD.

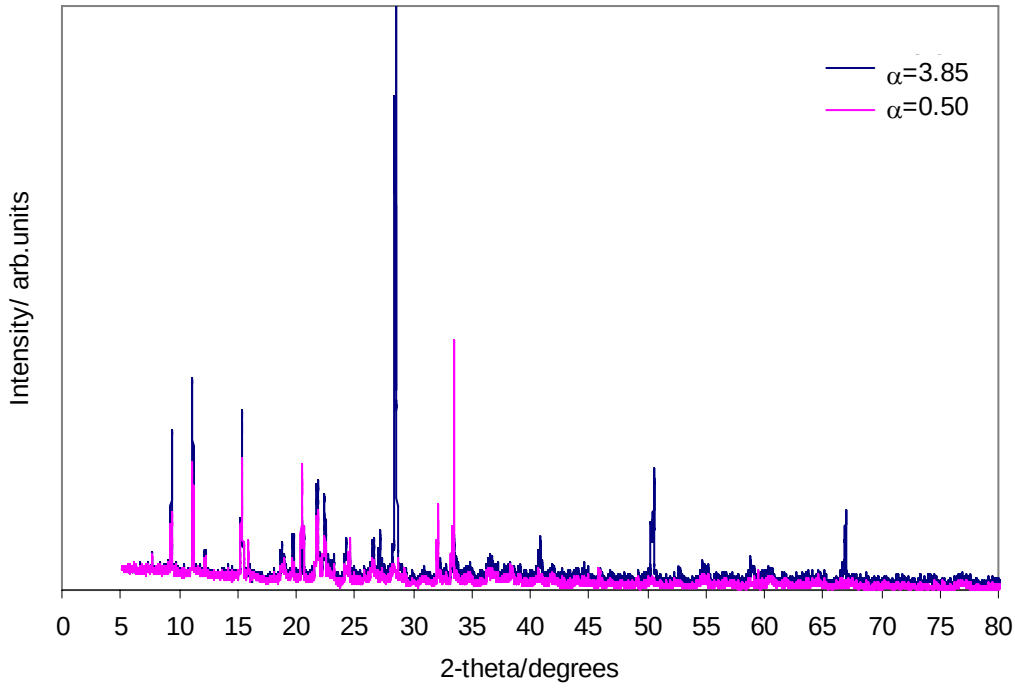

Figure 2-29 SR-GIXRD diffraction patterns at λ = 1 Å of a corroded mild steel electrode exposed in 30 g/L NaCl buffered with 0.1 g/L $NaHCO_3$, at 80°C and pH 5.5 saturated with mixed high-purity nitrogen and carbon dioxide.

Since the presence of chuknovite was identified from the GIXRD and confirmed from the FESEM with the lath-like fibrous structure, it would be useful to determine the Raman spectrum of this product as the Raman spectrum associated with this product has not been reported explicitly elsewhere. Though chukanovite falls under the mineral group of rosasite, the deformation modes and the vibration modes of the molecular stretches can be slightly different. Therefore, the Raman spectrum of the chukanovite formed on the scale was acquired and analysed. The Raman spectrum of chukanovite, as shown in Figure 2-30, has more bands than iron carbonate and the spectrum is closely correlated to the rosasite minerals. The band observed at 1068 $cm^{-1}$ is the significant $\nu_1$-$CO_3^{2-}$ symmetric stretching mode which is slightly shifted from the $\nu_1$-$CO_3^{2-}$ of iron carbonate at 1086 $cm^{-1}$ (Chan et al., 2009). In addition, a component band observed at 717 $cm^{-1}$ is the assigned $\nu_4$ mode of $CO_3^{2-}$ and the 1500 $cm^{-1}$ band is the $\nu_3$-$CO_3^{2-}$ antisymmetric stretching which seems to be affected by the hydration of the compound. Since there is hydroxide associated with this compound, the band at 512 $cm^{-1}$ could possibly be the hydroxyl deformation modes. The bands at 376, 582 and 677 $cm^{-1}$ are attributed to Fe-O stretching vibrations. There are two lower bands at 211 and 256 $cm^{-1}$ which can be assigned to the lattice mode (Erdös & Altorfer, 1976; Ray, 2006).

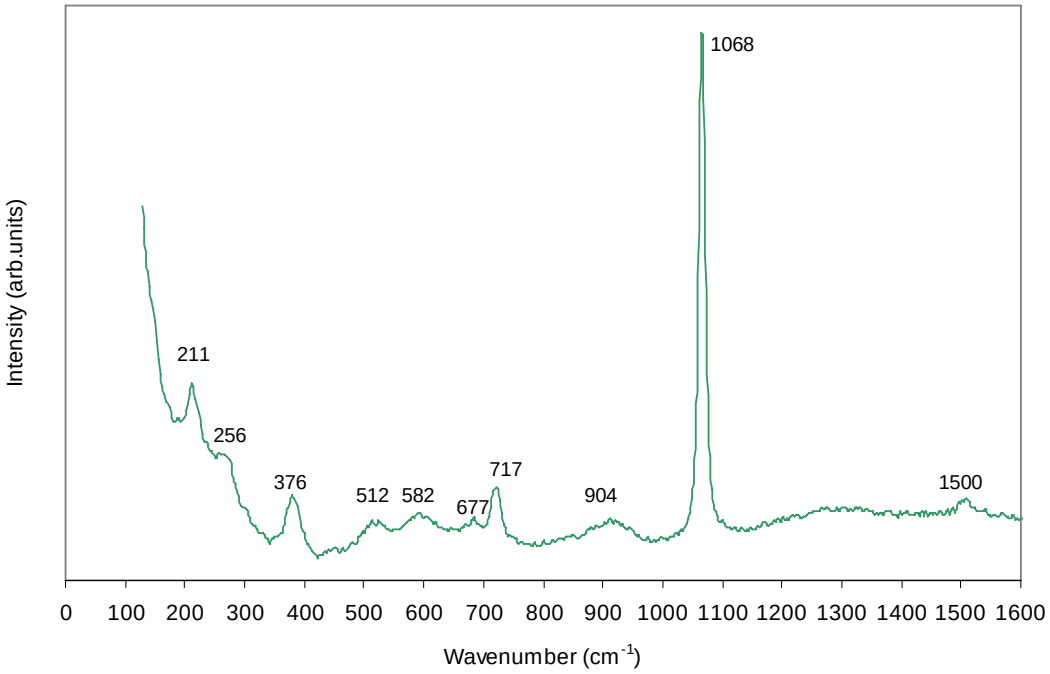


Figure 2-30 Raman spectrum of corrosion a corroded mild steel electrode exposed in 30 g/L NaCl buffered with 0.1 g/L $NaHCO_3$, at 80°C and pH 5.5 saturated with mixed high-purity nitrogen and carbon dioxide.

### 2.3.2.2. Electrochemical autoclave test at 80°C under $N_2$

Previous electrochemical measurements and surface analytical results of the low $CO_2$ partial pressure test at 80°C showed the formation of different phases of corrosion product scale. In order to test the hypothesis that the phase transformation during a sudden potential increase was the formation of magnetite, a set of tests was conducted in the absence of a carbonate source but at the same pH range. A brine solution, containing 30 g/L NaCl, with the pH adjusted to pH 6 with the addition of HCl, was deaerated with nitrogen gas. The open circuit potentials of the carbon steel are shown in Figure 2-31. Clearly, a consistency in potential increase was observed in the sets of tests with and without carbon dioxide which confirmed that the response was indicating a phase formation. Since there was no carbonate in this test, the possibility of the phase containing carbonate was eliminated. Hence, the response was likely the phase development of either iron hydroxide or magnetite.

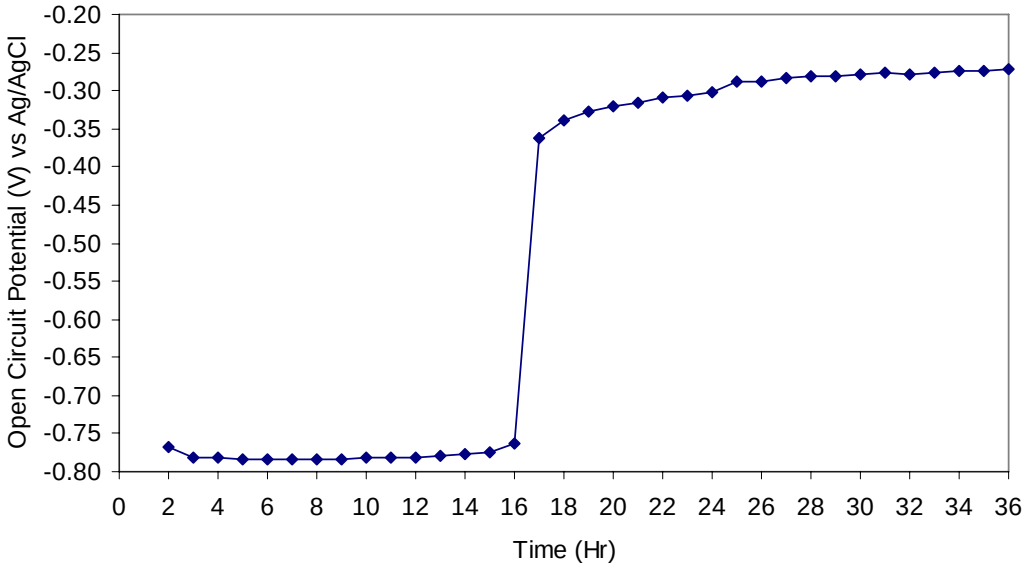


Figure 2-31 Open circuit potential of carbon steel in 30 g/L NaCl solution at pH 6, in the JIC at 80°C.

Additionally, the LPR results presented in Figure 2-32 also show a spike in the polarisation resistance. The sudden increase in LPR results is similar to the previous test results in the presence of $CO_2$. Moreover, this spike was again observed in the EIS results with an unstable impedance response towards the low frequency region at the 16$^{th}$ hour as shown in Figure 2-33.

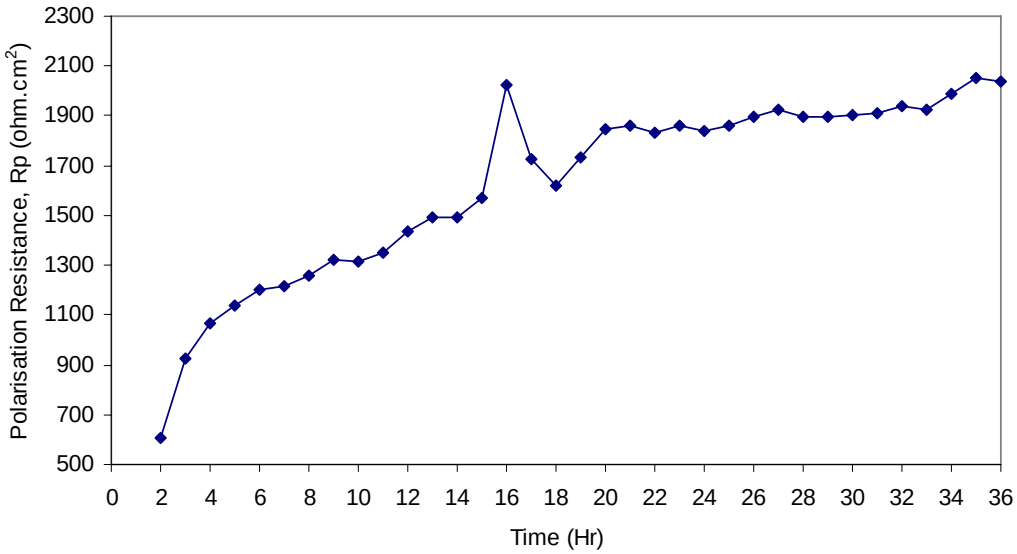


Figure 2-32 LPR measurements of the polarisation resistance of carbon steel in 30 g/L NaCl solution deaerated with nitrogen at pH 6, in the JIC at 80°C.

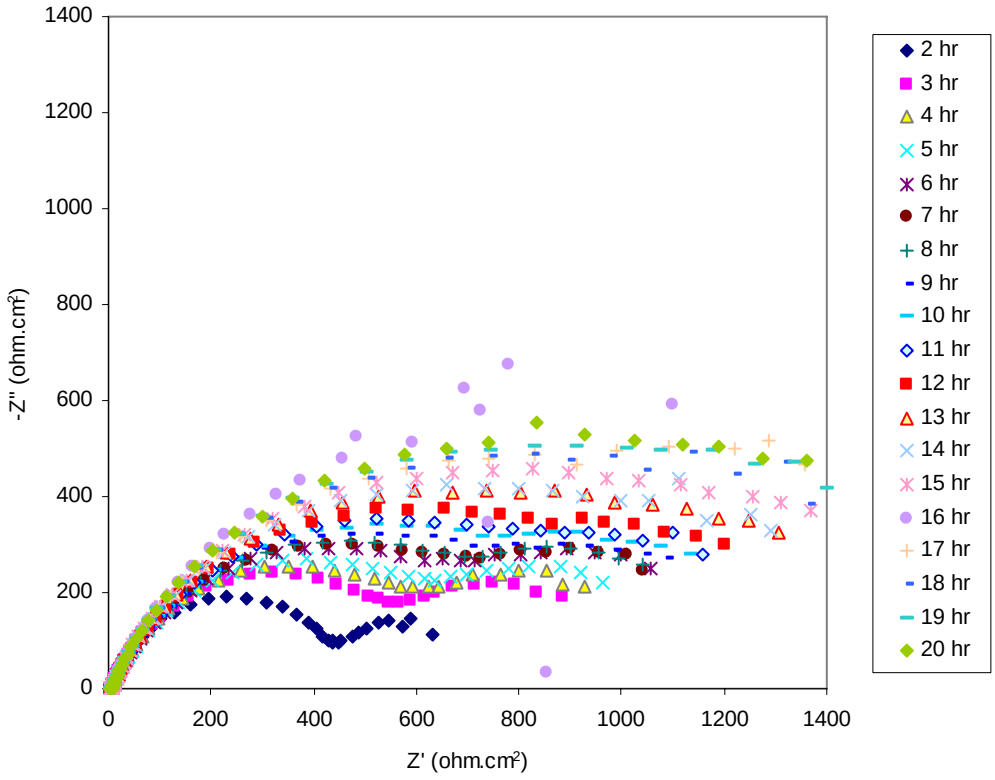


Figure 2-33 Nyquist plot of carbon steel in 30 g/L NaCl solution deaerated with nitrogen at pH 6, in the JIC at 80°C.

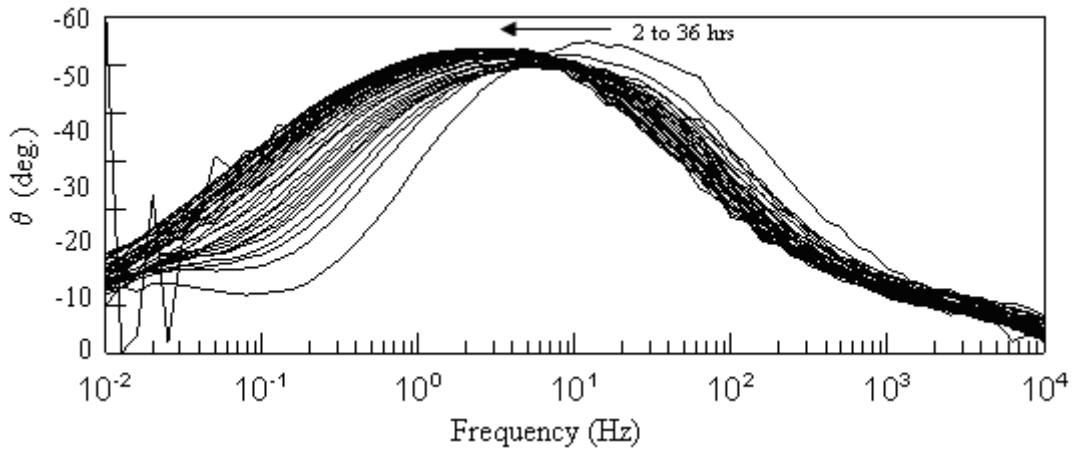


Figure 2-34 Progressive Bode phase plots of carbon steel corrosion over 36 hours in 30 g/L NaCl solution deaerated with nitrogen at pH 6 and 80$^{o}$C with 35 plots overlaid.

The Nyquist plots of the tests with and without the presence of carbonate species all showed capacitive loops. However, in the absence of carbonate species the charge transfer resistance increased progressively and the Nyquist plots were smoother. Besides, the growth of the first and second time constant was almost at an equal rate. Subsequently, the second time constant seems to merge with the first time constant to form a single time constant before the impedance response became erratic at the 16$^{th}$ hour. On the Bode phase plot, the first time constant appeared at around 10 Hz but slowly shifted to around 1 Hz. The second time constant was observed at around 0.01 Hz. Over time, the Bode phase plots shifted towards lower frequency and the second time constant was not seen - it could be outside the frequency range that was measured. The depressed semicircles on the Nyquist plot are consistent with a porous phase on the surface. It was hypothesized that the porous phase underwent a transformation at the 16$^{th}$ hour that caused an unstable state on the electrode surface.

Analysis of the impedance spectra using the Scribner Zview version 2.7 software showed that the impedance data did not fit the traditional coating model. In fact, it fitted well in the semiconductor model with the following equivalent circuit of two capacitances in series as shown in Figure 2-35.

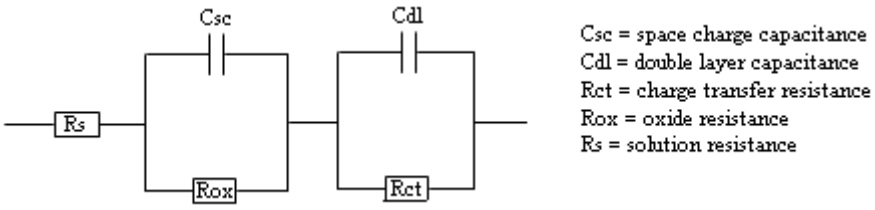


Figure 2-35 Equivalent circuit of a semiconductor model (Macdonald, 1987).

Since the data fits well with the semiconductor model, it suggests that the scale formed is semiconductive. The difference in magnitude and trend of the two capacitive loops of the Nyquist plots under low partial pressure carbon dioxide and nitrogen corrosion suggest that dissimilar corrosion products were formed when carbon dioxide was introduced into the system despite the fact that both are under mildly acidic conditions. The corrosion product may be the semiconductive magnetite scale. According to the semiconductor model, the first semicircle on the Nyquist plot in the high frequency region is associated with the space charge layer capacitance and the second semicircle in the lower frequency region is associated with the double layer capacitance (Bott, 1988; Macdonald, 1987).

Since the double layer capacitance is of 2 to 3 orders of magnitude larger than the space charge capacitance, the double layer capacitance should appear at the low frequency region. The fitted results of the Nyquist plots in Figure 2-36 shows a relatively constant charge transfer resistance throughout the test at around $427\pm28$ ohm.cm$^2$. Whereas the resistivity of the scale layer continued to increase as the corrosion product continued to build-up on the scale surface. However, the charge transfer resistance calculated from the analysis software can only be treated as an estimate because the complete impedance spectra at the very low frequency region could not be measured reliably with good confidence in the data acquired.

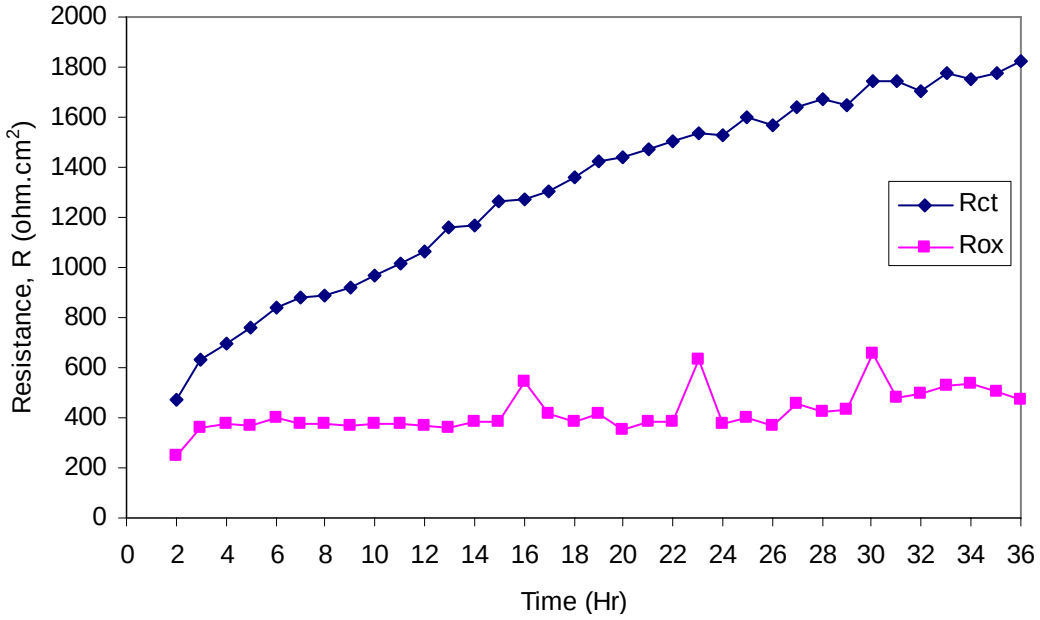


Figure 2-36 Fitted results of the impedance spectra from the semiconductor model using the Scribner Zview version 2.7 software.

The electrochemical impedance results seem very promising in illustrating the scale development but it is still important to justify the presence of the scale under the microscope to support the hypothesis. Previous microscopy images of the ex-situ analysis of coupons corroded in the autoclave at 80$^{o}$C failed to detect any corrosion product scale on the surface. Nevertheless, if the corrosion product was present on the nano scale, the SEM would not have resolved it. Therefore the FESEM was used to verify the prediction from the EIS results to detect the presence of the corrosion products. At low magnification and high electron voltage (500 times magnification and 20kV), the surface of the steel shown in Figure 2-37 looked as if there was no corrosion on the carbon steel besides the polishing marks as previously seen on the SEM.

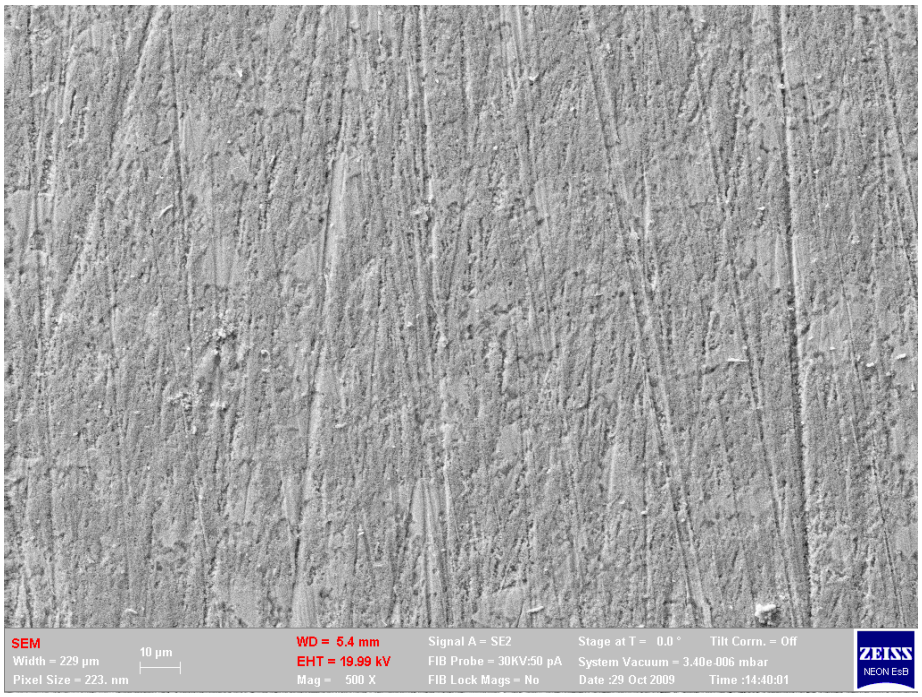


Figure 2-37 Morphology of the carbon steel surface at 500x magnification and 20 kV after 36 hours in 30 g/L NaCl solution deaerated with nitrogen at pH 6, in the JIC at 80$^{o}$C.

If the surface was truly devoid of any corrosion product scale, that would imply that the interpretation of the EIS results was wrong. However, a definitive conclusion cannot be made from low magnification topography. Therefore, the magnification was brought up to 5000x magnification on the FESEM and at low accelerating voltage. Suddenly, the unseen nano particles projected up clearly as shown in Figure 2-38 and Figure 2-39. The entire surface of the carbon steel was covered with nanoparticles which consist of a mixture of well defined crystals and extremely fine polycrystalline material. Even pores that were present in the polycrystalline material were hard to determine. The cubic structure of the larger crystals resemble the structure of magnetite as reported by Cornell and Schwertmann (Cornell & Schwertmann, 1996). However, the fine polycrystalline material was unclear. Therefore, the surface was magnified to the highest limit at 50,000 times. The ultrafine polycrystalline material was found to be charging under the FESEM as seen in Figure 2-40, as the carbon steel was not sputter coated with a conductive coating. This suggests that the ultrafine polycrystalline material was non-conductive but the nano crystals were either conductive or semiconductive.

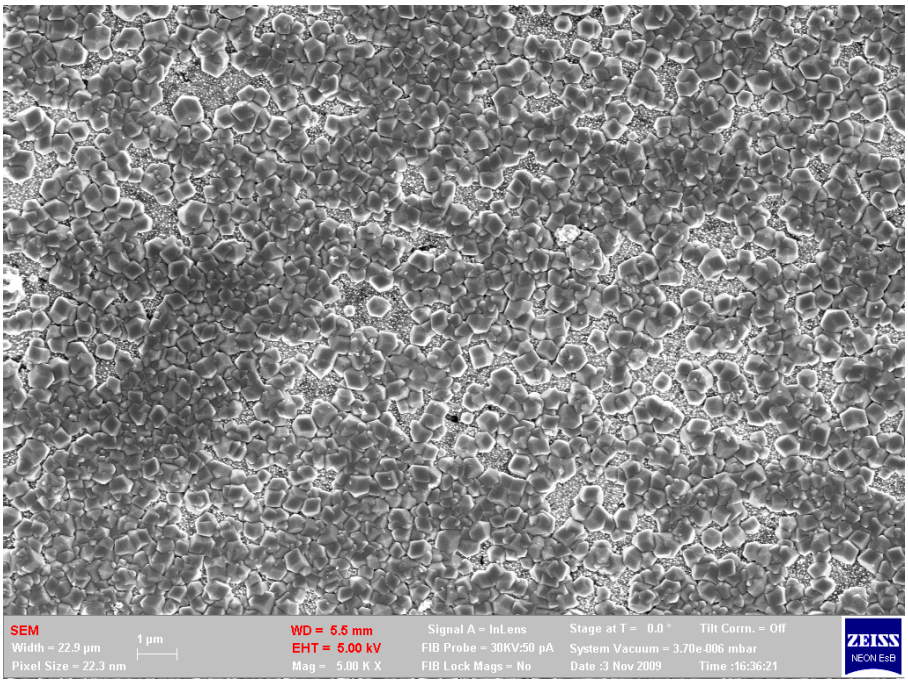


Figure 2-38 Morphology of the carbon steel surface at 5000x magnification and 5 kV after 36 hours in 30 g/L NaCl solution deaerated with nitrogen at pH 6, in the JIC at 80°C.

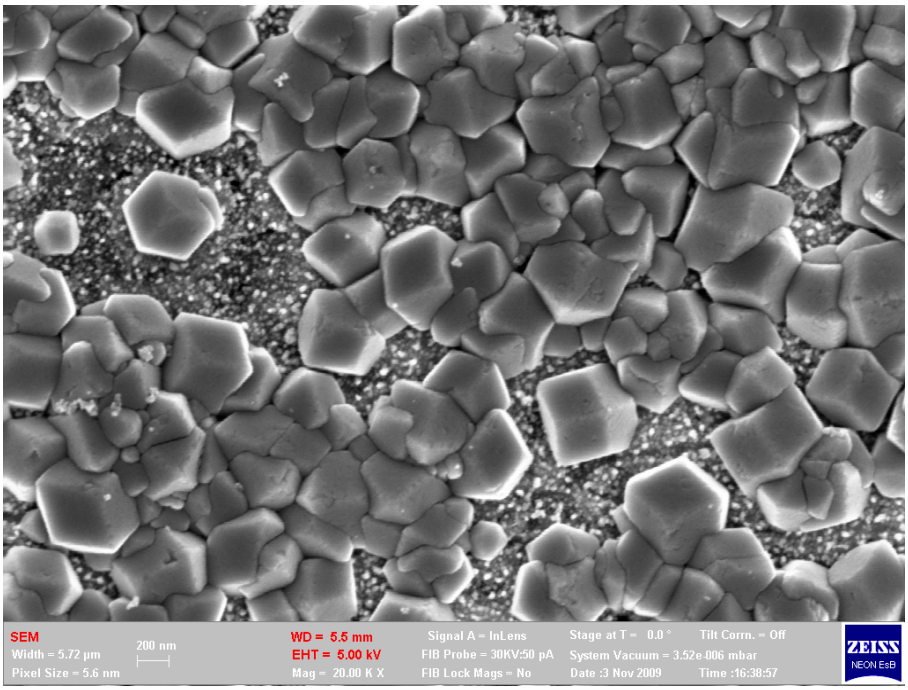


Figure 2-39 Morphology of the carbon steel surface at 20,000x magnification and 5 kV after 36 hours in 30 g/L NaCl solution deaerated with nitrogen at pH 6, in the JIC at 80°C.

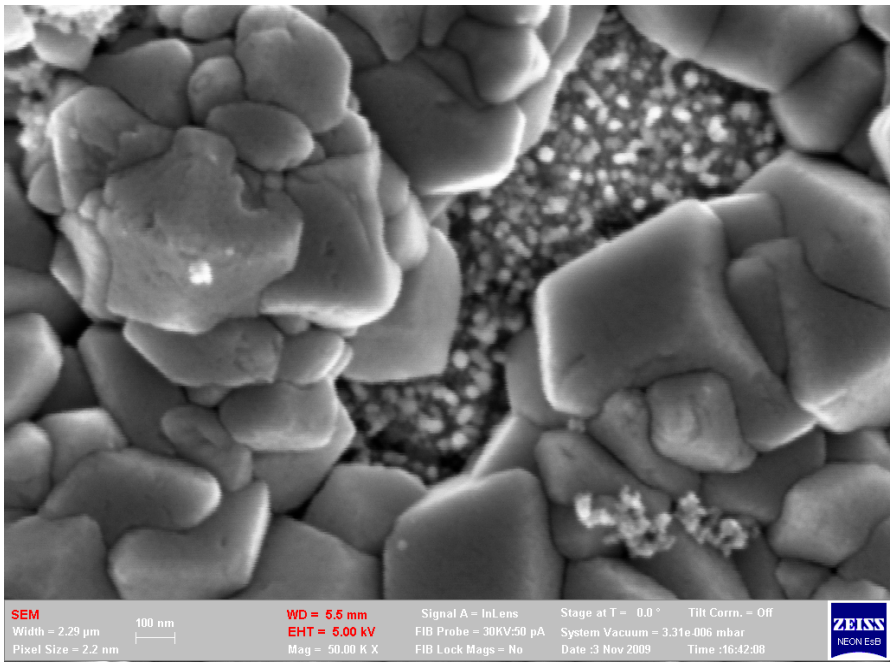


Figure 2-40 Morphology of the carbon steel surface at 50,000x magnification and 5 kV after 36 hours in 30 g/L NaCl solution deaerated with nitrogen at pH 6, in the JIC at 80$^{o}$C.

Magnetite was confirmed previously using Raman spectroscopy as being the corrosion product in the scale in the absence of carbon dioxide. However, a different analytical method using the SR-GIXRD was employed to confirm the identity of this scale layer in nanometers. The Bragg reflection of the scale was obtained at incidence angles of 0.5$^{o}$ (near the surface) and 1.85$^{o}$ (a deeper sampling) and reported in Figure 2-41. At the incidence angle of 0.5$^{o}$, it shows the predominant Bragg reflection of magnetite at the 2-theta angle of 11.8, 19.4, 22.8, 23.8, 27.5, 34.0, 36.2, 39.5, 44.165, 46.0, 48.8, 53.0, 54.6, 56.9, 62.1, 64.3, 69.3 and 71.1. At a higher depth of penetration, the magnetite peaks and the α-Fe from the steel substrate peaks at 28.6, 40.8, 50.6, 59.1, 66.9 and 74.3 were evidenced. In fact, the presence of magnetite being the only crystalline material detected by SR-GIXRD in the scale justified the semiconductive behaviour seen in the impedance spectra.

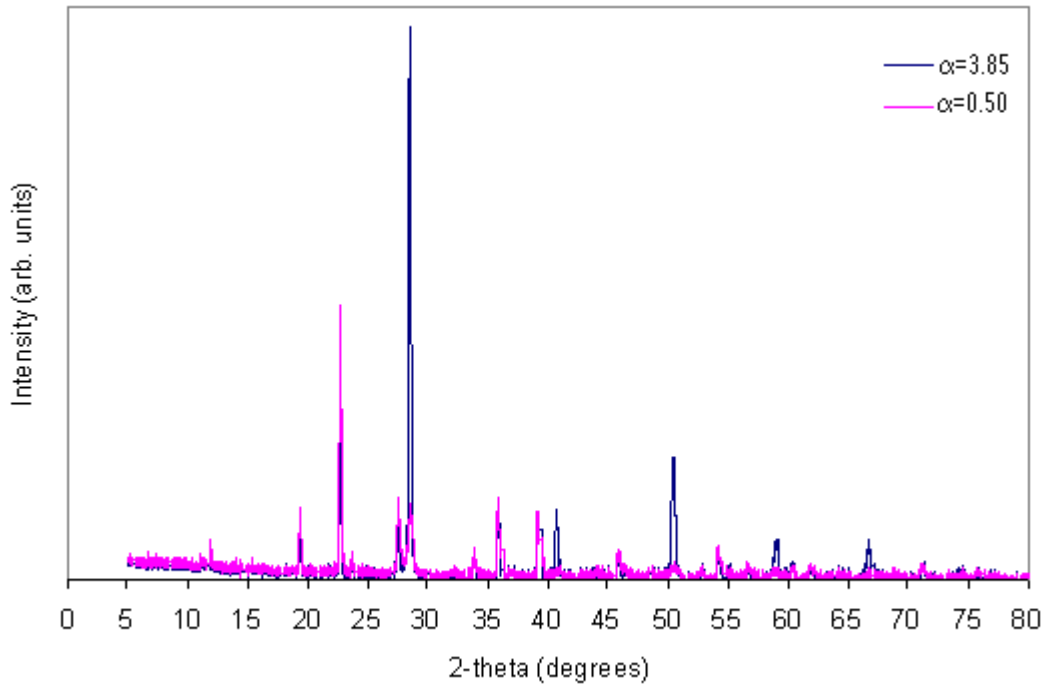


Figure 2-41 SR-GIXRD diffraction patterns at λ = 1 Å of the carbon steel electrode after 36 hours in 30 g/L NaCl solution deaerated with nitrogen at pH 6, in the JIC at 80°C.

### 2.3.3. In-situ SR-GIXRD study of scale development

Previous in-situ synchrotron studies by De Marco et al. (De Marco et al., 2005) showed the formation of chukanovite as the initial corrosion product and the subsequent formation of iron carbonate in $CO_2$ corrosion of carbon steel, but magnetite was not detected. The Pourbaix diagram of Fe-$H_2O$ in Figure 2-1 suggests that magnetite can be formed if the pH and potential are within the condition that favours the formation of magnetite. As the test conditions of De Marco were at pH 4.87 and potential range of -700 mV which are out of the magnetite stability region, magnetite was not detected in his test. Since chukanovite is a fairly newly discovered product there has not been much research to provide reliable thermodynamic data. Therefore, chukanovite is yet to be included in the Pourbaix diagram.

A new set of in-situ GIXRD synchrotron tests incorporating EIS were run in a standard brine solution containing 30 g/L of NaCl and 0.1 g/L of $NaHCO_3$, saturated with the low partial pressure of the $CO_2$ to the pH of 6 and at 45$^{o}$C. The results from the EIS measurements are shown in Figure 2-42. Two capacitive loops appeared on the Nyquist plot at the first hour of the test. The emergence of the double capacitive loops was an indication of a prepassivation process and the analysis of the SR-GIXRD results in the later discussion would justify the identification of the reaction occurring on the carbon steel surface.

As this test was conducted under dynamic flow of fluid and at 45$^{o}$C, it would be expected to show some differences in the scale development from the previous stagnant autoclave test results at 80$^{o}$C. The Nyquist plots changed with time. Initially, the two time constants were apparent but the second time constant disappeared after 2 hours. At subsequent hours, the second time constant became unclear as the data points at low frequency were quite noisy. In addition, the results from the impedance spectroscopy suggest that the scale development process consists of four stages. First, the two capacitive loops signified a prepassivation process with the formation of a porous phase during the first 2 hours. The presence of this porous phase increased the corrosion rate of the carbon steel as the charge transfer resistance of the steel represented by the first time constant was considerably reduced. Second, the porous phase transformed from an amorphous phase to a

crystalline phase as shown by the concurrent GIXRD results. During this transformation, the resistance of the first time constant remained fairly constant but the second semicircle was not clearly observable because of the random response towards the low frequency region. Nevertheless, the semicircle was depressed which again implied a diffusion limit through a porous layer (Turgoose & Cottis, 1993).

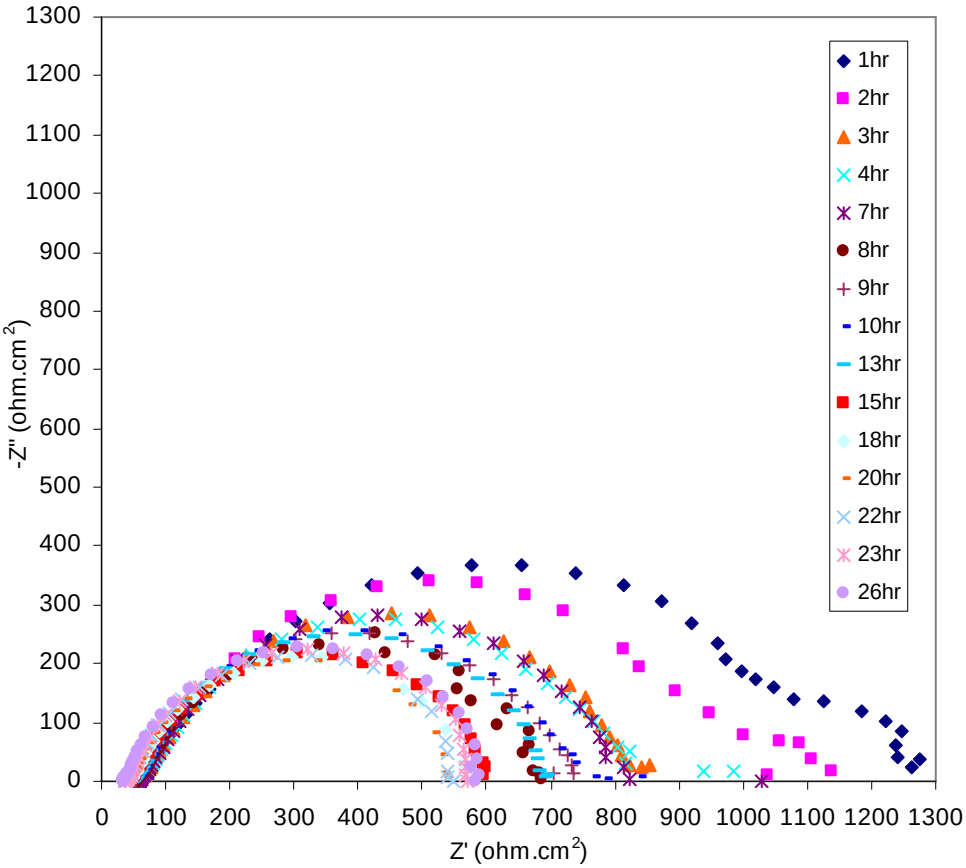


Figure 2-42 Nyquist plots for carbon steel exposed to standard brine solution, saturated with low partial pressure of $CO_2$ at pH 6 and at 45$^{o}$C.

Third, another phase was formed with a noisy response at the low frequency region of the first semicircle during the 8$^{th}$ hour. As the new phase was developing, the anodic reaction of the steel was suppressed, resulting in an increase charge transfer resistance. The retardation of the iron oxidation reaction could be a result of another anodic reaction occurring on the steel surface. The presumable anodic reaction would be the formation of magnetite from the Schikorr reactions (Lee et al., 2006).

Once the transformation was completed, the charge transfer resistance of the steel as seen starting from the 13$^{th}$ hour had decreased with a more depressed semicircle on

the Nyquist plot. Fourth, the build-up of the corrosion product finally spread over the steel substrate and blocked off the active steel surface. The carbon steel began to passivate after 20 hours as the charge transfer resistance increased gradually.

These hypothesized scale development stages are justified by the in-situ analysis of corrosion products using the SR-GIXRD. The diffraction patterns from the corroding carbon steel surface over a period of 22 hours are presented in Figure 2-43 to Figure 2-45 with the intensity registered as arbitrary units, as they were scaled for qualitative analysis. The SR-GIXRD was first aligned with the blank X-65 carbon steel electrode in the electrochemical cell, showing the diffraction peaks of α-Fe at 2-theta angles of 28.6, 40.8, 50.6, 59.1, 67.0 and 74.4. Then, the kapton film was placed on top of the electrode to seal the electrochemical cell. The diffraction pattern of the electrode was obtained with the predominant Bragg reflection of the α-Fe and the broad peaks at 2-theta angles of 9.8, 14.6 and 17.3 from the polycrystalline kapton film. The circulation of the standard brine solution in the electrochemical cell was commenced. The diffraction pattern of the carbon steel was then collected after 2 hours of corrosion. The Bragg reflection of the steel substrate and the kapton film remained on the diffraction patterns with an additional new phase at the 2-theta angle of $7.6^{o}$. This peak matched with the 2-theta angle of the $Fe_2(OH)_2CO_3$ (120) face. The broad peaks contributed by the polycrystalline kapton film caused an ambiguity in identifying new peaks if they fall in the kapton range from $9^{o}$ to $16^{o}$. The relative intensity of the peaks at 2 hour to 4 hours was the same. The intensity of the peak at 2-theta angle of $7.6^{o}$ [$Fe_2(OH)_2CO_3$ (120)] was diminishing with time and a new face at $24.6^{o}$ [$Fe_2(OH)_2CO_3$ (400)] was surfacing. The emergence of diffraction from this face coincided with the disappearance of the second time constant on the impedance spectra. The development of signal from the [$Fe_2(OH)_2CO_3$ (120)] face corresponded to a higher pore resistance but was also accompanied by a drop in charge transfer resistance of the carbon steel.

Identification of the $Fe_2(OH)_2CO_3$ diffraction peaks justified the prepassivation product development from electrochemical reactions which corresponded to the EIS respond with a second small capacitive loop in the low frequency region. However, the transformation of the crystal phase orientation had no direct link to the EIS respond but the specific diffraction data development leads to the deduction the prepassivation process.

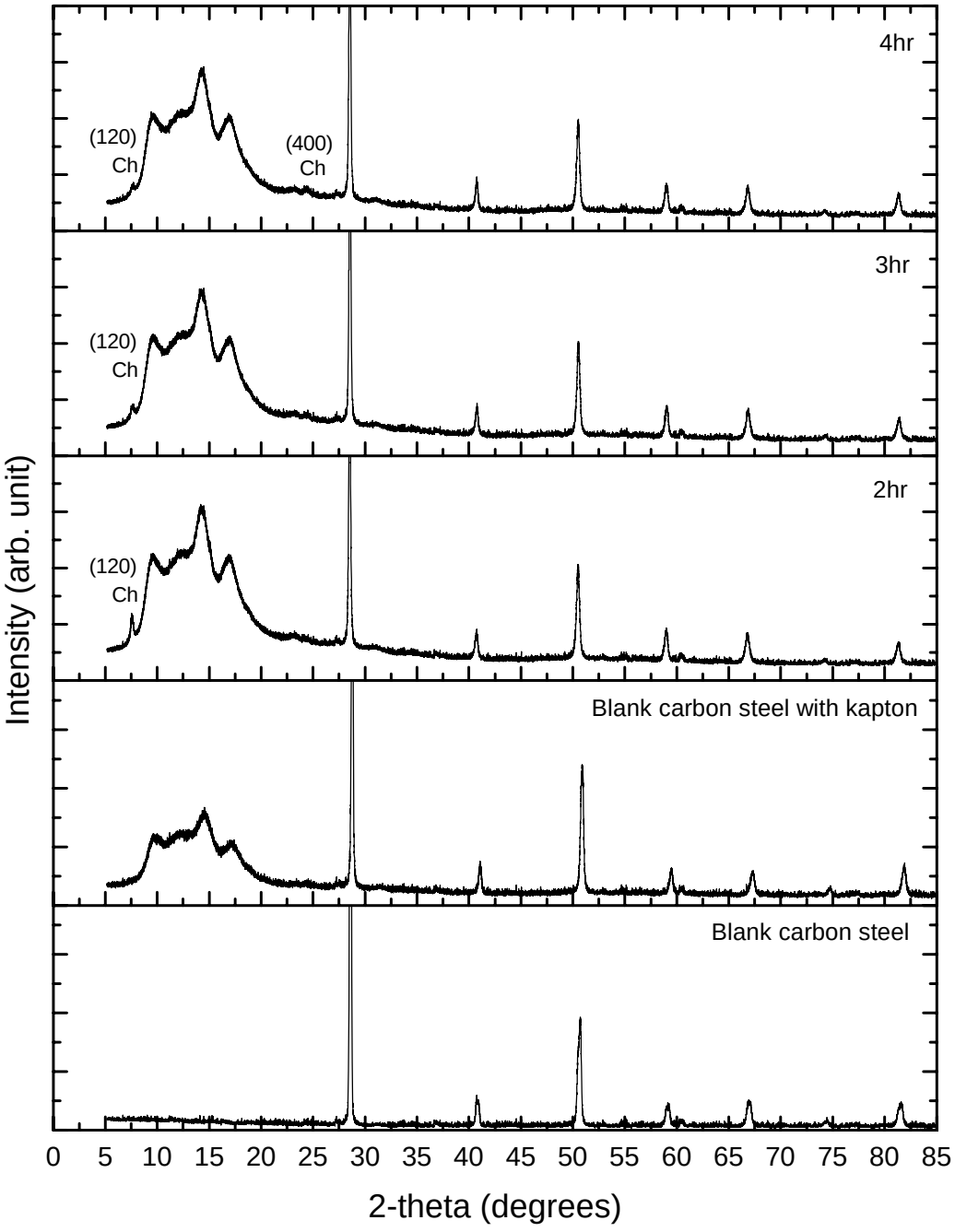


Figure 2-43 SR-GIXRD diffraction patterns at α = 0.5° and λ = 1 Å of the calibrated X-65 carbon steel, under 4 hours of corrosion in standard brine solution at 45$^{o}$C, saturated with high-purity nitrogen and carbon dioxide gas mix to pH 6.

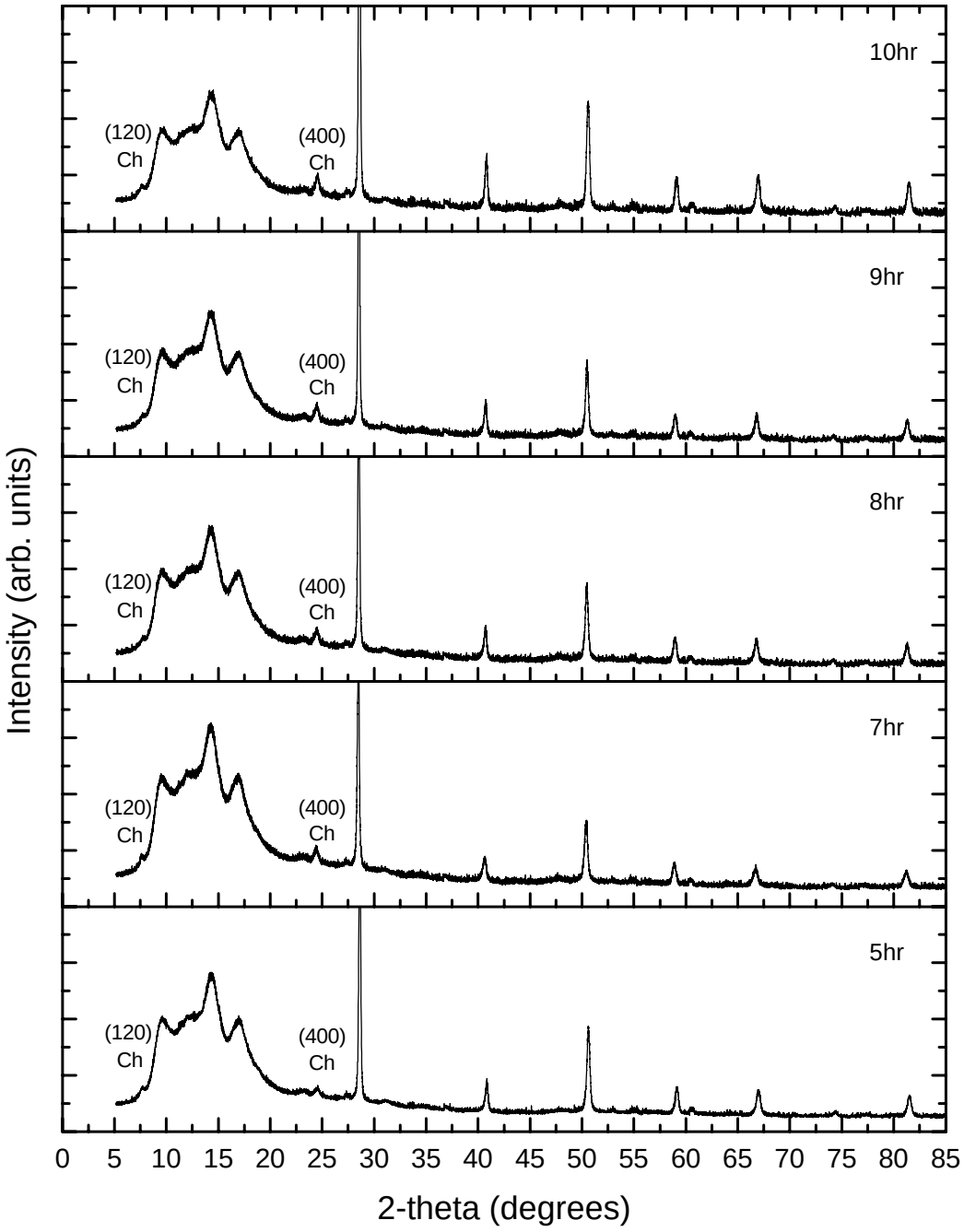


Figure 2-44 SR-GIXRD diffraction patterns at $\alpha = 0.5°$ and $\lambda = 1$ Å of a corroding X-65 carbon steel from 5 to 10 hours in standard brine solution at 45$^{o}$C, saturated with high-purity nitrogen and carbon dioxide gas mix to pH 6.

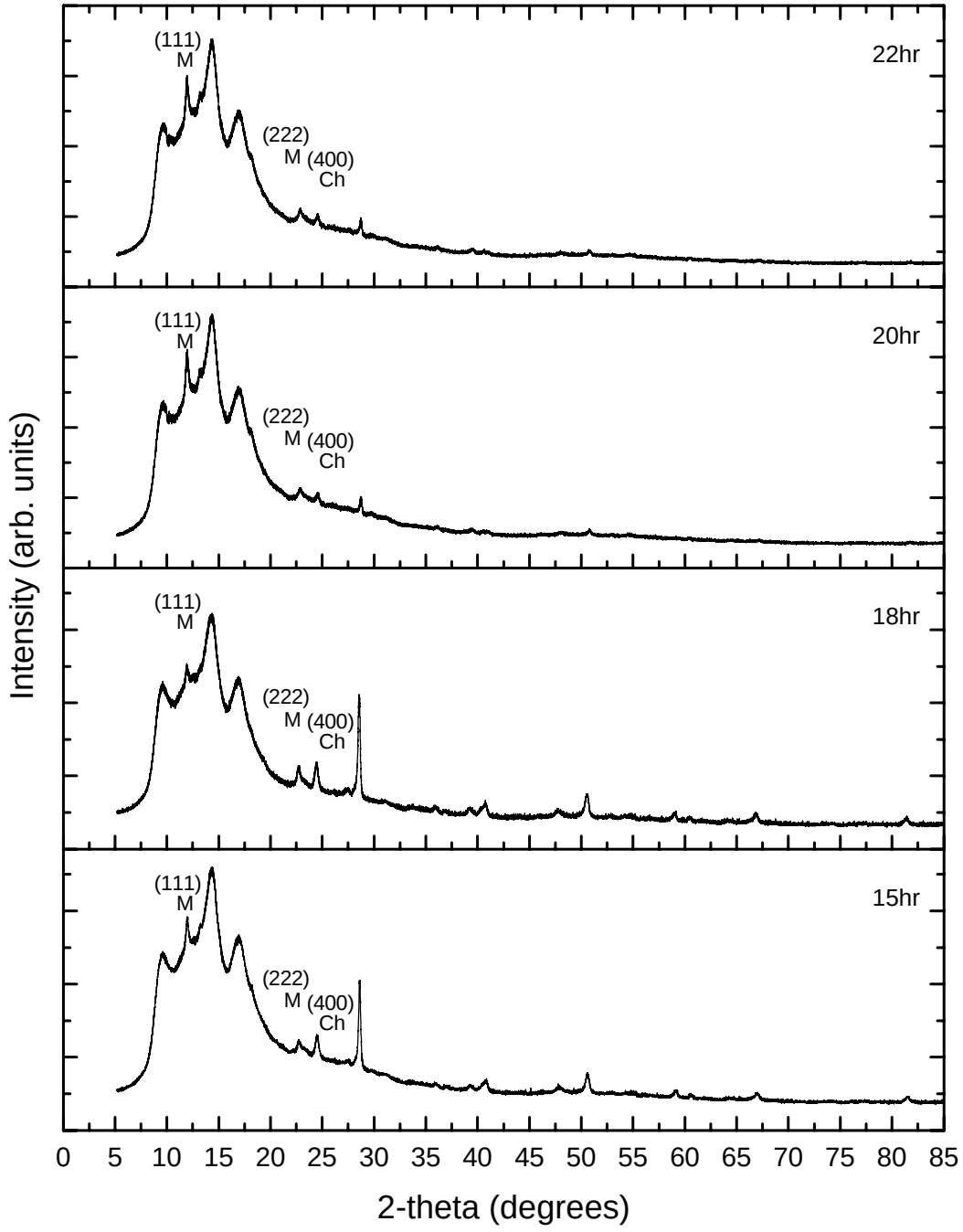


Figure 2-45 SR-GIXRD diffraction patterns at $\alpha = 0.5°$ and $\lambda = 1$ Å of a corroding X-65 carbon steel from 15 to 22 hours in standard brine solution at 45$^{o}$C, saturated with high-purity nitrogen and carbon dioxide gas mix to pH 6.

Once the diffraction pattern corresponding to the [$Fe_2(OH)_2CO_3$ (400)] face had developed, the charge transfer resistance stayed fairly constant until around the 8$^{th}$ hour, when the charge transfer resistance dropped again. No new peaks were observed until later at the 15$^{th}$ hour. After 15 hours two new peaks at the 2-theta angles of 11.8$^o$ [$Fe_3O_4$ (111)] and 23.9$^o$ [$Fe_3O_4$ (222)] were apparent and the intensity of the $\alpha$-Fe peaks was suppressed. The charge transfer resistance stayed constant as each transformation reaction was taking place, and dropped again once a new phase was observed. When magnetite was formed, the charge transfer resistance continued to fall until most of the $\alpha$-Fe diffraction peaks had subsided after 25 hours of corrosion. The disappearance of the $\alpha$-Fe diffraction peaks revealed a state of passivation as the active carbon steel surface was covered with corrosion product scale. Therefore, the corrosion rate of the steel began to decline. The formation of new phases caused an estimated 57% drop in charge transfer resistance under flowing conditions which was equivalent to a 75% increase in corrosion rate, before the steel surface was passivated by the corrosion product scale.

The depth profiles of the carbon steel taken every five hours are shown in Figure 2-46 to Figure 2-48. The development of the $Fe_2(OH)_2CO_3$ phase can be seen in Figure 2-46 with the diffraction peak at 7.6$^o$ [$Fe_2(OH)_2CO_3$ (120)] only apparent at higher depth of penetration. Whereas, the [$Fe_2(OH)_2CO_3$ (400)] at 24.6$^o$ became the preferred face orientation as the structure of this product continued to develop. On the other hand, the development of the magnetite phase is evidenced at the 15$^{th}$ hour. The diffraction peak at 23.9$^o$ [$Fe_3O_4$ (222)] is the initial peak of the magnetite phase and this peak is present at all depths of penetration in Figure 2-48. However, the latter diffraction peak at 11.8$^o$ [$Fe_3O_4$ (111)] is not noticeable at higher depth of penetration. Again, iron carbonate is not detected in this 22 hours test. Since iron carbonate has a low solubility product of 9.4x10$^{-12}$ estimated at 45$^o$C, it would require at least 0.189 mol/L of $Fe^{2+}$ to exceed its solubility limit for the precipitation reaction to take place.

The combined results from both the electrochemical techniques and chemical analysis were in agreement that new phases were formed during the corrosion process in a mildly acidic environment. Nevertheless, the hypotheses made

previously from the ex-situ studies have been justified by this powerful in-situ SR-GIXRD cum EIS technique.

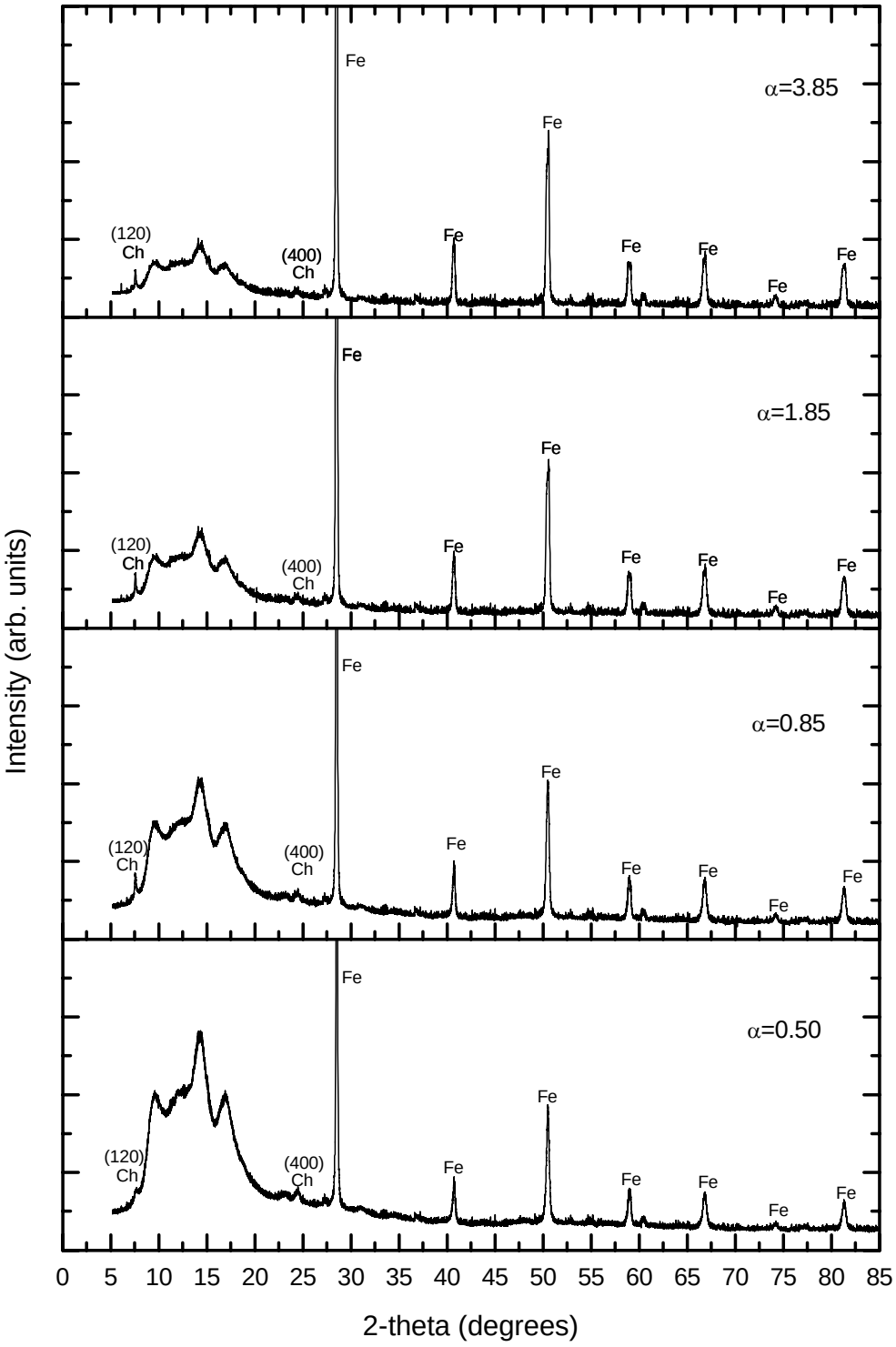


Figure 2-46 SR-GIXRD depth profile of corroding X-65 carbon steel at α = 0.5°, 0.85°, 1.85° and 3.85° and λ = 1 Å at the 5$^{th}$ hour.

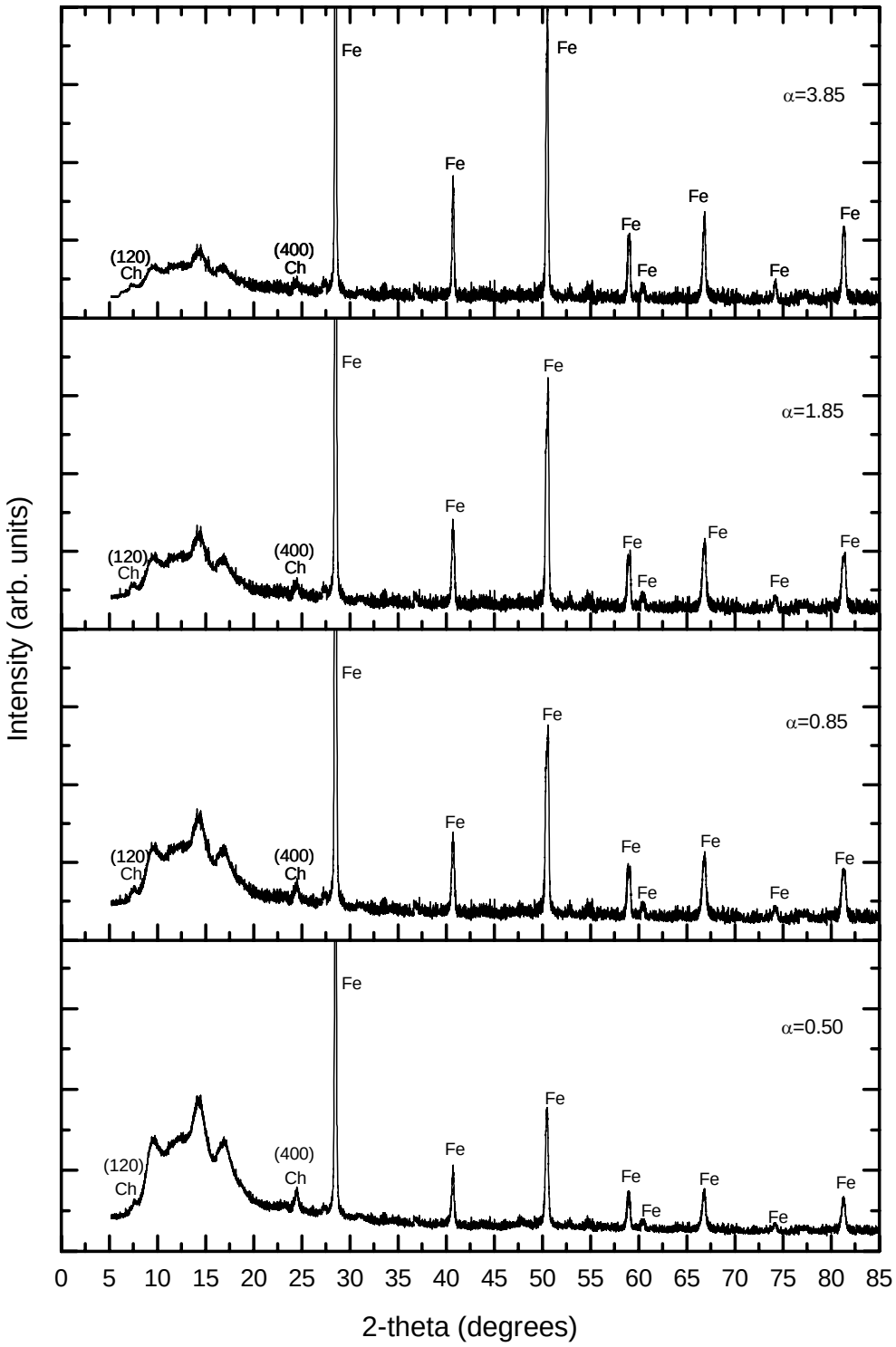


Figure 2-47 SR-GIXRD depth profile of corroding X-65 carbon steel at α = 0.5°, 0.85°, 1.85° and 3.85° and λ = 1 Å at the 10$^{th}$ hour.

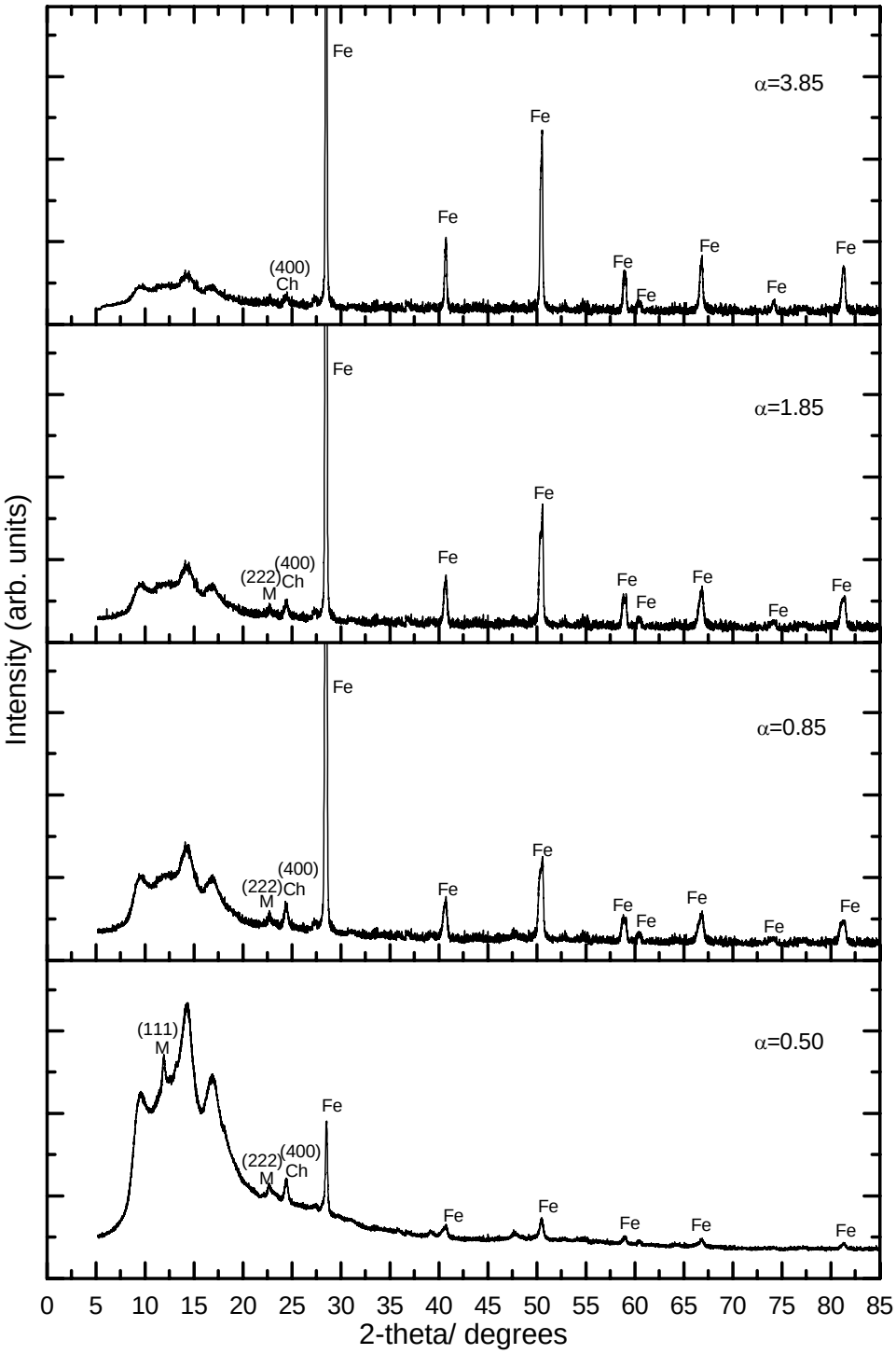


Figure 2-48 SR-GIXRD depth profile of X-65 corroding carbon steel at α = 0.5°, 0.85°, 1.85° and 3.85° and λ = 1 Å at the 15$^{th}$ hour.

## 2.4. CONCLUSIONS

Analysis of corrosion product scales, formed at 150$^{o}$C and under low $CO_2$ partial pressures, using the complementary techniques of Raman spectroscopy and SEM / EDS shows the presence of both iron carbonate and magnetite. It is theorized that magnetite was formed via an electrochemical reaction pathway whilst iron carbonate precipitated over the underlying magnetite scale when the solubility limit of iron carbonate was exceeded. Under a nitrogen atmosphere in mildly acidic solutions in the absence of carbonate, magnetite was found to be the sole solid corrosion product formed. Although the magnetite scale formed an incomplete coverage, it was found to be relatively stable in air and the octahedral structure of magnetite was clearly projected under the SEM.

Study of the morphology of scale formed at 80$^{o}$C under low partial pressure of $CO_2$, pH 5.5 using the SEM was unable to identify the presence of any crystals and it appeared as if there was no corrosion product scale formed on the carbon steel surface. However, the emergence of double capacitive loops on the EIS Nyquist plots indicated a prepassivation event owing to the formation of a new phase on the steel surface. Thus, a FESEM was employed and this revealed the presence of a nano crystalline and lath-like structure covering the entire steel surface. The identity of the lath-like structure was confirmed using a combination of EDS, Raman spectroscopy and SR-GIXRD to be the chukanovite ($Fe_2(OH)_2CO_3$) phase.

A consistent sudden increase in the open circuit potential in the in-situ autoclave test with and without the presence of carbonate was due to the development of an unstable magnetite phase. In the absence of carbon dioxide, the scale formed comprised only magnetite and the two time constants Nyquist plot was slightly different from that when the scale formed under carbon dioxide. The impedance spectra fitted well to the semiconductor equivalent circuit which suggests that the magnetite scale formed was semiconductive. Whereas, the reversal of the sequence of the two capacitive loops on the EIS Nyquist plots of the scale formed in the presence of carbon dioxide suggests that the passive scale might not be conductive.

The in-situ SR-GIXRD and EIS study of the scale development showed the appearance of the second time constant was associated with the $Fe_2(OH)_2CO_3$ (120) face at the 2-theta angle of 7.6$^o$. At the third hour, the second capacitive loop on the EIS Nyquist plot and the peak at 2-theta angle of 7.6$^o$ diminished simultaneously with the appearance of a new peak at 24.6$^o$ due to [$Fe_2(OH)_2CO_3$ (400)]. The formation of this chukanovite phase has caused a drastic drop in the polarisation resistance of the steel. At the 8$^{th}$ hour, a new phase was formed with a noisy response at the low frequency region. This corresponded to the two new peaks at the 2-theta angle of 11.8$^o$ [$Fe_3O_4$ (111)] and 23.9$^o$ [$Fe_3O_4$ (222)]. Those peaks had become fully developed after the 15$^{th}$ hour. The charge transfer resistance of the steel increased slightly during the formation of the magnetite phase. The retardation of the iron oxidation reaction could be a result of an additional oxidation reaction of the hydroxide phase to magnetite. The charge transfer resistance continued to drop once this magnetite phase was fully developed. Then the charge transfer resistance rose again as the steel was passivated by the mixture chukanovite and magnetite phase with the disappearance of the $\alpha$-Fe peaks.

In summary, corrosion product scales formed on carbon steel under mildly acidic carbon dioxide conditions undergo three different types of reaction. Firstly, ferrous ions from the oxidation reaction of the carbon steel are hydrolysed. A porous hydroxide compound is formed via the hydrolysis reaction and $Fe_2(OH)_2CO_3$ is the preferred product formed in the presence of carbonate ions in the solution. Secondly, magnetite is formed via an electrochemical reaction when the conditions for the formation of stable magnetite are met. Thirdly, the precipitation reaction of iron carbonate proceeds when the iron carbonate exceeds its solubility limit.

# CHAPTER 3 GALVANIC CORROSION OF CARBON STEEL CAUSED BY COUPLING MAGNETITE

## 3.1. INTRODUCTION

### 3.1.1. Galvanic corrosion

Galvanic corrosion is commonly thought of an accelerated corrosion due to two dissimilar metals being coupled in a corrosive environment. There are three main conditions for galvanic corrosion to occur:

1) at least two different conductive materials
2) electrical contact to allow current to flow between them
3) the presence of a corrosive medium or electrolyte.

Galvanic corrosion can be beneficial if the application is used appropriately. This concept has been applied successfully for decades in the marine industry in cathodic protection.

It is not widely recognized that many corrosion products are electrically conductive and more noble in the electrochemical series than the steel. The corrosion product can therefore furnish a galvanic coupling, resulting in galvanic corrosion. In oil and gas production, the influence of carbon dioxide, hydrogen sulphide and seawater environments on the formation of a semiconductive iron sulphide scale and iron carbide layer are widely reported (Baboian, 1976b). Often, the presence of other corrosion product scales, that are electrically conductive can potentially cause galvanic corrosion failures in the oil and gas production pipelines, has been overlooked.

The galvanic effect of magnetite on carbon steel has been studied previously in relation to the high temperature and high pressure boiler industry. In fact, the studies showed that the coupling of magnetite to carbon steel caused galvanic corrosion on carbon steel (Al-Mayouf, 2006; Al-Mayouf et al., 2007; Fushimi, Yamamuro, & Seo, 2002). It must be pointed out that these studies were concerned with corrosion by

oxygen. No studies addressed the effect of the galvanic coupling of magnetite and mild steel under carbon dioxide conditions on the corrosion rate.

Therefore, the factors affecting the galvanic corrosion of carbon steel caused by coupling of magnetite which include the cathode to anode surface area ratio and the effect of carbon dioxide partial pressures were studied. In addition, the inhibition effect from a range of generic inhibitors and commercial inhibitors on the galvanic corrosion was investigated.

### 3.1.2. Electronic properties of corrosion products

The conductivity of a corrosion product scale is determined by the energy gap between the upper edge of the valence band (highest occupied energy level) and the lower edge of the conduction band (lowest unoccupied energy level) of the molecular orbitals. A semiconductive corrosion product scale, unlike a metal which has a readily occupied conduction band due to the overlapping of the conduction and valence bands, requires a low band gap for the electrons to promote easily from the valence band to the conduction band (Bott, 1988). However, temperature can affect the electrical properties of a corrosion product scale by either increasing or restricting the mobility of the electrons between the valence band and conduction band. At absolute zero temperature, most semiconductors will be insulators whilst at high temperature, some semiconductors or even insulators can become conductive due to thermal or photochemical excitation of the electrons from the valence band to the conduction band (Bott, 1988).

Corrosion product scales may exhibit a range of conductivities depending on the degree of stoichiometry, and they can be classified into three categories: conductor, insulator and semiconductor. Both conducting and semiconducting products may be at risk of generating a galvanic influence to the corrosion process (Cornell & Schwertmann, 1996; Wilhelm, 1988). Most oxide and sulfide corrosion products, as shown in Table 3-1, fall in the category of semiconductor as they derive conductivity from non-stoichiometry with their band gaps ranging between 1 eV and 4 eV, which is within the characteristic band gap of less than 5 eV for semiconductors (Cornell &

Schwertmann, 1996; Wilhelm, 1988). Semiconductors are divided into two types which are p-type and n-type semiconductors. The conductivity of a p-type semiconductor is mainly via holes. P-type semiconductors are metal ion deficient and function more readily as an anode. In contrast, the conductivity of an n-type semiconductor is mainly via electrons. N-type semiconductors are oxygen or sulphur deficient and the promotion of charge transfer is via the donation of electrons in the conduction band to solution species. Additionally, n-type semiconducting corrosion product scales are at risk of causing localised attack due to the ability of the surface film to support the reduction reactions of $O_2$ or $H^+$ and provide a galvanic influence to the corrosion process (Baboian, 1976b).

Table 3-1 Electronic properties of iron corrosion products (Schoonen, 2000; Wilhelm, 1988)

| Product | Formula | Electronic property | Band gap (eV) |
|---|---|---|---|
| Goethite | $\alpha$-FeOOH | n/a | 2.1 |
| Lepidocrocite | $\gamma$-FeOOH | n/a | 2.06 |
| Hematite | $Fe_2O_3$ | n-type semiconductor | 2.2 |
| Magnetite | $Fe_3O_4$ | n or p type semiconductor | 0.1 |
| Maghemite | $\gamma$-$Fe_2O_3$ | n-type semiconductor | 2.03 |
| Wüstite | FeO | p-type semiconductor | 2.3 |
| Pyrite | $FeS_2$ | Conductor | 1.2 |
| Troilite | FeS | p-type semiconductor | 0.1 |
| Greigite | $Fe_3S_4$ | n/a | 0 |

Many corrosion product scales show the characteristic of a semiconductor if their electrical resistivity at room temperature is in the range from $10^{-2}$ to $10^{9}$ ohm.cm (Kittel, 2005) and the band gap energy is less than 5 eV (Cornell & Schwertmann, 1996). Interestingly, most iron oxides are intrinsic semiconductors with the band gap energy below 3 eV at standard conditions, as listed in Table 3-1. These corrosion products have the ability to serve as surface electrodes when the product layers are greater than 5 nm thick (Wilhelm, 1988). Iron carbonate, however, has been reported as an insulator (Crolet, Thevenot, & Nesic, 1998) but the band gap energy of this product has never been determined. Apart from iron carbonate, the electrical property

of chukanovite is still unknown and to date there have been limited studies done on this product.

### 3.1.3. Factors governing galvanic corrosion

The principle of galvanic corrosion can be explained by mixed potential theory as presented by Baboian (Baboian, 1976a), Oldfield (Oldfield, 1988) and Efird (Efird, 1988). The anodic and cathodic reactions occur at different sites, connected through the electronic conduction of the coupled material. Every material has its own corrosion potential when it is at steady state with the electrolyte. When two different conductive materials are electrically coupled in the same electrolyte, both materials will be polarized at a new rate with a resultant mixed potential where the total oxidation rate is in balance with the total reduction rate. The use of mixed potential theory can also provide qualitative information on galvanic corrosion

The controlling mechanisms in a galvanic corrosion system depend upon the anodic and cathodic polarization, potential drop in the solution and the total potential difference between the coupled materials. There are four controlling modes of galvanic corrosion as illustrated in Figure 3-1: cathodic control, anodic control, resistance control and mixed control (Zhang, 2000).

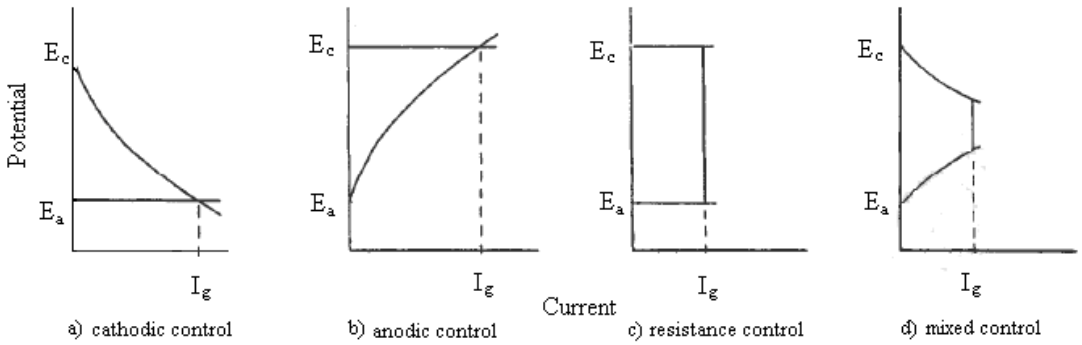


Figure 3-1 Polarisation curves of different type of control of galvanic corrosion reactions: a) cathodic control, b) anodic control, c) resistance control and d) mixed control (Zhang, 2000).

Under cathodic control, the cathode polarizes and the current flow is controlled entirely by the cathode in solutions of low resistivity whilst the anode does not have

any influence. Galvanic corrosion under anodic control is the reverse where the anode polarizes and not the cathode. If neither of the electrodes polarizes and the current flow is controlled by the resistivity of the path for instance, solution resistance - the system is under resistance control. It is common that the galvanic system is under mixed control which is a combination of the solution resistance and anodic or cathodic polarization (Zhang, 2000).

#### 3.1.3.1. Carbon dioxide partial pressure

The carbon dioxide concentration in the water phase of the oil and gas wells can vary significantly depending on the depth of a well, temperature and carbon dioxide partial pressure. Thus, the acidity of the water phase varies according to the dissolved carbon dioxide level. The carbon dioxide partial pressure has minimal effect on the cathodic polarization curve but it affects the occurrence of passivating corrosion product scales such as iron oxides and iron carbonate which are a complex function of temperature, carbon dioxide partial pressure and pH. The presence of a corrosion product could potentially affect the galvanic current through an increased ohmic resistance and a positive shift in the free corrosion potential (Baboian, 1976b).

#### 3.1.3.2. Cathode to anode surface area ratio

The cathode to anode surface area ratio causes a major effect on the galvanic corrosion rate. An illustration of the galvanic couple on an Evans diagram is shown in Figure 3-2 (Baboian, 1976a). The cathodic current curve of the cathode shifts according to the size of the cathode as the total current is simply the product of the current density by the area. Therefore, a large cathode provides large total current and the current line is shifted towards higher current. The intersection of the anodic line of the anode with the cathodic line of the cathode gives the mixed potential of the couple and the corrosion current.

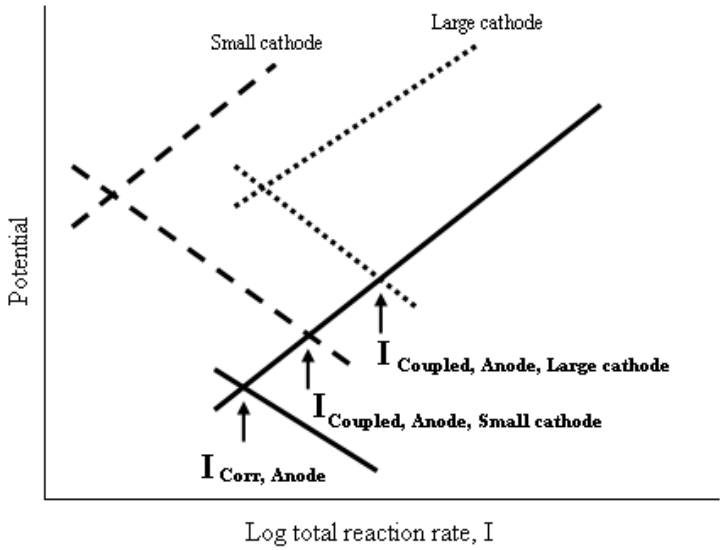


Figure 3-2 Evans diagram of effect of cathode to anode surface area ratio on couple current (Baboian, 1976a).

According to Faraday's law, the corrosion penetration rate is proportional to the cathode to anode surface area ratio in the following equation:

$$i_{corr} = i_{ox} = \frac{A_c}{A_a} i_{red}$$ Equation 3-1

Where,

$i_{corr}$ = corrosion current density ($A/cm^2$)

$i_{ox}$ = oxidation current density ($A/cm^2$)

$i_{red}$ = reduction current density ($A/cm^2$)

$A_c$ = cathode area ($cm^2$)

$A_a$ = anode area ($cm^2$)

If the cathode area is large, the cathode current line will appear far to the right in Figure 3-2 and intersect on a higher anodic current line of the anode with the mixed potential shifted towards higher anodic potential. The vice versa also applies. As a rule of thumb, a small anode and large cathode is undesirable as it causes higher galvanic corrosion rate.

### 3.1.4. Inhibition of galvanic corrosion

The galvanic effect of magnetite on carbon steel was studied previously in the application of high temperature and high pressure boiler industry, where it was found that the coupling of magnetite to carbon steel caused galvanic corrosion of the carbon steel (Al-Mayouf, 2006; Al-Mayouf et al., 2007; Fushimi, Yamamuro, & Seo, 2002). Therefore, mitigation of the galvanic corrosion is essential to prevent unnecessary disaster due to premature pipeline failure.

Galvanic corrosion can be inhibited by the adsorption of the surfactant functional group onto a metal surface through a variety of mechanisms that may involve the blockage of the anodic or cathodic sites of the corrosion reaction, the reduction of the porosity of the surface film or retardation to the transport of reactant species (S. Ramachandran & V. Jovancicevic, 1999b). The ability of a surfactant molecule to adsorb can be related to the ability of surfactant molecules to aggregate to form micelles. Field tests and laboratory research found that the inhibitor performance exhibits a plateau at or above the critical micelle concentration (CMC), corresponding to that observed with surfactant adsorption on homogeneously charged surfaces (D. John et al., 2006). Further increase in the solution surfactant concentration does not lead to any further increases in the surface excess. Therefore, the inhibitors were tested at concentrations twice the CMC.

Since the galvanic corrosion rates are controlled or limited by different types of reactions, it is crucial to determine the controlling reaction by interpreting the polarization curves as shown in Figure 3-3 (Harvey, 2005). A typical cathodically controlled reaction is where the cathodic site is highly polarised from its equilibrium potential whereas the anodic site is only slightly polarised. Whereas, the anodically controlled reaction is just the reverse.

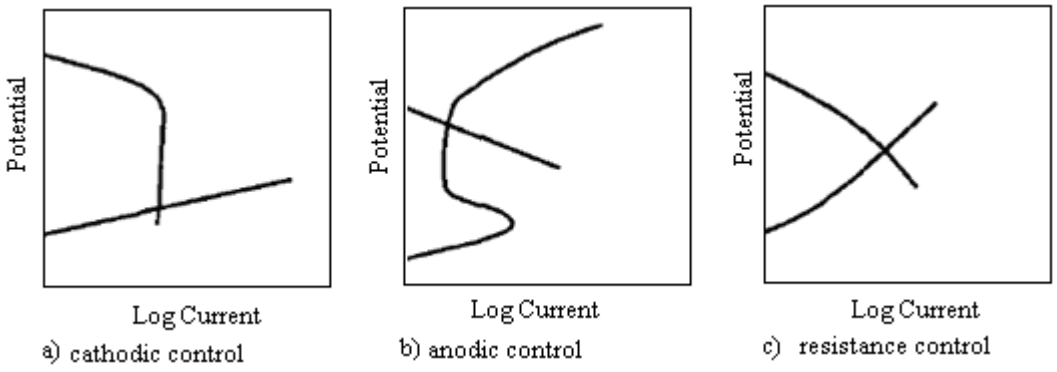


Figure 3-3 Polarisation curves of different type of control of galvanic corrosion reactions: a) cathodic control, b) anodic control and c) mixed control (Harvey, 2005).

Molecular modelling has been extensively utilized to study the inhibitor molecule adsorption on iron carbonate, magnetite and hematite surfaces (S. Ramachandran & V. Jovancicevic, 1999a; S. Ramachandran & V. Jovancicevic, 1999b; Ramachandran et al., 1996, 1997). Simulations were performed by calculating the binding energy of adsorbed water molecules and different inhibitor molecules on the iron carbonate and oxide surfaces. It was found that every $Fe^{2+}$ site of the magnetite surface is favourably bonded by three water molecules by electrostatic and hydrogen bonding. In order for the corrosion inhibitor molecule to bind preferentially to the magnetite surface, and impede water and corrosive ions from migrating to the surface, the water molecules had to be displaced from the oxide surface and replaced by an adsorbed layer of inhibitor molecules (S. Ramachandran & V. Jovancicevic, 1999a).

## 3.2. EXPERIMENTAL

Studies were conducted to determine the effect of electrochemically coupling mild steel electrodes with a magnetite electrode under anaerobic conditions. A rock sample of magnetite from Arkansas Magnet Cove was machined into an electrode with an exposed surface area of 4.9 $cm^2$. Three different sizes of X-65 mild steel electrode with surface areas of 3.05 $cm^2$, 1.2 $cm^2$ and 0.66 $cm^2$ (cathode to anode surface ratio of 1.61, 4.09 and 7.44) were constructed. The test was performed in a standard rotating cylinder electrode (RCE) cell setup for linear polarization measurement which comprised a temperature controller, a platinum mesh counter electrode, a silver/silver chloride reference electrode and both the magnetite and mild steel electrodes as working electrodes. The working mild steel electrode was inserted in a rotating shaft, positioned in the centre of the cell, with both the reference and working magnetite electrodes aligned close to one another to minimise IR drop across the electrodes. The IR drop effect was however been offset by the relative comparison of the results from the same experimental setup. A glass cell was filled with 1 L of 30 g/L NaCl electrolyte buffered with 0.1 g/L of $NaHCO_3$ and deaerated with $CO_2$ gas under atmospheric pressure at 30$^oC$. A standard sample preparation of the mild steel electrodes was applied. First, the steel electrode was polished with a 600 grit grinding paper. Then the electrode was rinsed with ethanol, degreased with acetone, dried in the oven at 70$^oC$ for 10 minutes and then cooled in a desiccator. The weight of the electrode was recorded before and after the test for weight loss measurement.

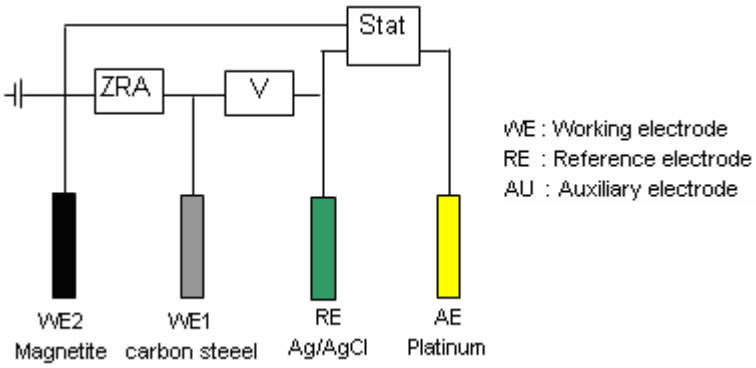


Figure 3-4 Circuit diagram of the galvanic test configuration.

An ACM Gill 12 potentiostat with built in zero resistance ammeter (ZRA), automated by the Sequencer software, was used to measure the galvanic current of

the coupling and the linear polarization resistance (LPR) of the mild steel electrode. A schematic diagram of the test configuration is shown in Figure 3-4. The mild steel electrode was set to rotate at 1000 rpm. A program was developed in the Sequencer software to measure the galvanic current from the coupling for 3600 s followed by LPR measurement, repeated 5 times. The magnetite electrode was consistently decoupled from the Gill instrument during linear polarization measurement in order to determine the self corrosion rate of the mild steel electrode.

The effect of carbon dioxide partial pressure on galvanic corrosion was tested using a series of carbon dioxide/nitrogen gas mixtures which were produced by adjusting the flow rate of the respective gases using an Allborg gas flow meter. The following gas mixtures were used: 90:10, 70:30, 50:50, 30:70 and 10:90. The solution was sparged overnight with nitrogen and the changeover to the mixed gas was made one hour before commencing the electrochemical measurements. The solution pH before and after the test was measured using a Cyberscan pH meter.

Six generic inhibitors were studied: cetylpyridinium chloride (CPC), imidazoline, dodecylpyridinium chloride (DPC), thioglycolic acid (TGA), benzyldimethylhexadeclammonium chloride (C16BDMAC) and DPC/TGA mix (1:10 mass ratio), along with ten commercial inhibitors. The experimental setup was similar to the aforementioned procedure with the exceptional of testing on a single cathode to anode ratio of 4.09 (carbon steel electrode area of 1.09 $cm^2$) and also the inhibitor dosed in after 2 hours of blank galvanic corrosion rate measurements. Corrosion inhibitor was added in after LPR measurement upon reconnecting the magnetite working electrode with the mild steel electrode at hourly intervals with a dosage of 10 µL (10 ppm), 10 µL (total of 20 ppm) and 30 µL (total of 50 ppm).

## 3.3. RESULTS AND DISCUSSION

### 3.3.1. Galvanic corrosion from magnetite

Electrochemical techniques have been employed successfully in galvanic corrosion studies to predict the polarization characteristics of the couple by measuring the potential, current and polarization resistance (Baboian, 1976a). Reaction kinetics and limiting reaction rates of the couple can be predicted from electrochemical polarization measurements. Furthermore, the rate of galvanic corrosion can also be governed by factors such as ionic conductivity of the electrolyte, the ratio of areas of anode and cathode sites, mass transport, electrode potential and alloy compositions, etc. Therefore, galvanic corrosion measurement is often conducted under conditions that closely simulate the actual corrosive environment. Unfortunately, the use of electrochemical techniques can sometimes lead to erroneous conclusions because of misinterpretation of data. Hence, it is good to employ conventional techniques such as weight loss to verify the results. The effects of the cathode to anode surface area ratio and carbon dioxide partial pressure were investigated in this research.

#### 3.3.1.1. Effect of cathode to anode surface area ratio

The corrosion behaviour of the galvanic coupling of magnetite with various surface areas of mild steel electrodes was studied under carbon dioxide corrosion. The corrosion rate measured using electrochemical techniques was compared with the conventional weight loss measurement since the use of electrochemical techniques can sometimes lead to erroneous results because of misinterpretation of data. The corrosion rates were calculated by assuming the Tafel constant (B) is 26 mV under mixed controlled carbon dioxide corrosion. The results of the measured corrosion rate of the carbon steel (anode) with different surface areas coupled with a fixed surface area magnetite (cathode) are presented in Figure 3-5. The self corrosion rate of the carbon steel measured from the linear polarization technique was relatively constant under the same test conditions, regardless of the surface area; the galvanic corrosion rate, which was calculated from the measured galvanic current, was increasing with the cathode to anode surface area ratio. The overall corrosion rate determined by the weight loss measurement actually tallied with the summation of both the galvanic and the self corrosion rate. The results also showed that the

galvanic corrosion contributed to a higher overall corrosion rate and this contribution increased upon increasing the cathode to anode surface area ratio. The cathode to anode surface area ratio was reported previously by Al-Mayouf (Al-Mayouf et al., 2007) to be a key factor in the galvanic corrosion of carbon steel coupled to magnetite under anaerobic corrosion conditions. The comprisable results from the weight loss measurement and electrochemical techniques, which shows the overall corrosion rate of the carbon steel, having a direct addition of the self corrosion and the galvanic corrosion, suggests that the galvanic coupling is cathodically controlled.

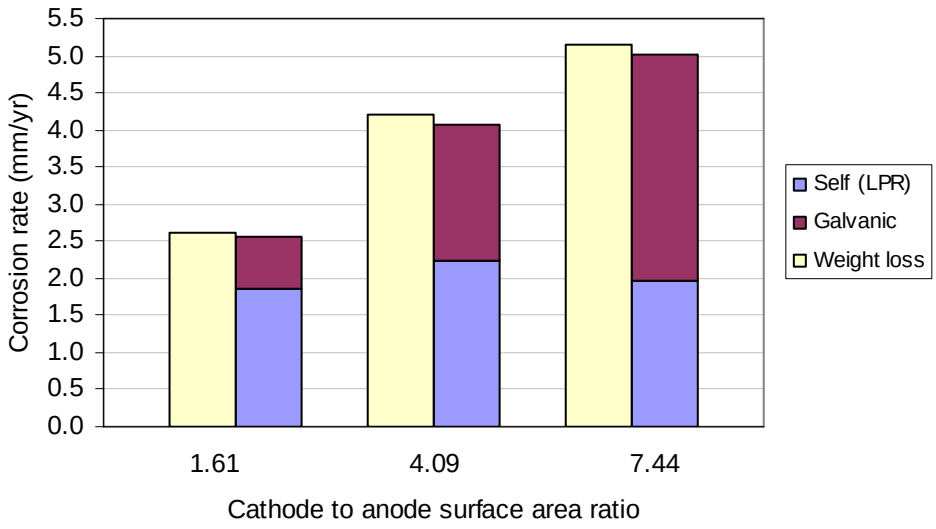


Figure 3-5 Self corrosion and galvanic corrosion rates for different mild steel surface areas.

The average galvanic currents of the coupling with different anode surface areas were measured at hourly intervals and the galvanic corrosion rate was determined by integrating the measured galvanic currents. The results in Figure 3-6 show the consistency in the absolute galvanic current for all three different surface areas of mild steel electrode which implies that a constant galvanic current was passed through the magnetite for all three different anode surface areas. With the supply of constant current from the cathode, the smaller anode had to increase the rate of its oxidation reaction to keep up with the reduction rate, which resulted in an acceleration of the corrosion rate on the smaller anode. On the other hand, the galvanic current was diminishing over time. The current decrease could be a consequence of a reduction event on magnetite surface which could change its

physical, electrical and chemical properties. The reduction event is addressed in chapter 4 on reduction of magnetite.

The consistency in the self corrosion rates shows that cathode to anode surface area ratio effect has no impact to the self corrosion of the carbon steel. However, the galvanic current contribution increased significantly with increasing cathode to anode surface area ratio. The significance of the galvanic current contribution from increasing cathode to anode surface area ratio implies that galvanic corrosion rate of the mild steel is cathodically controlled by magnetite.

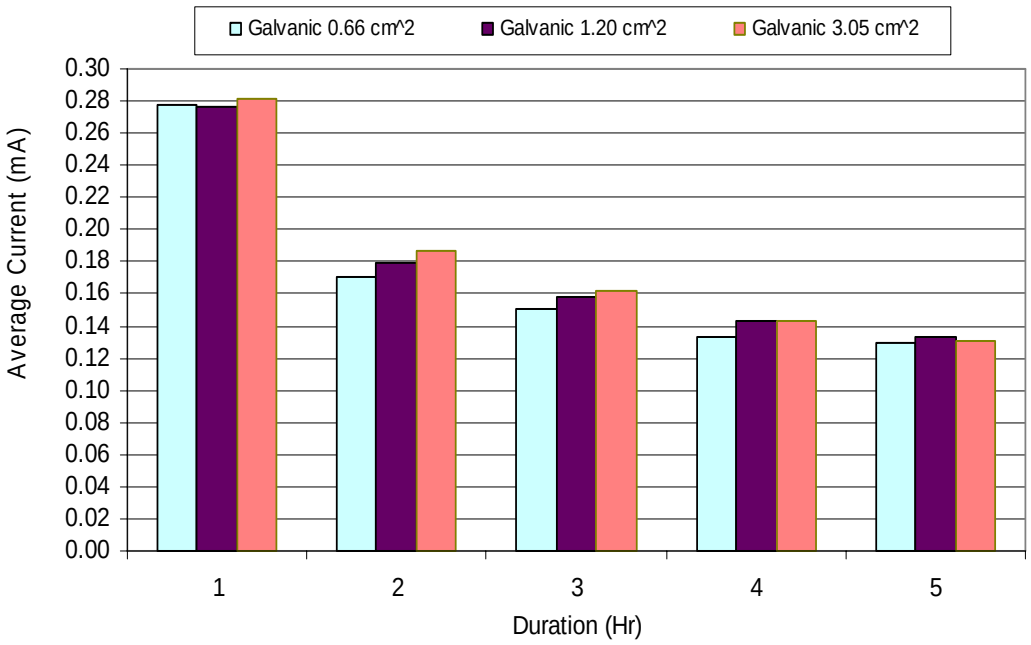


Figure 3-6 Average galvanic current over hourly intervals in carbon dioxide saturated brine solution at 30$^{o}$C and total pressure of 1 atm.

In the study by Baboian (Baboian, 1976a) on the galvanic corrosion of a copper/iron couple, it was found that the galvanic corrosion of iron was accelerated with increasing cathode to anode area ratio in the galvanic couple. The mixed potential shifted to less negative values, indicating a cathodic control event. The same trend of results was observed in this study of the magnetite/ mild steel coupling, as illustrated in Figure 3-7 and Figure 3-8 with the mixed potential shifted towards more noble potential as the cathode to anode area ratio increased. Perhaps this galvanic coupling could be under the influence of cathodic control from the magnetite.

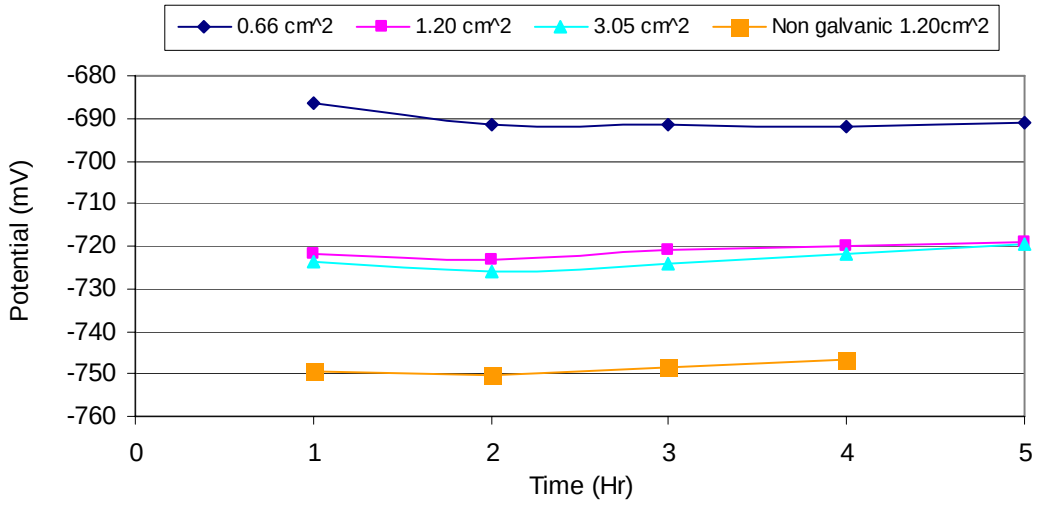


Figure 3-7 Mixed potential of magnetite/mild steel coupling with different mild steel surface area, and the uncoupled mild steel potential.

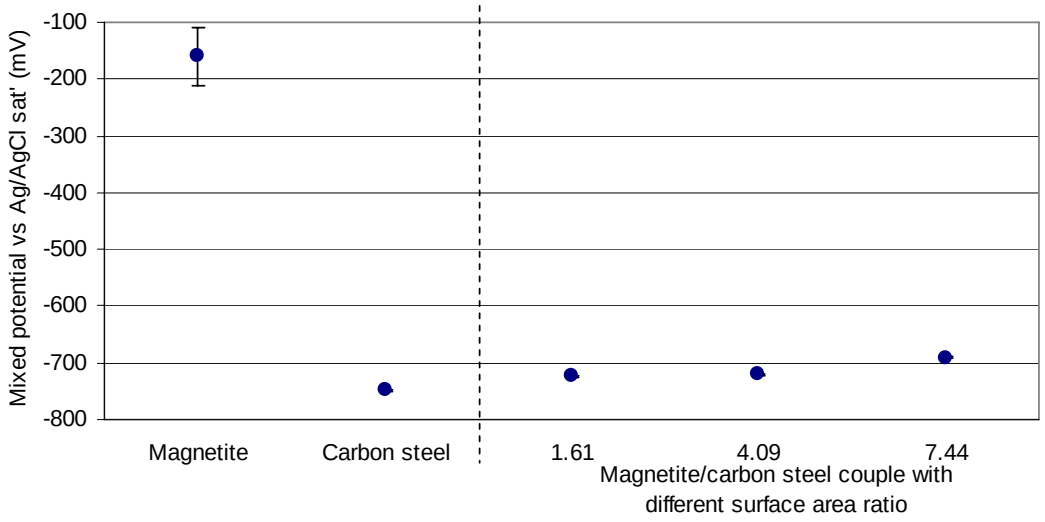


Figure 3-8 Mixed potentials of magnetite, mild steel and of magnetite/mild steel couples with different cathode to anode surface area ratio.

Since the results suggested that the galvanic corrosion is cathodically controlled by magnetite, a potentiodynamic sweep was performed on the carbon steel and magnetite independently. The results were mapped on an Evans diagram as shown in Figure 3-9. The intersection point of the cathodic curve of magnetite and the anodic curve of carbon steel is the mixed potential of the galvanic coupling. The mixed potential as determined from the Evans diagram matches closely with the measured open circuit potential of the galvanic couple of the galvanic coupling. The potential of the magnetite was highly polarised when it is coupled with carbon steel; whilst the

mixed potential of the carbon steel changed only slightly. This proves that the galvanic corrosion is indeed a cathodically control reaction.

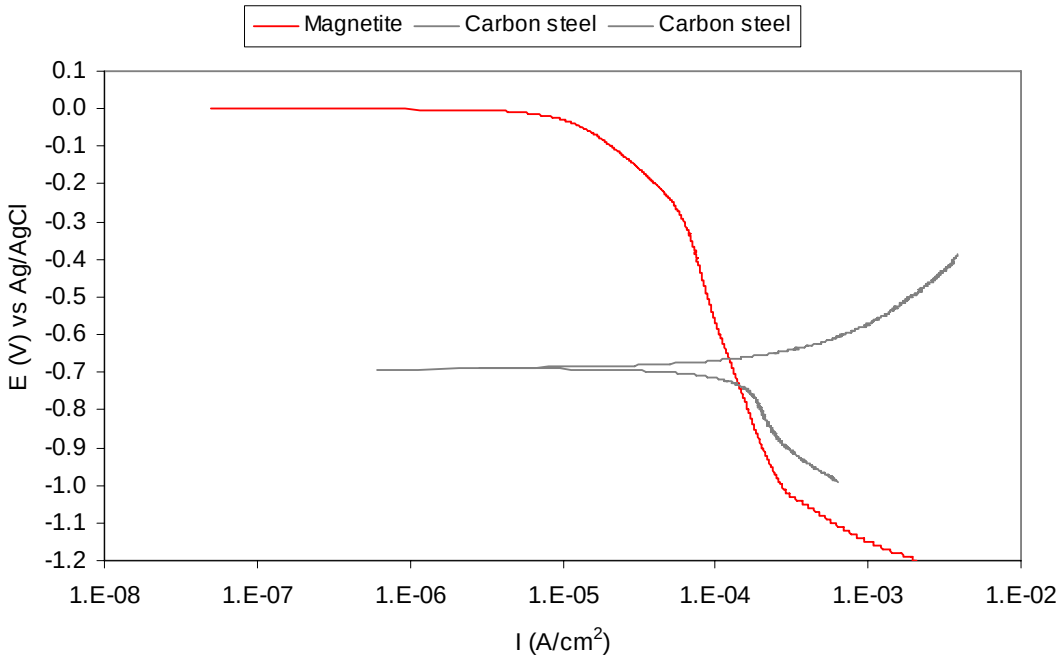


Figure 3-9 Potentiodynamic sweeps of magnetite and carbon steel in standard brine solution saturated with $CO_2$ at 30°C.

### 3.3.1.2. Effect of carbon dioxide partial pressure

Many oil and gas production fields experience carbon dioxide partial pressure drop after several years of production. The pH of the production fluid in the pipeline is very much affected by the carbon dioxide partial pressure as the $CO_2$ equilibria govern the equilibrium of the pH.

The solution pH of a standard brine solution at ambient conditions normally falls in the range of 6 to 8 as it is poorly buffered. The results of pH variation with carbon dioxide partial pressure are shown in Figure 3-10. The pH of the solution has an inverse relationship with the dissolved carbon dioxide concentration. As the brine solution is fully deoxygenated with nitrogen, the alkalinity of the solution increases and registered a pH 8.86 due to the presence of 0.1 g/L of sodium bicarbonate and the displacement of dissolved carbon dioxide in the brine solution. However, as soon

as carbon dioxide gas is introduced, the pH of the solution drops rapidly due to the formation of carbonic acid.

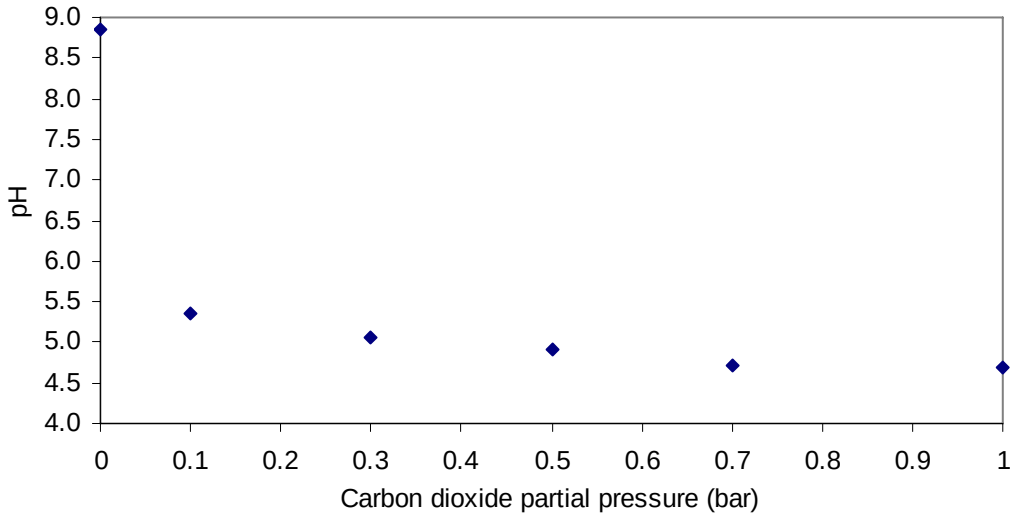


Figure 3-10 Relationship of carbon dioxide partial pressure with pH in brine solution containing 30 g/L NaCl and 0.1 g/L of sodium bicarbonate at 30$^{o}$C and total pressure of 1 atm.

Since the partial pressure affects the pH of the solution, it also affects the corrosion rate of carbon steel according to the corrosion prediction from De Waard and Milliams on the effect of pH (De Waard, Milliams, & Lotz, 1991). Therefore the effect of pH on galvanic corrosion of this magnetite - carbon steel coupling was investigated. Results in Figure 3-11 show the influence of $CO_2$ partial pressure on the self corrosion and the galvanic corrosion rates. The self corrosion rate of the mild steel increased significantly with increasing partial pressure of carbon dioxide. The increase of the overall corrosion rate was largely caused by the increasing rate of the self corrosion that became dominant at higher partial pressures. However, at lower partial pressure of $CO_2$, the galvanic corrosion rate did not reduce significantly, and so it becomes a major contributor to the overall corrosion rate.

The effect of carbon dioxide partial pressure to the mixed potential of the magnetite/mild steel couple (Emixed) could not be studied or analysed precisely as the potential variations were very small and fell within ±3mV error margin of the measured potential fluctuations.

Figure 3-11: Effect of carbon dioxide concentration on corrosion rate in brine solution at 30$^{o}$C and total pressure of 1 atm.

At 0.1 bar of $CO_2$ partial pressure, the galvanic corrosion rate was almost double of the self corrosion rate. The high solution pH seems to have limited influence on the galvanic current. The severity of carbon dioxide corrosion is known at low pH but no one would have predicted a high overall corrosion rate near neutral pH under the influence of the magnetite coupling. The relatively high galvanic corrosion rate in mildly acidic condition could be tied into previous suggestion that magnetite itself was partaking in the reduction reaction. The reductive dissolution phenomenon of magnetite has been studied previously by Fushimi et al. (Fushimi et al., 2002) and Haruyama et al. (Haruyama & Masamura, 1978) in anaerobic sulfate solution and acidic perchlorate solution. They both hypothesized that the reduction of magnetite itself might have contributed to a galvanic corrosion of the carbon steel in addition to the contribution from the reduction of water, whereby magnetite may be reduced to iron oxide with lower valency or metallic iron. Therefore, an in depth study on the reduction mechanism of magnetite was carried out and will be discussed in the next chapter.

### 3.3.2. Inhibition of galvanic corrosion

In the oil and gas industry, carbon dioxide corrosion is often controlled through the application of a corrosion inhibitor. Most corrosion inhibitors are specially formulated to prevent specific types of corrosion and ensure its compatibility in different operating conditions. Many corrosion inhibitors work efficiently in controlling the self corrosion of the carbon steel, but these inhibitors might fail when the corrosion on the carbon steel involves other types of corrosion. Besides, the galvanic corrosion caused by magnetite is fairly new to the oil and gas industry and there are no commercially available inhibitors that target this type of corrosion. Therefore, in this work, some generic inhibitors and commercially used corrosion inhibitors were selected to test their efficiency of performance against this galvanic corrosion.

#### 3.3.2.1. Inhibition from generic inhibitors

Previous results showed that the galvanic corrosion of magnetite/carbon steel couple was a cathodically controlled reaction. Therefore, an effective galvanic corrosion control can be achieved by suppressing either the cathodic or the anodic current curve.

The effectiveness of different generic corrosion inhibitors on the magnetite based galvanic corrosion of carbon steel under a carbon dioxide environment was investigated. Six inhibitors were studied: cetylpyridinium chloride (CPC), imidazoline, dodecylpyridinium chloride (DPC), thioglycolic acid (TGA), benzyldimethylhexadeclammonium chloride (C16BDMAC) and DPC/TGA mix (1:10 mass ratio). The inhibitors were applied at twice the CMC concentration. Figure 3-12 shows the self corrosion rate of carbon steel over a five hour test period with inhibitors added after two hours of blank corrosion rate measurement. The addition of DPC/TGA mix resulted in the lowest corrosion rate on the carbon steel: 0.2 mm/yr. On the contrary, the addition of DPC alone did not reduce the corrosion rate significantly and the corrosion rate measured at the end of three hours after the addition was relatively high at 1.0 mm/yr. The remaining inhibitors are found to

reduce the corrosion rate to within the range of 0.4 to 0.8 mm/yr. Overall, the self corrosion from all the six inhibitors tested was relatively high, and above the generally accepted protective range of below 0.1 mm/yr.

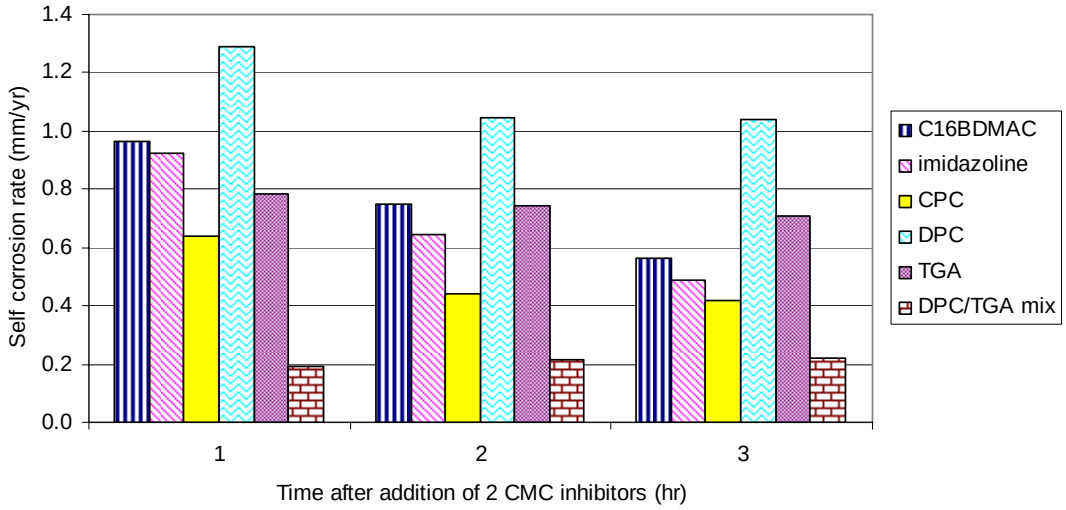


Figure 3-12 Inhibition effect on self corrosion of carbon steel in standard brine solution.

The results of the galvanic corrosion rate in Figure 3-13 show that both imidazoline and the DPC/TGA mix work more efficiently in galvanic corrosion control than the rest of the inhibitors tested. However, the galvanic corrosion rate from all the inhibitors tested was still higher than the self corrosion rate and contributed to higher overall corrosion (the summation of both the self corrosion rate and the galvanic corrosion), as depicted in Figure 3-14. Evidently, the inhibitors were more effective in controlling the self corrosion rather than the galvanic corrosion.

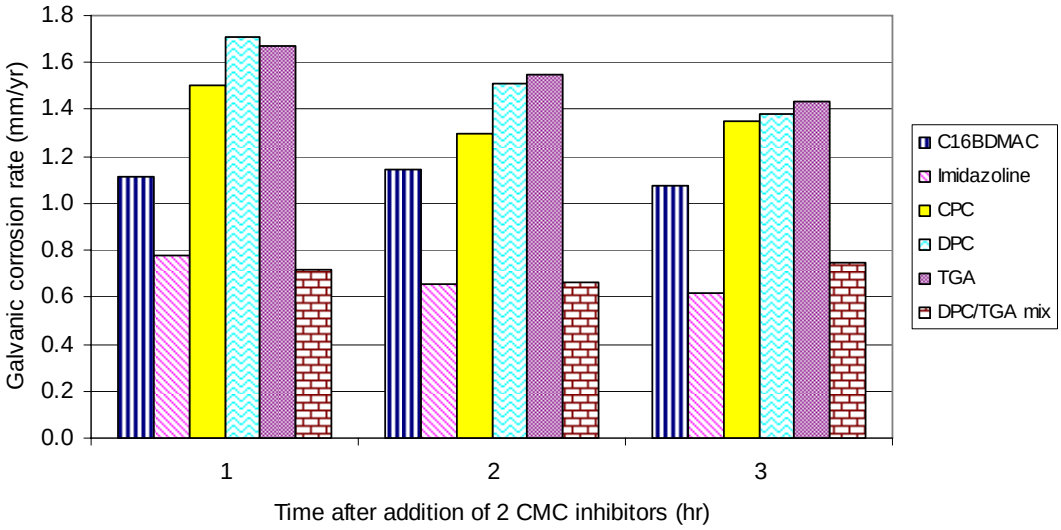


Figure 3-13 Inhibition effect on galvanic corrosion rate of carbon steel in standard brine solution.

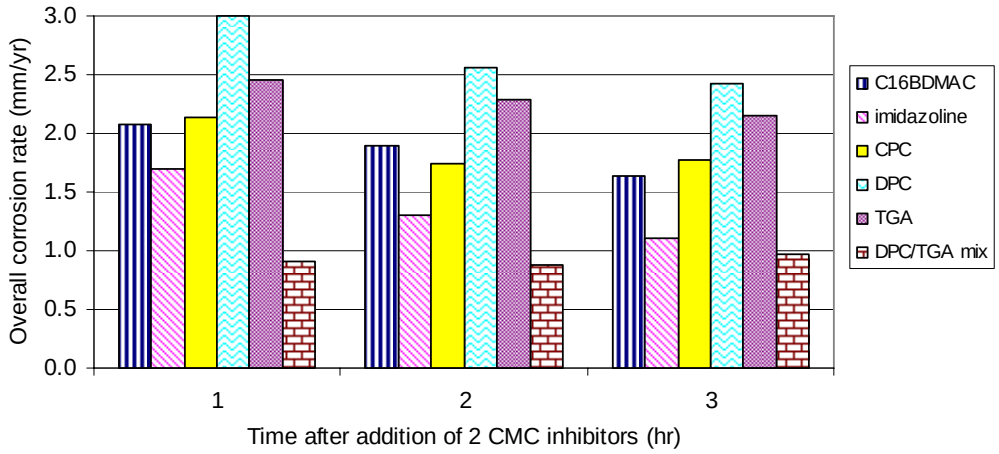


Figure 3-14 Inhibition of the overall corrosion rate of carbon steel from the galvanic coupling galvanic in standard brine solution.

A direct comparison of inhibitors can be made from Figure 3-15 which summarises the inhibition efficiencies for the inhibitors. The maximum efficiency achieved by both imidazoline and the DPC/TGA mix was only 65% and 67%, respectively, on galvanic corrosion control. This was far from achieving a confidence level of at least 90% of inhibition efficiency.

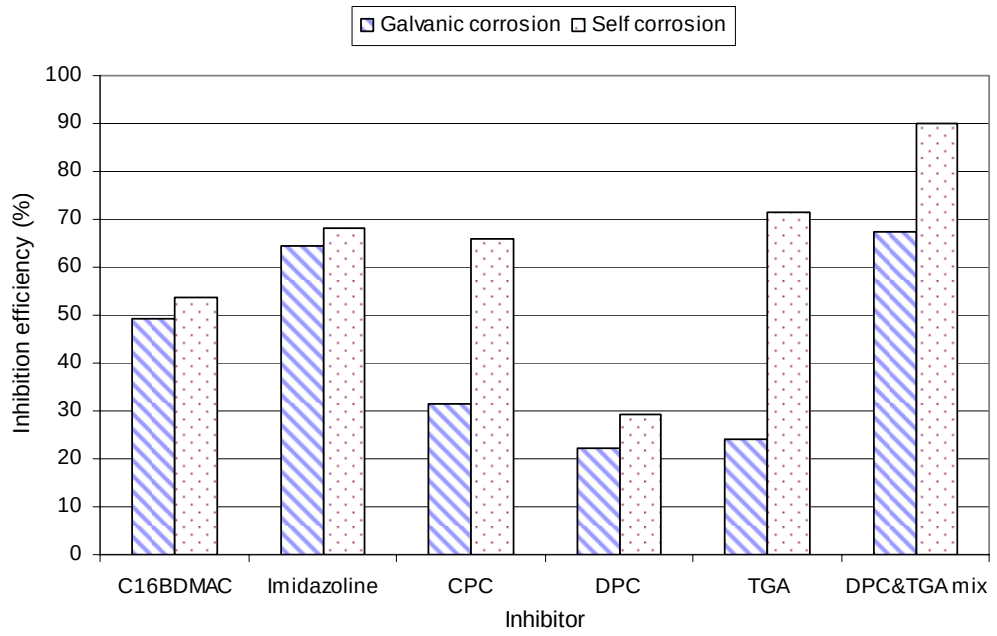


Figure 3-15 Comparison of the inhibition efficiency from different inhibitors on galvanic corrosion and self corrosion of carbon steel after 1 hour of inhibition.

The study of the mixed potential and galvanic current provided some information on the response of the inhibitors to galvanic corrosion. The galvanic current of the magnetite couple started off at a high current density and gradually reached a limiting value with time. Inhibitors were dosed in after 200 s of coupling. As shown in Figure 3-16, the response from each inhibitor varied. The galvanic current density dropped almost instantly with all the inhibitors added, except for CPC which did not have a distinctive break point and the galvanic current decreased gradually with time. DPC and TGA alone had a relatively low inhibition effect in limiting the galvanic current. However, the mixed solution of DPC and TGA inhibitors resulted in a drastic drop in the galvanic current. The inhibition effect of the mixed inhibitor solution was comparable to the results from imidazoline and C16BDMAC. Thus, the synergistic effect of this inhibitor mix could play a role in the inhibition.

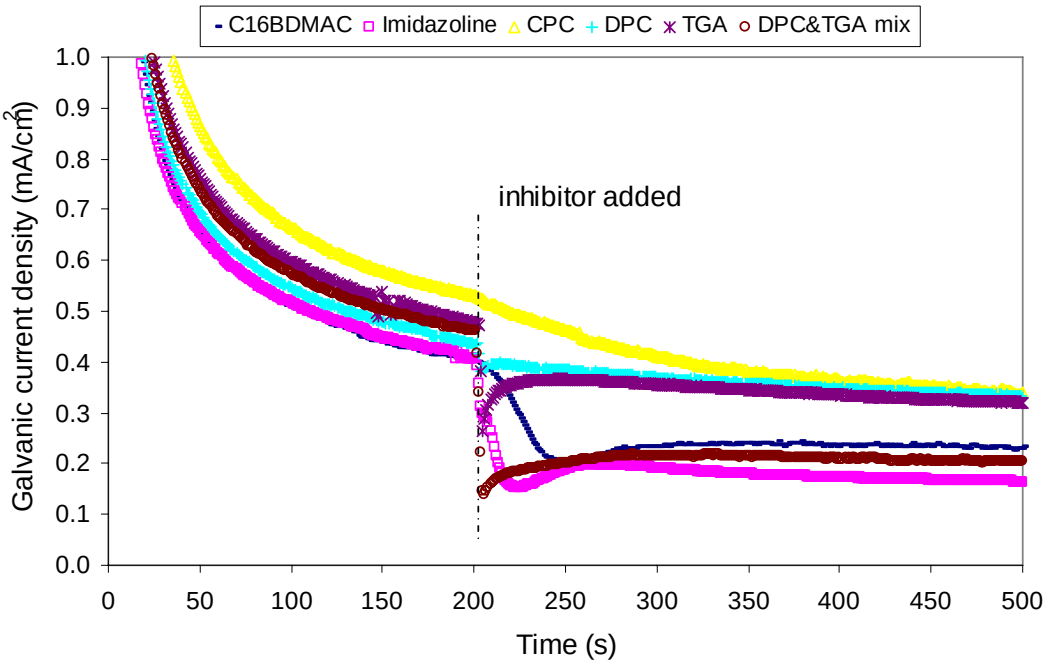


Figure 3-16 Galvanic current density response with different inhibitors added.

Earlier investigation on the galvanic coupling of magnetite and carbon steel showed that the galvanic coupling of magnetite and carbon steel was cathodically controlled by the reduction reaction. The results in Figure 3-17 show that the mixed potential changed upon addition of the inhibitors. Clearly, the stronger the shift of the mixed potential towards higher anodic potential, the better the inhibition effect on the galvanic corrosion. The increase OCP and a decrease corrosion rate trend of the inhibitors indicates that the inhibitors are anodic inhibitor. The DPC/TGA mixed solution had the largest mixed potential shift, followed by imidazoline and C16BDMAC. The mixed potential changed slightly with the addition of CPC, DPC and TGA alone and the potential was still very close to the mixed potential of carbon steel in a $CO_2$ saturated brine solution.

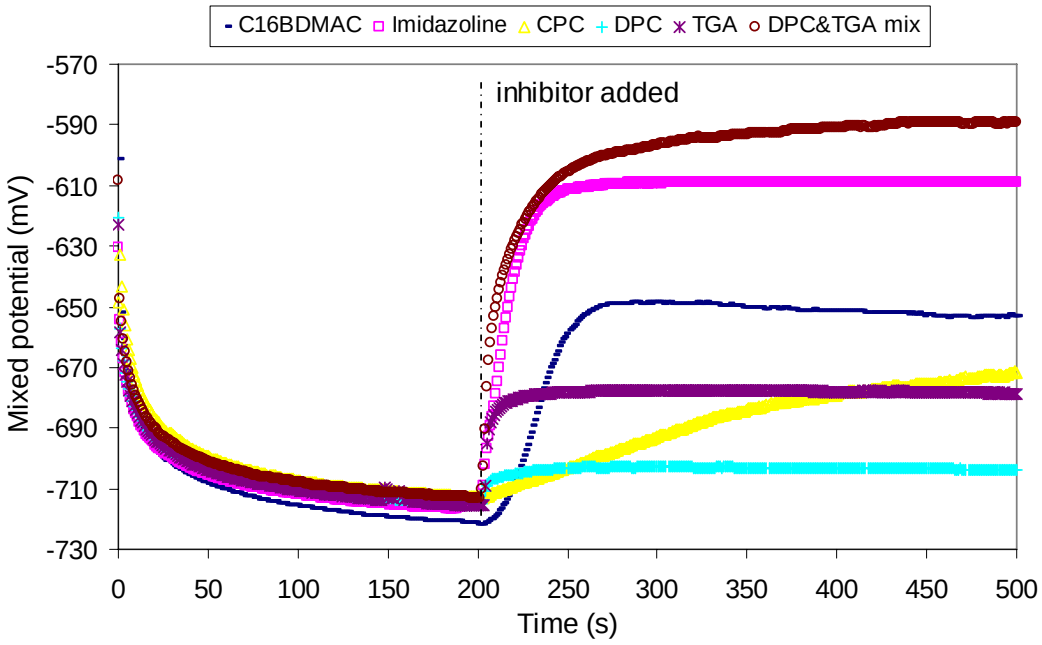


Figure 3-17: Mixed potential change with inhibitors added

Molecular simulation information published by Ramachandran and Jovanicevic (S. Ramachandran & V. Jovancicevic, 1999a) showed that imidazoline adsorbs strongly on both the anodic and cathodic sites of the electrically conductive magnetite surface as imidazoline had the strongest binding energy on the magnetite when compared with single molecules of water, amines and amides. The simulation studies suggest that the formation of a bilayer film could overcome the direct adsorption of imidazoline molecules that only covered one third of the surface $Fe^{2+}$ sites (S. Ramachandran & V. Jovancicevic, 1999a; Ramachandran, Jovancicevic, & Ward). The claims were solely based on simulation results - there was no physical testing reported. Nonetheless, the simulation results showed that imidazoline would be effective in controlling the galvanic corrosion from magnetite.

On the other hand, TGA is a very strong chelating or complexing agent which dissolves magnetite (Borghi, Morando, & Blesa, 1991). It complexes both $Fe^{2+}$ and $Fe^{3+}$ and reduces $Fe^{3+}$ by intramolecular electron transfer to much less soluble disulphides to form a protective surface oxide/carbonate/disulfide film (Baumgartner, Blesa, & Maroto, 1982; Jovanicevic, Ahn, Dougherty, & Alink, 2000). Jovanicevic, et al. (Jovanicevic et al., 2000) claimed that TGA is an anodic inhibitor based on the anodic shift of the mixed potential, but this claim was opposed by Bilkova, et al.

(Bilkova, Hackerman, & Bartos, 2004) who proposed that the corrosion potential shift was due to the change in pH. This was also supported by work from Borghi, et al. (Borghi et al., 1991) on dissolution of magnetite in TGA which showed that the rate is dependent on the pH and the concentration of TGA. The results in Figure 3-17 show a distinctive shift towards more anodic potential. However, the potential shift was not as large as the effect from imidazoline. The effect from DPC was even lower. However, the synergism between DPC and TGA enhanced the effectiveness on the galvanic corrosion control and caused the greatest anodic shift of the mixed potential. The synergistic effect of the DPC and TGA mix is not well understood and is still under investigation.

#### 3.3.2.2. Inhibition from commercial inhibitors

Commercially available corrosion inhibitors are formulated for specific industry needs and applications. Corrosion inhibitors are designed to block either active cathodic or anodic reaction sites of the corrosion reaction or incorporate into the corrosion product to prevent further access of the corrosive fluid. Therefore, a selection of corrosion inhibitors, which are commonly used in oil and gas fields for carbon steel in carbon dioxide environments, were tested for the effectiveness in controlling the galvanic corrosion from magnetite. Generally, all inhibitors tested responded well in reducing self corrosion of the carbon steel. The results of the self corrosion rate reduction are summarized in Table 3-2.

Table 3-2 Comparison of self corrosion rate reduction from different corrosion inhibitors in brine solution at 30$^{o}$C and total pressure of 1 atm.

| | Time (Hr) | | | | |
|---|---|---|---|---|---|
| | 1 | 2 | 3 | 4 | 5 |
| | Inhibitor concentration (ppm) | | | | |
| | 0 | 0 | 10 | 20 | 50 |
| Inhibitor ID | Corrosion rate (mm/yr) | | | | |
| Inhibitor 1 | 2.44 | 2.49 | 0.30 | 0.15 | 0.13 |
| Inhibitor 2 | 2.44 | 2.46 | 0.22 | 0.15 | 0.13 |
| Inhibitor 3 | 2.39 | 2.38 | 0.34 | 0.25 | 0.22 |
| Inhibitor 4 | 2.44 | 2.49 | 0.49 | 0.32 | 0.24 |
| Inhibitor 5 | 2.84 | 2.86 | 0.87 | 0.49 | 0.35 |
| Inhibitor 6 | 2.49 | 2.62 | 1.18 | 0.57 | 0.46 |
| Inhibitor 7 | 2.32 | 2.41 | 0.30 | 0.25 | 0.19 |
| Inhibitor 8 | 2.56 | 2.65 | 0.49 | 0.36 | 0.31 |
| Inhibitor 9 | 2.26 | 2.34 | 0.35 | 0.29 | 0.23 |
| Inhibitor 10 | 2.71 | 3.14 | 0.46 | 0.25 | 0.20 |

On the contrary, the results for galvanic corrosion inhibition were not promising, as seen in the tabulated results in Table 3-3. The overall galvanic corrosion inhibition efficiency was relatively low with a maximum of 74% achieved with inhibitor 3 as shown in Figure 3-18. This suggests that the corrosion inhibitors tested failed to inhibit the electrically conductive surface of magnetite, allowing electrons to flow freely from the anodic mild steel surface to the cathodic magnetite surface.

Overall, the generic inhibitors as well as the commercial inhibitors tested did not control the galvanic corrosion satisfactorily. Hence, it is important to raise global awareness on the severity of the galvanic corrosion caused by the magnetite and carbon steel coupling amongst the oil and gas industry and inhibitor suppliers, and the dire need to formulate an inhibitor that can control this galvanic corrosion.

Table 3-3 Comparison of galvanic corrosion rate reduction from different corrosion inhibitors in brine solution at 30°C and total pressure of 1 atm.

| | Time (Hr) | | | | |
|---|---|---|---|---|---|
| | 1 | 2 | 3 | 4 | 5 |
| | Inhibitor concentration (ppm) | | | | |
| | 0 | 0 | 10 | 20 | 50 |
| Inhibitor ID | Corrosion rate (mm/yr) | | | | |
| Inhibitor 1 | 2.76 | 1.75 | 1.02 | 0.85 | 0.74 |
| Inhibitor 2 | 2.82 | 1.79 | 0.68 | 0.48 | 0.40 |
| Inhibitor 3 | 2.58 | 1.64 | 0.56 | 0.42 | 0.36 |
| Inhibitor 4 | 2.89 | 1.79 | 0.84 | 0.80 | 0.69 |
| Inhibitor 5 | 3.41 | 2.12 | 1.24 | 1.10 | 0.91 |
| Inhibitor 6 | 3.12 | 1.90 | 1.28 | 0.85 | 0.72 |
| Inhibitor 7 | 2.94 | 1.82 | 0.74 | 0.61 | 0.50 |
| Inhibitor 8 | 3.05 | 1.82 | 0.61 | 0.61 | 0.52 |
| Inhibitor 9 | 3.15 | 1.87 | 1.08 | 0.92 | 0.80 |
| Inhibitor 10 | 2.64 | 2.07 | 1.34 | 1.15 | 0.97 |

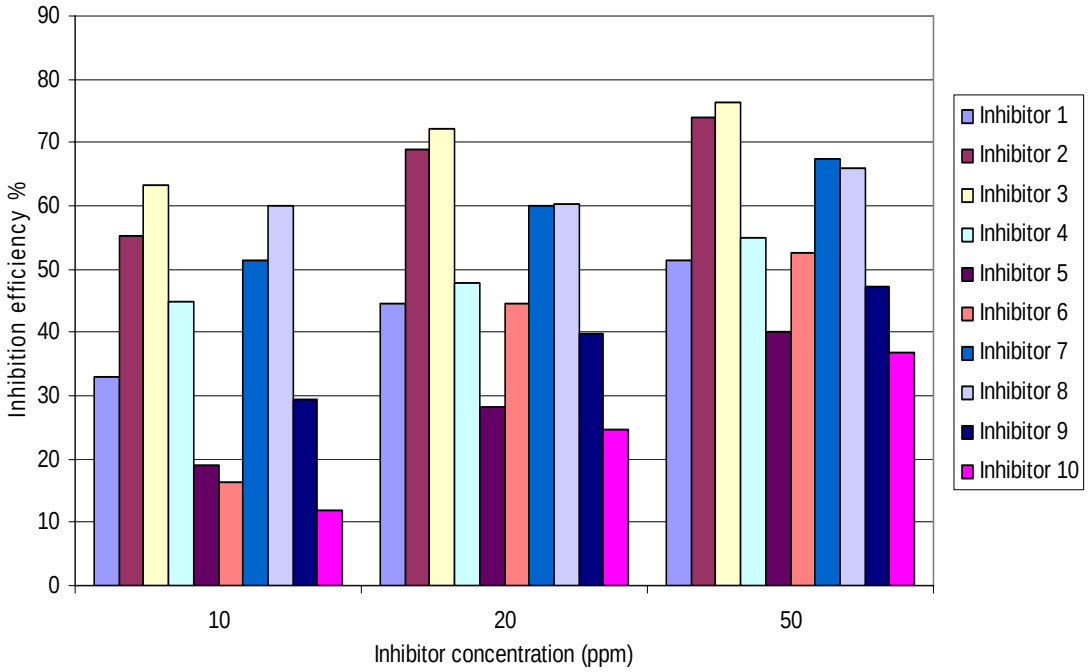


Figure 3-18 Comparison of inhibition efficiency of different corrosion inhibitors for galvanic corrosion control in brine solution at 30°C and total pressure of 1 atm.

## 3.4. CONCLUSIONS

The presence of the magnetite scale causes galvanic corrosion of the carbon steel under carbon dioxide conditions, even in mildly acidic conditions. Increasing the cathode to anode surface area ratio increases the galvanic corrosion rate and thus increases the overall corrosion rate of the mild steel. Corrosion of the magnetite/carbon steel galvanic couple was a cathodically controlled process limited by the cathodic reaction. The carbon dioxide partial pressure, which influences the solution pH, affects not only the self corrosion rate but also the galvanic corrosion rate. At low pH, the self corrosion rate increases due to the severity of carbonic acid attack; at pH close to neutral, the galvanic component from magnetite results in a relatively high overall rate of corrosion. Since the formation of magnetite is favoured at high pH, pipelines operating at mildly acidic conditions are at risk of a high corrosion rate due to the galvanic coupling effect from the magnetite scale to the exposed carbon steel.

Inhibitors that work satisfactorily in self corrosion control failed to inhibit the galvanic corrosion caused by magnetite. The inhibition results for imidazoline and for a mixed solution of DPC and TGA showed better galvanic control than other generic inhibitors tested. The synergistic effect of the inhibitors may offer a route towards resolving the problems with the galvanic corrosion from the magnetite coupling.

# CHAPTER 4 REDUCTION OF MAGNETITE

## 4.1. INTRODUCTION

Magnetite is the main constituent of mill scale and the primary corrosion product scale on carbon steel in high temperature and high pressure applications such as heat exchangers, boilers, steam generators and reactors. The build-up of the magnetite deposits is found to be problematic because it can potentially clog up the pumping system, reduce the heat transfer efficiency of the heat exchangers, and cause localised corrosion (Al-Mayouf, 2006; Al-Mayouf et al., 2007). Therefore chemical cleaning processes which dissolve the magnetite deposit with acid have been adopted in the boiler industry to enhance the service life of the equipment. However, oil and gas pipelines are constantly under carbonic acid attack which can dissolve the porous magnetite scale, and also penetrate through the pores, cracks and other faults in the magnetite layer to attack the exposed active metal (Al-Mayouf et al., 2007). The coupling of magnetite and mild steel under carbon dioxide conditions has caused galvanic corrosion of the carbon steel as proven in the previous chapter.

Recently, there have been several studies on the coupling of magnetite with mild steel and the results suggested that the accelerated corrosion of the carbon steel is a consequence of an additional cathodic reaction from the reductive dissolution of magnetite. The validity of this hypothesis was justified by Fushimi, Yamamuro and Seo (Fushimi et al., 2002) using a platinum microdisk probe electrode for the detection of hydrogen generated from a magnetite electrode during galvanic coupling with a carbon steel electrode in anaerobic sulphate solution. The results showed a large discrepancy of the probe current from the hydrogen generation on magnetite alone to the coupling current of the galvanic coupling, with a deduced current efficiency of about 50%. The authors also compared the probe current of the coupling, uncoupled carbon steel and uncoupled magnetite at different pH. The results suggested that magnetite itself took place in the reduction reaction in parallel with hydrogen generation. On the other hand, Haruyama and Masamura (Haruyama & Masamura, 1978) also proved the reductive dissolution of magnetite in fully deaerated acidic perchlorate solution by means of the potential sweep method and

impedance measurement and compared this with colorimetric analysis of the ferrous ion. This showed that cathodic peak of magnetite at around -900 mV was due to the reduction of magnetite to ferrous ion in Reaction 4-1. The reduction potential at -1200 mV, as hypothesized by the author, was assigned to the reduction of magnetite to metallic iron according to Reaction 4-2. Furthermore, the authors also postulated that a surface layer of ferrous hydroxide may form at the potential between -100 mV to -900 mV by the adsorption of protons.

$$Fe_3O_{4(s)} + 8H^+_{(aq)} + 2e^- \rightarrow 3Fe^{2+}_{(aq)} + 4H_2O_{(l)} \qquad \text{Reaction 4-1}$$

$$Fe_3O_{4(s)} + 8H^+_{(aq)} + 8e^- \rightarrow 3Fe_{(s)} + 4H_2O_{(l)} \qquad \text{Reaction 4-2}$$

The reaction pathway of the reductive dissolution of magnetite was deduced from the backward reaction of its formation via the hydrolysis reaction of ferrous ions (Allen, Hampson, & Bignold, 1980). Allen, Hampton and Bignold (Allen et al., 1980) and Sweeton and Baes (Sweeton & Baes, 1970) proposed that the rate of dissolution of magnetite is controlled by the pH. In order for $Fe^{2+}$ to dissolve in solution, the $Fe^{3+}$ has to be converted to $Fe^{2+}$ according to Reaction 4-3 to maintain its electrical neutrality in the crystal. The rate of the $Fe^{3+}$ reduction is dependent of the rate at which $Fe^{2+}$ is dissolved from the crystal surface. Subsequently, the $Fe^{2+}$ leaves the iron lattice in acid dissolution via the intermediate $FeOH^+$ according to Reaction 4-4 and Reaction 4-5.

$$Fe^{3+} + e \rightarrow Fe^{2+} \qquad \text{Reaction 4-3}$$

$$Fe^{2+}_{lattice} + OH^- \rightleftharpoons FeOH^+_{(aq)} \qquad \text{Reaction 4-4}$$

$$(FeOH)^+_{ads} + H^+ \rightleftharpoons Fe^{2+}_{(aq)} + H_2O_{(l)} \qquad \text{Reaction 4-5}$$

The galvanic corrosion rate results from the previous chapter indicated the possibility of magnetite itself partaking in self reduction which contributed to the galvanic corrosion. In order to verify the previous hypothesis, a series of different electrochemical and surface analysis techniques were employed to investigate the reductive dissolution of magnetite. The specific techniques include cyclic voltammetry (CV), potentiodynamic electrochemical impedance spectroscopy (PDEIS), in-situ Raman spectroscopy and ex-situ surface and compositional analysis from FESEM.

Cyclic voltammetry (CV) has been widely used in electrochemistry to study the adsorption and desorption of species based on the cathodic and anodic peaks from the redox reactions. However, the application of this technique has surpassed the conventional electrochemistry studies and advanced in the semiconductor and battery research (McHardy & Ludwig, 2002). Interpretation of the CV data is not always straightforward owing to the complexity of the solid-electrolyte interaction and electrochemical reaction which might involve adsorption, electrodeposition, surface redox reactions, electrochemical double layer capacitance and space charge capacitance (Pandey, Sahu, & Chandra, 1996). In fact, in depth understanding of CV can provide significant useful information.

Magnetite is an extrinsic semiconductor. It is an n-type semiconductor at its natural state. Its interchangeable electron state of $Fe^{2+}$ and $Fe^{3+}$ in the octahedral sites allows the migration of electrons to conduct current. The occurrence of the electronic transition of magnetite when it is being polarized electrochemically can be explained by the band theory. Magnetite, being an electrode, has a redox potential when it is in contact with an electrolyte solution. This redox potential is determined by the Fermi level. The redox potential of the electrolyte normally has different energy than the Fermi level of a semiconductor. Therefore, the charge between the two phases will shift to achieve equilibrium. The excess charge on a metallic electrode lies at the surface; whilst the excess charge on a semiconductor extends into its electrode surface for a significant distance of 100-10,000 Å, forming a region with depleted mobile carriers, known as the space charge region. Normally, a metallic electrode does not have a space charge region, therefore, an applied potential will cause a shift in the Fermi level; whereas applying a potential on a semiconductor will cause either an upward or a downward bending of the band edges in the interior of the semiconductor, away from the depletion region. Hence, the concept of the band bending of the band edges under depletion condition was adopted by Mott-Schottky using the potentiodynamic electrochemical impedance spectroscopy (PDEIS) technique known as Mott-Schottky analysis to determine the type of semiconductor by measuring the apparent space charge capacitance as a function of potential (Bott, 1988).

## 4.2. EXPERIMENTAL

### 4.2.1. Electrochemical setup

A magnetite rock sample from Arkansas Magnet Cove was cored into a cylindrical rod with a diameter of 4.6 mm. The rod sample was then adhered onto the center of a threaded stainless steel stub with silver epoxy to ensure electrical connectivity. The magnetite rod assembly was then filled with epoxy in a mould and let it cured overnight. Once the epoxy was cured, the top epoxy layer was removed by grinding the electrode on a 600 grit grinding paper, leaving an exposed steel surface area of 0.166 $cm^2$.

Electrochemical tests on the magnetite disc electrode were run on a typical rotating electrode test setup. A glass cell was filled with a brine solution containing 30 g/L NaCl in milliQ water. The brine solution was deaerated with $CO_2$ gas under atmospheric pressure at 30$^oC$. The cell setup consists of a platinum mesh counter electrode, a silver/silver chloride reference electrode, a magnetite working electrode and a thermocouple to feedback control of the solution temperature. The standard sample preparation as described in the previous chapter was applied on the magnetite electrode. All electrochemical measurements were performed using a Gamry Ref 600 potentiostat.

The semiconductor behaviour of magnetite was investigated using the Mott-Schottky method on a Gamry Ref 600 potentiostat which runs on Gamry Framework software version 5.60. The Mott-Schottky program was selected and the potential was scanned from 0.3 V to –1.0 V versus Ag/AgCl at frequency of 100 Hz, AC potential of 5 $mV_{rms}$ and voltage step of 0.1 V. The capacitance was calculated from the imaginary part of the impedance, assuming a series circuit of the capacitance in the system (refer to Figure 2-35 in Chapter 2) since the circuit with capacitance gave better fit. The tests were done under a full sparge of carbon dioxide (pH 4.87) or nitrogen (pH 8.87) in a standard brine solution containing 30 g/L of NaCl and 0.1 g/L of $NaHCO_3$. The solution was deaerated for an hour before the electrode was inserted to begin the test measurement. The results were analysed using the Gamry Echem Analyst software version 5.50.

Cyclic voltammetry measurements were taken under conditions where the magnetite electrode was stationary or rotated. A Pine rotator was used to rotate the electrode at a rotational rate of 500 rpm. The CV was applied at a scan rate of 2 mV/s, sweeping cathodically from 0 V (vs Ag/AgCl) to -0.8 V (vs Ag/AgCl). The sweep was reversed anodically to 0 V (vs Ag/AgCl). The first set of tests was run under full deaeration with carbon dioxide at the pH of 3.87 (unbuffered) and 4.87 (buffered with 0.1 g/L $NaHCO_3$). The second set of the test was carried out under full sparge with nitrogen to verify if the reduction reaction was under the influence of pH and not from carbonic acid. Solutions of the same pH (3.87 and 4.87) were prepared by carefully adding a small amount of 0.1 M of HCl using a micropipette into a fully deoxygenated brine solution (starting pH 7.89) to the desired pH. The third set of tests was to compare the pH effect under the influence of carbonate and bicarbonate species in the solution. A standard brine solution containing 30 g/L of NaCl buffered with 0.1 g/L of $NaHCO_3$ was used. The pH of the solution was adjusted by controlling the partial pressure of $CO_2$ by mixing with an inert $N_2$ gas from an Allborg gas flow meter. Cyclic voltammetry measurements were obtained under the conditions of full $CO_2$ (pH 4.87), 50:50 $CO_2$ and $N_2$ mix (pH 5.08) and full nitrogen (pH 8.51).

### 4.2.2. In-situ Raman setup

The reductive transformation of magnetite was studied in-situ under an UHTS300 Raman spectroscopy system. The experimental setup comprised of 3 different systems: the Raman and electrochemical system, the reservoir system and the pumping system, as shown in Figure 4-1. The whole experimental setup with the fluid reservoir filled with 200 mL of standard brine solution, maintained at $30^oC$, was deaerated with high purity carbon dioxide gas for 2 hours. The dissolved oxygen level was measured using an Orbisphere oxygen meter at the gas outlet of a closed system through the low oxygen permeability, high purity Tygon 2275 tubing after passing through the reservoir system, pumping system and lastly the Raman system. Once the dissolved oxygen level dropped to below 1.5 ppb, a magnetite electrode with an exposed area of 0.1267 $cm^2$ which had been prepared according to the usual

sample preparation procedure was inserted into the Raman electrochemical cell (Simard, Odziemkowski, Irish, Brossard, & Ménard, 2001). Then, the same Tygon 2275 tubing was lowered from the gas phase to the liquid phase in the reservoir. The other end of the Tygon tubing connected to the Raman electrochemical cell outlet was inserted into the glass cell to complete a recirculation loop. A stopper in the glass cell was replaced instantly with a tubing insert for gas outflow. The tubing outlet was immersed into a beaker of water to prevent ingress of oxygen back into the system. The pump was then started to recirculate the solution. The bubbles in the Raman cell were removed by tilting the Raman cell slightly. Once all the bubbles were removed, the electrochemical Raman cell was mounted on the control stage of the Raman microscope.

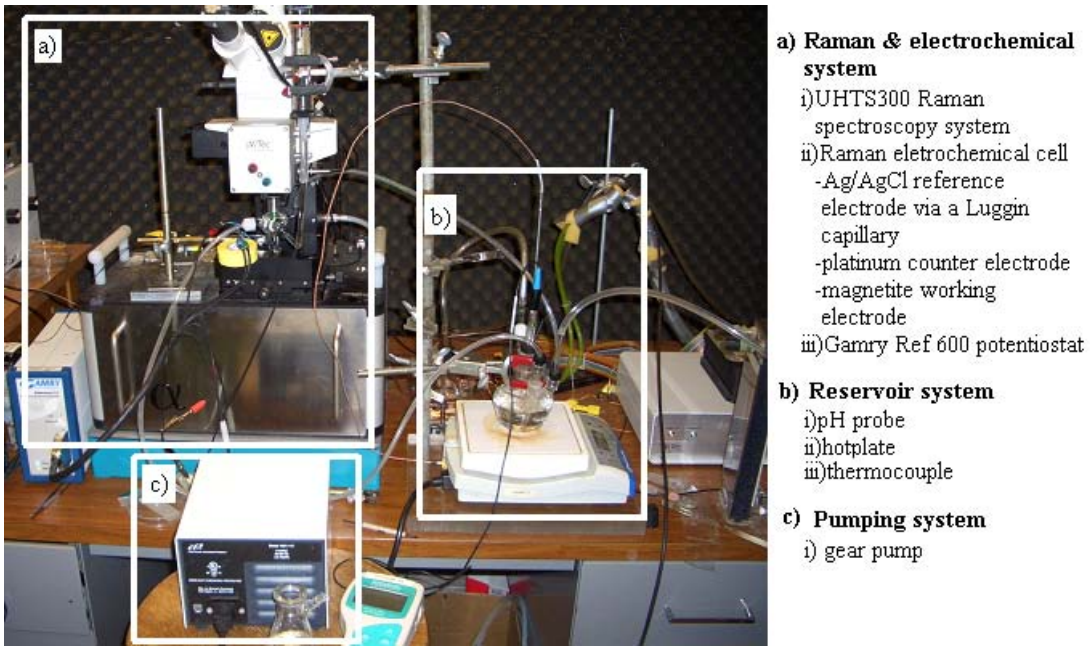


Figure 4-1 In-situ Raman test setup for magnetite reduction.

The electrochemical setup is illustrated in Figure 4-2. A potentiostatic polarisation was applied on the magnetite at -0.65 V (vs Ag/AgCl) for 4 hours using the Gamry Ref 600 potentiostat. Raman spectra of the magnetite were obtained every hour on a CRM 200 Raman spectrometer which was controlled from the WiTec ScanCtrl Spectroscopy Plus software for four hours to detect chemical changes on the magnetite during cathodic polarisation. The spectrometer was operated using 1800 g/mm gratings. Excitation was provided by a Nd:YAG laser with the

wavelength of 532 nm through a Plan 25x Nikon objective lens mounted on the WiTec Raman/near-field scanning optical microscope.

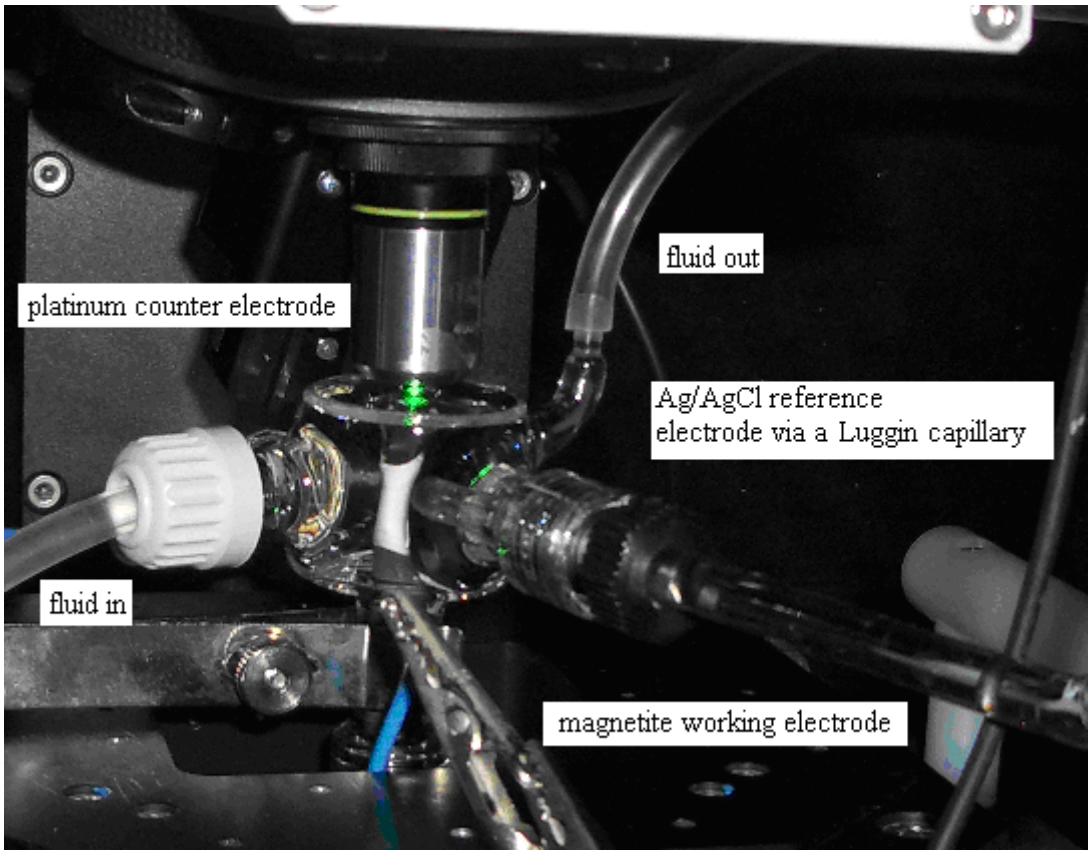


Figure 4-2 Electrochemical Raman cell setup.

## 4.3. RESULTS AND DISCUSSION

### 4.3.1. Cyclic voltammetry study of the reductive-oxidative behaviour of magnetite under carbon dioxide

The galvanic corrosion results presented in previous chapter suggest that magnetite could be partaking in self reduction, thereby contributing to the galvanic current. Therefore, the CV technique was adopted to study the effect of carbonic acid, and simply the influence of pH on the reductive-oxidative behaviour of magnetite.

#### 4.3.1.1. Effect of carbonic acid

The reductive dissolution of magnetite under carbon dioxide environments at different solution pH was investigated. Since a pipeline is constantly under dynamic flow, the CV of magnetite was obtained under rotation at a rate of 500 rpm. The CV results are presented in Figure 4-3. The trend of the CV changed with solution pH and was different from an idealised CV. The CV results of magnetite in solutions of pH above 4.83 show resemblance to the response from a semiconductor, similar to the trend described by McHardy and Luwig (McHardy & Ludwig, 2002) and Wu et al. (Wu et al., 2001). Capacitive behaviour is observed at the start of the forward scan at around 0 V (vs Ag/AgCl) in which the downward curvature of the plot indicates the charging effect of a capacitor. At pH close to 7, magnetite seems to be charging negatively towards cathodic potential with a slight hump at around -0.5 V and a reversal oxidative hump at around -0.3 V. However, the trend of the CV changed significantly when the pH of the solution dropped below pH 5. The CV for pH 3.87 has a distinct reductive humps that peak at -0.25 V on forward scan and at -0.45 V on reverse scan. Overall, the reduction current density of magnetite increased with a decrease in solution pH.

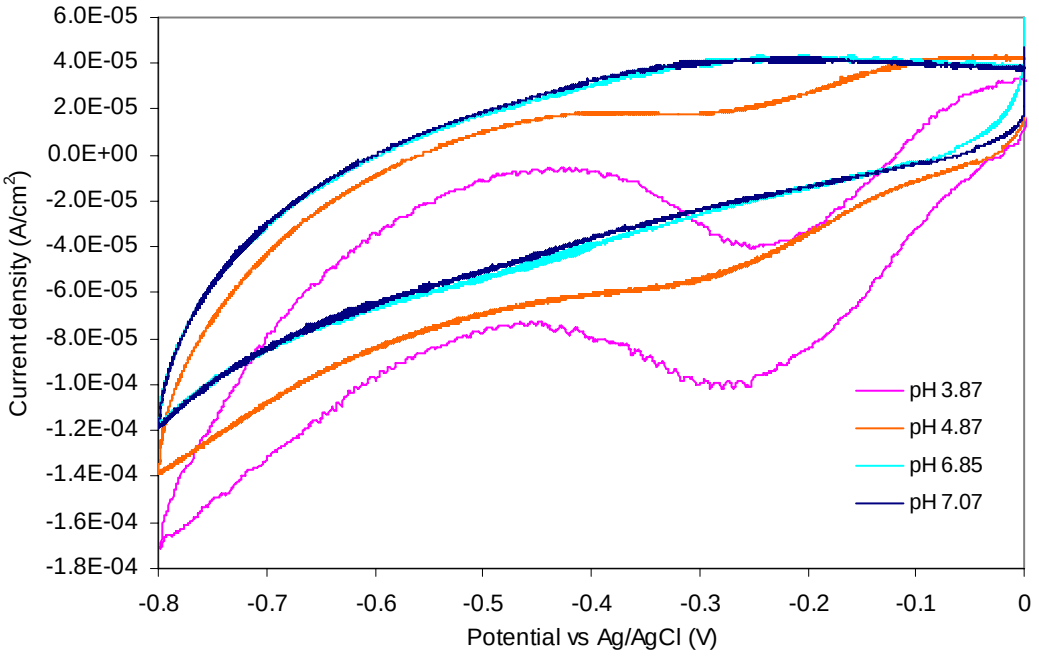


Figure 4-3: Cyclic voltammograms of magnetite in 30 g/L NaCl with the addition of $NaHCO_3$ for pH adjustment, deaerated with $CO_2$ and measured under 500 rpm rotational speed at scan rate of 2 mV/s.

The reductive behaviour of magnetite in acidic perchlorate solution was studied and discussed by Haruyama and Masamura (Haruyama & Masamura, 1978). The authors found that the first reductive peak in the region between -0.1 V to -0.3 V strongly depended on the solution pH and the dissolution rate of magnetite. At potential more negative than -0.65 V shows a limiting current behaviour controlled by a diffusion process and it is postulated that a layer of ferrous hydroxide may form in this potential range due to the adsorption of protons on the surface. In fact, the CV results are in strong agreement with authors' results which proved that magnetite undergoes reductive dissolution. The broad reduction peak at -0.25 V was seen at low pH because the reductive dissolution reaction of magnetite only occurred in low pH solution. Whereas, there seems to be another broad reduction hump at higher pH around -0.5 V. The reverse oxidation sweep did not show a clear peak but there was a broad oxidation hump between -0.5 V to 0 V. The broad reduction peak as postulated by Haruyama was the reduction and adsorption process to form a ferrous hydroxide layer. The reverse oxidation sweep could simply be the oxidation of the reduced species to iron oxide.

Since the CV of magnetite in lower pH solution looked very peculiar, the CV was repeated without rotating the electrode. A comparison of the CVs between stagnant and rotation conditions at pH 4.83 and 3.87 is shown in Figure 4-4. The CV results obtained under rotation showed a higher reductive current density as compared to the results under stagnant conditions. The trend of the CV at pH 4.83 with and without rotation was the same except for a difference in the magnitude of the current density, which seems to have shifted -10 $\mu A/cm^2$ on rotation. The reductive current density of the rotating magnetite was higher but the reverse oxidation current density was lower than the stationary magnetite. The CV trend was even more peculiar at pH 3.87. The current was still negative on the reverse sweep and a sudden increase in negative current was registered as the potential swept past -0.4 V. After sweeping past -0.25 V, the current rose anodically.

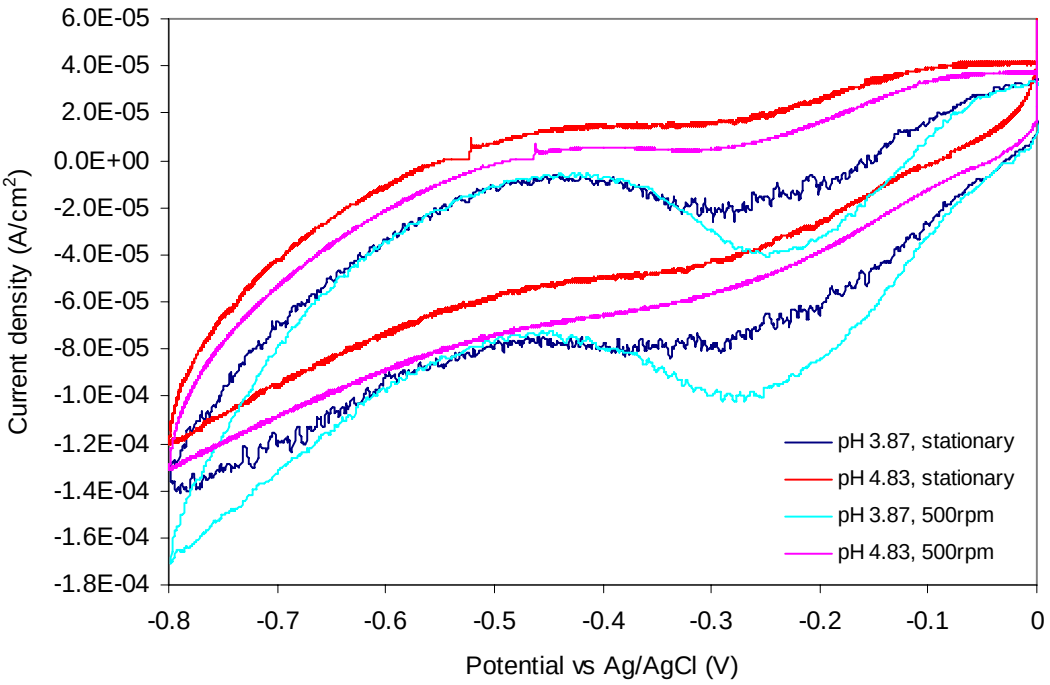


Figure 4-4: Cyclic voltammograms of magnetite in 30 g/L NaCl at low pH, deaerated with $CO_2$ at scan rate of 2 mV/s.

The reductive dissolution rate of magnetite at potentials around -0.25 V was enhanced by increasing the concentration of the acid. Besides, rotation of the electrode also helped in facilitating the diffusion of $Fe^{2+}$, which was produced by reduction of $Fe^{3+}$, away from the Helmholtz layer.

On the reverse sweep, the oxidation current of magnetite in solution pH 4.83 without rotation was higher than with rotation. Since the oxidation reaction depends on the availability of the surface ions responsible for an anodic reaction, rotating the electrode actually removes the surface ions and results in lower conversion rate. On the other hand, the oxidative current densities at pH 3.87 at the potential of -0.5 V were the same on CVs with or without rotation. However, a sudden drop of current at the potential around -0.3 V was observed. The sudden drop of current density could be an event of depassivation of an amorphous species which remained on the surface from the reduction reaction, which could not be sustained under highly acidic conditions.

#### 4.3.1.2. Effect of acid

The CV results of magnetite under different pH in acidic carbon dioxide solutions showed that magnetite underwent reductive dissolution. This reductive dissolution reaction was further investigated in the absence of carbon dioxide to compare if there were any difference in the reactions. The CV results for magnetite under rotation in the absence of $CO_2$, as shown in Figure 4-5, looked similar to the CV trend under carbon dioxide except that the current densities were lower. At low pH, the reductive peak was slightly shallower than the CV under $CO_2$ despite being at the same pH. Furthermore, no significant reductive-oxidative peak was observed except when the solution pH was below 4. The broad hump seen under $CO_2$ at pH 3.87 was also observed in the $N_2$ deaerated test at the same pH. The collective results showed that the reduction of magnetite was influenced by pH. The presence of carbon dioxide resulted in higher reaction rate than an acidic solution of the same pH which did not contain carbon dioxide.

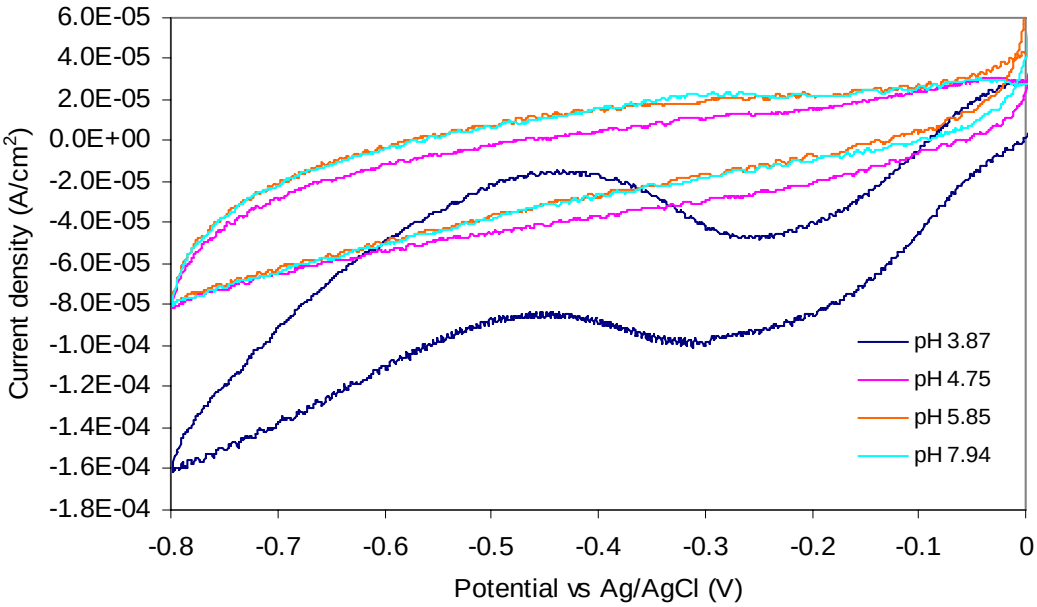


Figure 4-5: Cyclic voltammograms of magnetite in 30 g/L NaCl with the addition of HCl for pH adjustment, deaerated with $N_2$ and measured under 500 rpm rotational speed at scan rate of 2 mV/s.

The tests were again compared for the differences in the current density on the CV for the electrode under rotation and non rotation. The results are presented in Figure 4-6. Overall, the cathodic current densities of magnetite in acid solutions not containing carbon dioxide were of lower than the CV obtained in acidic carbon dioxide solution. The broad hump at around -0.25 V was not noticeable at pH 4.87 and there was barely any difference in the current density for both stationary and rotation. However, the difference was more apparent in pH 3.87. The broad humps appeared in the CV of magnetite under rotation but were not obvious on the stationary electrode. This again showed that the reduction rate of magnetite was higher in more highly acidic solutions.

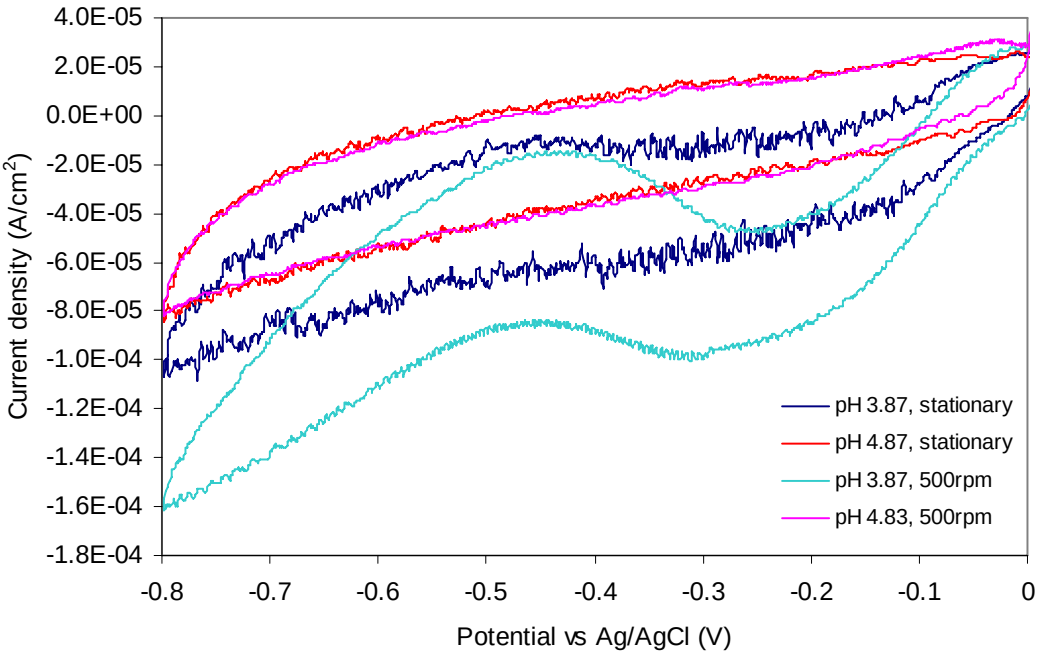


Figure 4-6: Cyclic voltammograms of magnetite in 30 g/L NaCl at low pH, deaerated with $N_2$ at scan rate of 2 mV/s.

#### 4.3.1.3. Effect of bicarbonate species

Since acidic carbon dioxide solutions showed greater magnetite reduction rates than other solutions of the same pH, a new set of tests was carried out to compare the effect of pH with the presence of bicarbonate species on the reductive dissolution reaction of magnetite. The CV results for magnetite in brine solutions buffered with 0.1 g/L $NaHCO_3$ under different partial pressures of $CO_2$ are shown in Figure 4-7 and Figure 4-8. The cathodic current densities were significantly higher in the presence of bicarbonate even though the test was under stagnant conditions. At pH 8.51, no hump was observed at -0.25 V but the cathodic current density was significantly higher than in the CV of magnetite at pH 7.94 in the absence of bicarbonate species in the solution. At pH 5.08, under low partial pressure of $CO_2$, the hump was still noticeable. The results suggest that the presence of bicarbonate results in a higher reduction rate of magnetite.

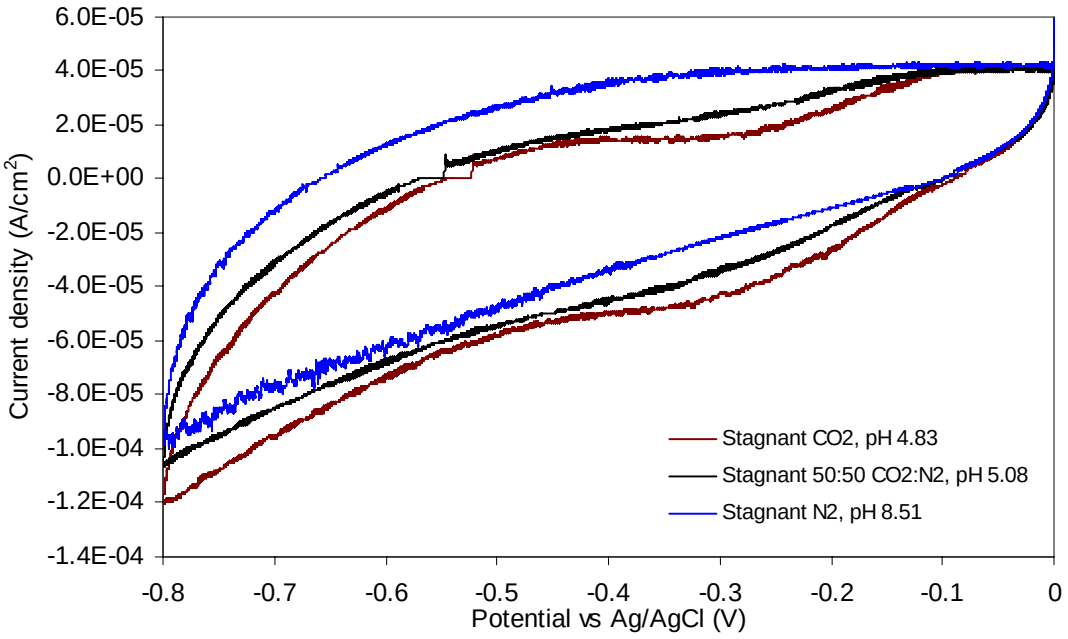


Figure 4-7: Cyclic voltammograms of magnetite in 30 g/L NaCl brine solution buffered with 0.1 g/L $NaHCO_3$, deaerated with $N_2$ (pH 8.51), $CO_2$ (pH 4.83) and 1:1 ratio of $CO_2$ and $N_2$ mix (pH 5.08), measured under stagnant conditions at scan rate of 2 mV/s.

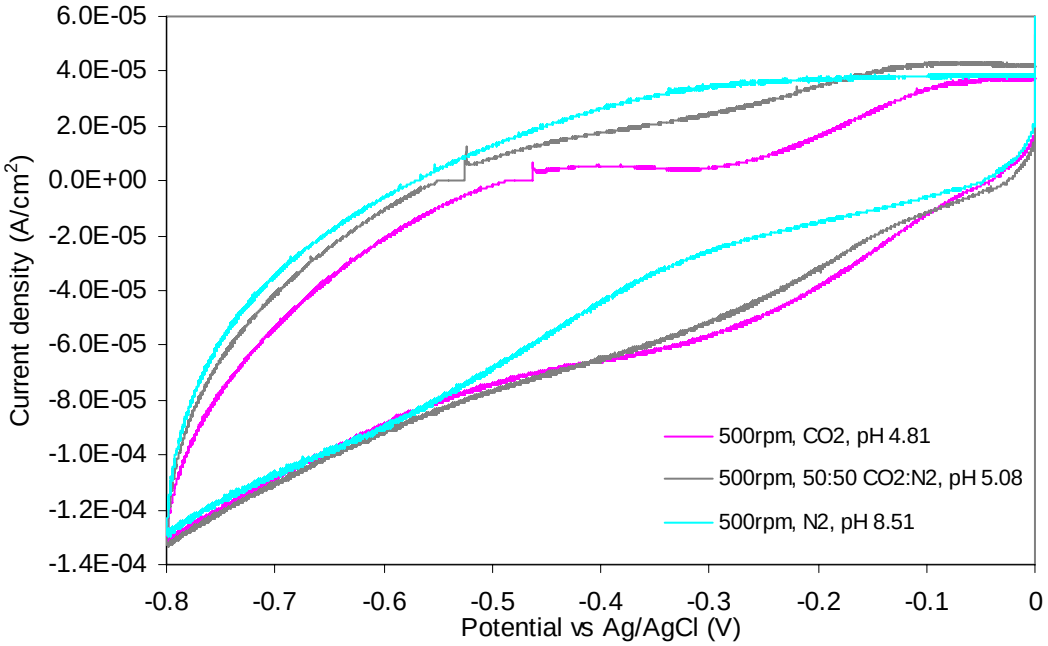


Figure 4-8: Cyclic voltammograms of magnetite in 30 g/L NaCl brine solution buffered with 0.1 g/L $NaHCO_3$, deaerated with $N_2$ (pH 8.51), $CO_2$ (pH 4.83) and 1:1 ratio of $CO_2$ and $N_2$ mix (pH 5.08), measured at 500 rpm rotational speed and at scan rate of 2 mV/s.

An overview of the CV of magnetite under a range of conditions is presented in Figure 4-9. A general trend is observed with respect to the pH in the forward reduction sweep and the reverse oxidation sweep. The cathodic current of the CV of magnetite increases with a decrease in the solution pH; whereas the anodic current increases with an increase in the solution pH. It appears that the oxidation reaction of the reduced species is favoured at higher pH and the reductive dissolution reaction is favoured at lower pH. The presence of bicarbonate species influenced the rate of the reductive dissolution of magnetite. It is evident that the high galvanic current observed in the previous chapter on galvanic corrosion, even at low solution pH, has a significant contribution from the reductive dissolution reaction of magnetite. The presence of carbon dioxide increases the reductive dissolution rate of magnetite.

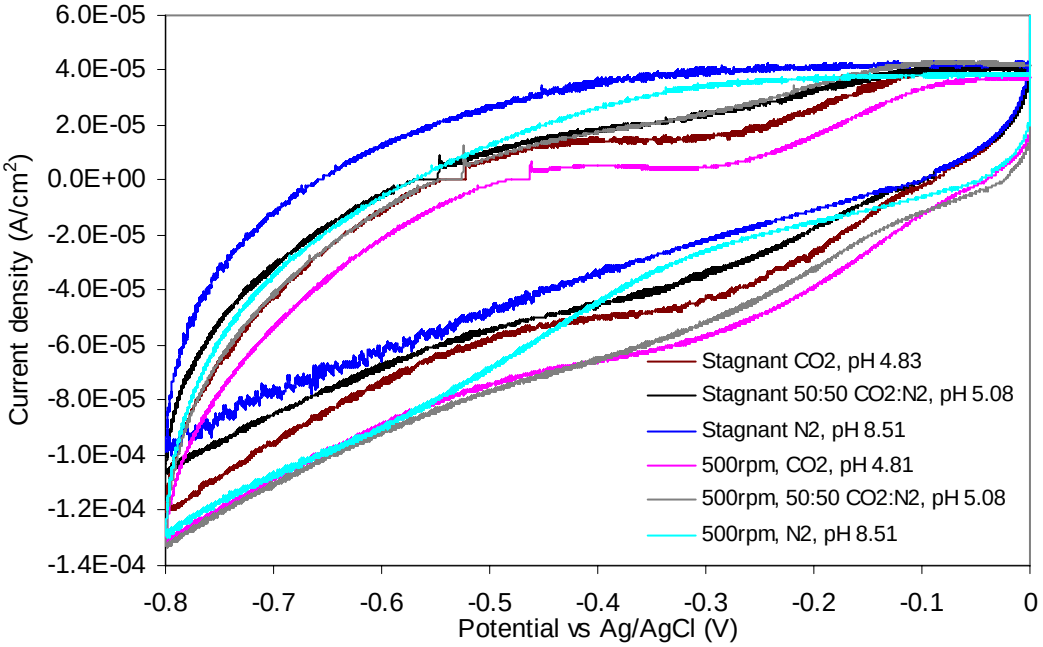


Figure 4-9: Cyclic voltammograms of magnetite in 30 g/L NaCl brine solution buffered with 0.1 g/L $NaHCO_3$, deaerated with $N_2$ (pH 8.51), $CO_2$ (pH 4.83) and 1:1 ratio of $CO_2$ and $N_2$ mix (pH 5.08) at scan rate of 2 mV/s.

#### 4.3.1.4. Reduction at high cathodic potential

In the previous section, the study of the reductive behaviour of magnetite was limited to -0.8 V (vs Ag/AgCl) in order to simulate the coupled potential of magnetite and carbon steel. Nevertheless, further investigation at higher cathodic potential may provide additional information on the reductive behaviour of magnetite. Several authors have hypothesized that the $Fe^{2+}$ in magnetite can be reduced to metallic iron (Fushimi et al., 2002; Haruyama & Masamura, 1978; Holser & Schneer, 1961). It seems quite feasible for magnetite to reduce to Fe but there is limited work that has clearly justified the reduction mechanism of magnetite. Hence, the cyclic voltammetry technique was again used to study the reduction reaction of magnetite at higher reductive potential. A faster scan rate at 20 mV/s was applied for the wider reduction potential range to minimise damage on the magnetite electrode. The results in Figure 4-10, under $CO_2$ sparging at the pH of 4.87, show no reductive peak when the potential is swept to -1.1 V.

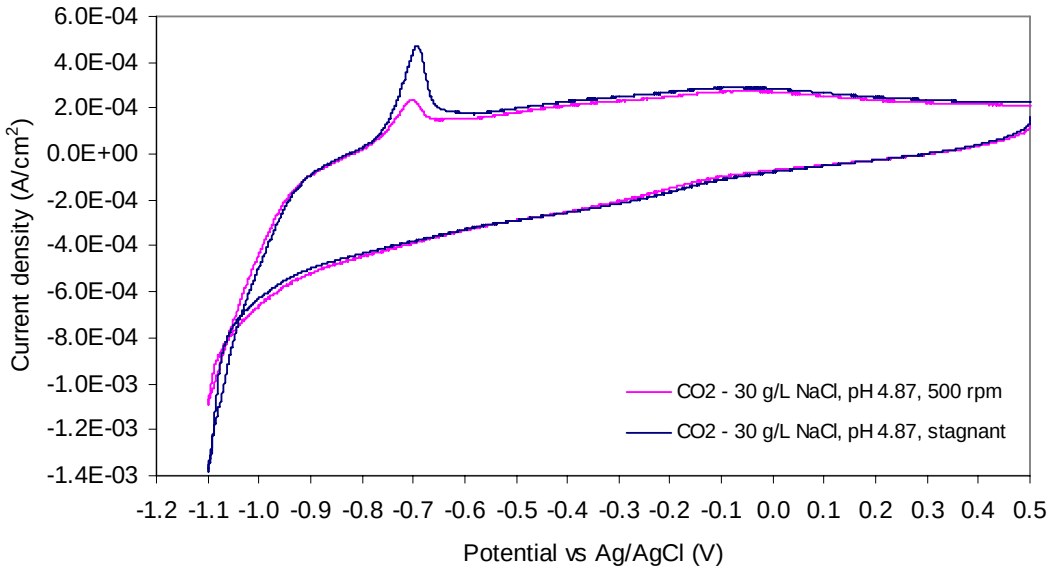


Figure 4-10: Cyclic Voltammograms of magnetite in 30 g/L NaCl added with 0.1 g/L $NaHCO_3$ to pH 4.87, deaerated with $CO_2$ and measured at scan rate of 20 mV/s

However, the cathodic current density increased drastically after passing -0.8 V. This observed drastic increase in the reduction current density was interpreted as being an occurrence of a surface involving the transformation of the solid and not reduced species of $H^+$ because the reduced species of $H^+$ would have dissolved into solution

under rotation. On reverse scan, the oxidation reaction of $H^+$ would not form a solid phase on the electrode surface to result in a noticeable peak. The product that was formed on the surface was then oxidised on the reverse sweep, with a clear oxidative peak at around -0.75 V. The peak at the -0.75 V matched sensibly with the equilibrium potential of Fe oxidation to $Fe^{2+}$. It has been confirmed by Haruyama that the reduction reaction in a nitrogen deaerated perchloric acid solution at pH 2 at -1.1 V is an event of reduction to Fe.

Comparing the results under stagnant conditions and with rotation, the height of the peak under stagnant conditions was about twice the current density of the reverse oxidation sweep of magnetite under rotation. The oxidation peak was still noticeable even with rotation of the electrode, but the oxidation current density peak was lower. This suggests that the dynamic movement of the electrode facilitated the transport of the reduced species from the lattices into the solution and affected the subsequent reduction reaction rate to Fe at -1.1 V. In addition, the latter reduction reaction did not seem to be a direct reduction from magnetite to Fe but via an intermediate reduced species from the former reduction reaction. This interpretation will be justified in the later tests at higher pH. Besides, there was no noticeable peak on the reduction sweep except for the slight hump at -0.25 V as seen and discussed previously. Since the CV was obtained at a higher scan rate, the reductive dissolution peak at -0.25 V was not pronounced.

The presence of carbon dioxide and bicarbonate were found to increase the reductive dissolution reaction of magnetite. If the reduction at -1.1 V was a direct conversion from magnetite, and not from an intermediate reduced species, the oxidative peak at -0.75 V should be observed regardless of solution pH. However, the CV of magnetite in a brine solution without bicarbonate buffer or carbon dioxide, at pH 7.86, as shown in Figure 4-11, did not show any noticeable oxidation peak. The concurrent disappearance of the reductive hump at -0.25 V and the oxidative peak at -0.75 V under high pH solution suggests that both reactions were interrelated. The reductive reaction to Fe was confirmed to be not a direct magnetite conversion as suggested by Haruyama and Masamura (Haruyama & Masamura, 1978) but via the intermediate $Fe^{2+}$ which was reduced at lower cathodic potential and remained on the surface of the magnetite lattice.

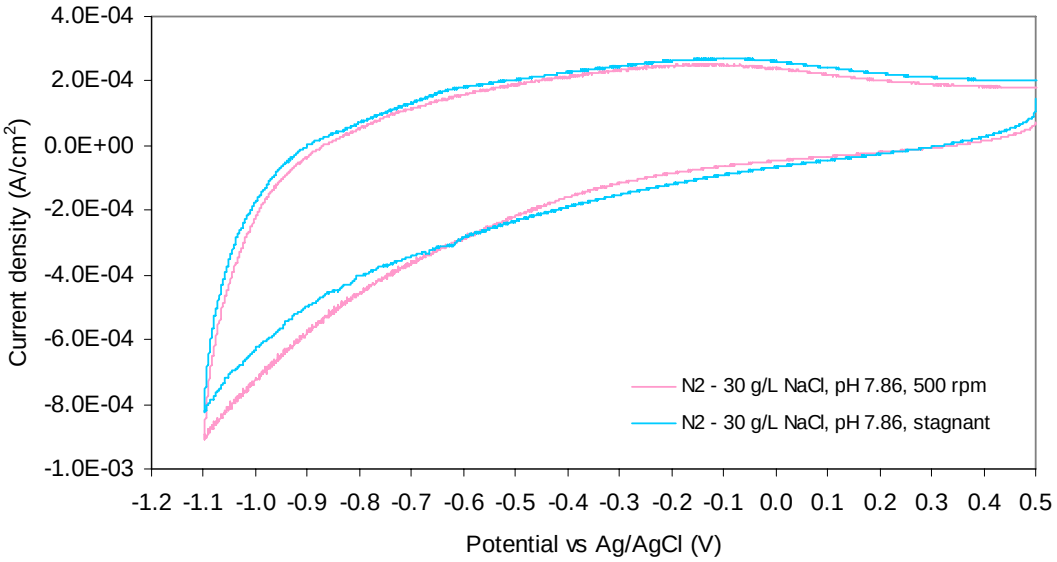


Figure 4-11: Cyclic Voltammograms of magnetite in 30 g/L NaCl at pH 7.86, deaerated with $N_2$ and measured at scan rate of 20 mV/s.

### 4.3.2. Effect of reduction on the semiconductor behaviour of magnetite

The Mott-Schottky analysis has been used previously to study the semiconductor behavior of iron oxide such as magnetite and hematite, but the potential range studied was limited to low cathodic potential in order to limit the possible changes due to reduction of the iron oxide (Wielant, Goossens, Hausbrand, & Terryn, 2007). So far, there is no study that justifies how the semiconductor property could change when the iron oxide is reduced. Therefore, a full range of cathodic potential from 0.3 V to -1 V was applied to study the semiconductive property change in magnetite. The Mott-Schottky plots of magnetite in standard brine under $CO_2$ (at pH 4.87) and $N_2$ (at pH 8.87) at 30$^{o}$C and are shown in Figure 4-12.

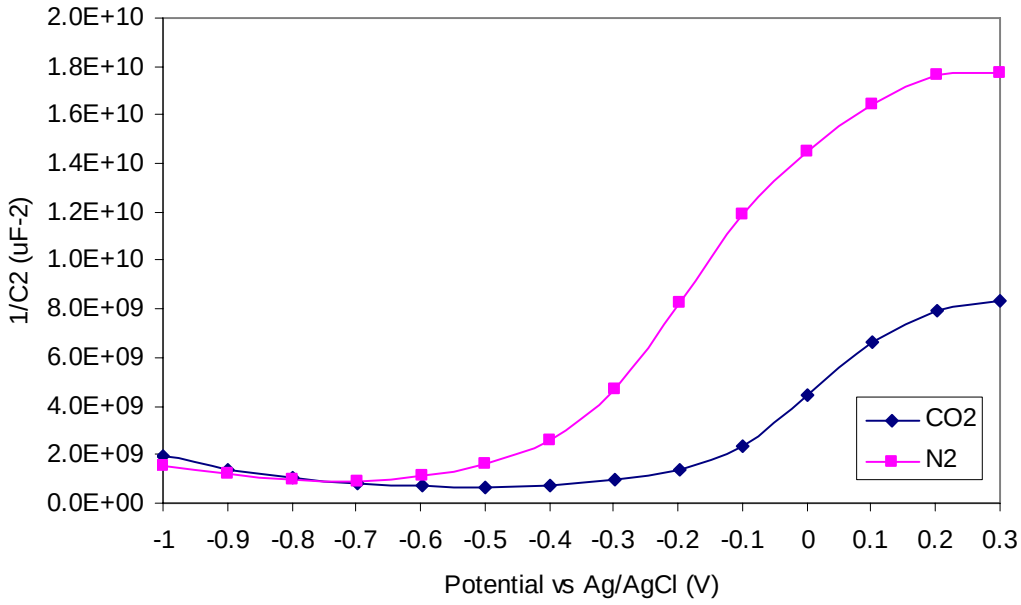


Figure 4-12 Mott-Schottky plots of magnetite in standard brine solution under $CO_2$ (pH 4.87) and $N_2$ (pH 8.87) at 30$^{o}$C.

The Mott-Schottky plots of magnetite are not linear in the high cathodic potential range of -1 V to 0.3 V. The plots consist of two curves showing a positive gradient (n-type semiconductor) towards oxidative potential which then flex at a higher cathodic potential to a negative gradient (p-type semiconductor) towards higher reductive potential. However, the point of inflexion was different under different experimental conditions. Under $CO_2$ (pH 4.87), the inflexion point started at around -0.4 V; whereas under $N_2$ (pH 8.87) the inflexion point was around -0.7 V. This transition of an n-type semiconductor to a p type semiconductor for magnetite seems to be affected by the solution pH. Since the reductive dissolution behavior of magnetite was justified in the previous section, the change in the semiconductor property of magnetite could be a result of the reduction reaction and associated transformation into another iron compound.

Iron, being a transition metal, and known for its chemical complexity, can form different iron compounds depending on pH, temperature, applied potential, solution species and the surrounding environment. Since the formation of different iron products can be estimated from thermodynamic equations according to pH, activity, pressure and temperature, a simple Pourbaix diagram as seen in Figure 4-13 can be

generated readily as a guide to predict iron conversion. Each region of the most stable iron species is bounded by equilibrium lines. Magnetite is bounded by $Fe^{2+}$ and $Fe^{3+}$ species. The stability of the iron species strongly depends on pH and potential. As such, applying a potential to magnetite can change its chemical, physical and electronic properties.

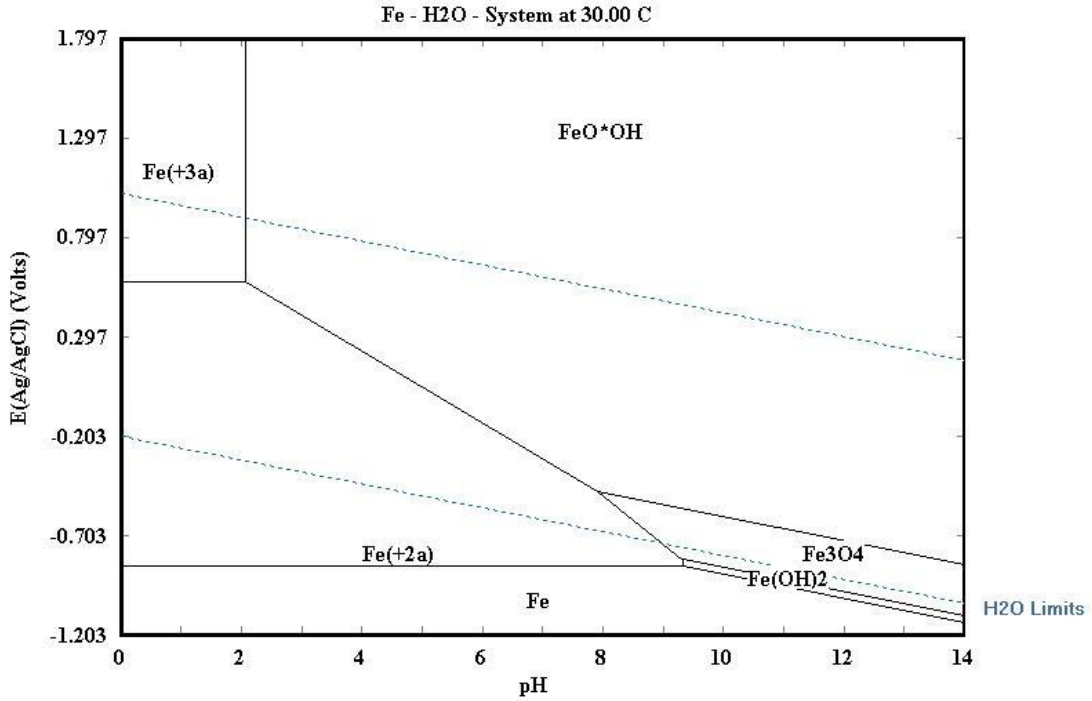


Figure 4-13 Pourbaix diagram of Fe-$H_2O$ at 30$^oC$ and $Fe^{2+}$ concentration of $10^{-6}$ M generated by HSC Chemistry software.

If magnetite can exist as either n or p-type semiconductor as stated by Cornell and Schwertmann (Cornell & Schwertmann, 1996), the band theory would be able to justify this transition of the states. According to the band theory, magnetite in its normal stable state is an n-type semiconductor with its Fermi level lying just below the conduction band (Bott, 1988). Since the Fermi level is higher than the redox potential of the electrolyte solution, electrons will transfer from the electrode into solution effortlessly, leaving a positive charge in the space charge region with an upward bending of the band edges as illustrated in Figure 4-14. By applying an anodic potential to magnetite, it forces the cloud of electrons out, causing an excess of electrons in the space charge region which deflects the band edge downwards with an accumulation region. With the abundance of electrons for charge transfer in the

accumulation layer, the electron transfer reactions occur rapidly, similar to a metallic electrode (Bott, 1988). In contrast, when a reverse potential (cathodic potential) is applied, electrons are pumped into the magnetite and results in a depletion layer with an upward bending of the reflected band edges. This depletion layer contains fixed equal but opposite charges which act like a charged capacitor (Rosenberg, 1988). This band theory relates closely to the increase in the capacitance of an n-type semiconductor being polarized cathodically. Therefore, it is unlikely that the capacitance of an n-type semiconductor would decrease at extremely high cathodic potential (close to the reduction potential of $Fe^{2+}/Fe$) while most holes are being filled with electrons which would have retarded the charge transfer rate and increase in its space charge capacitance.

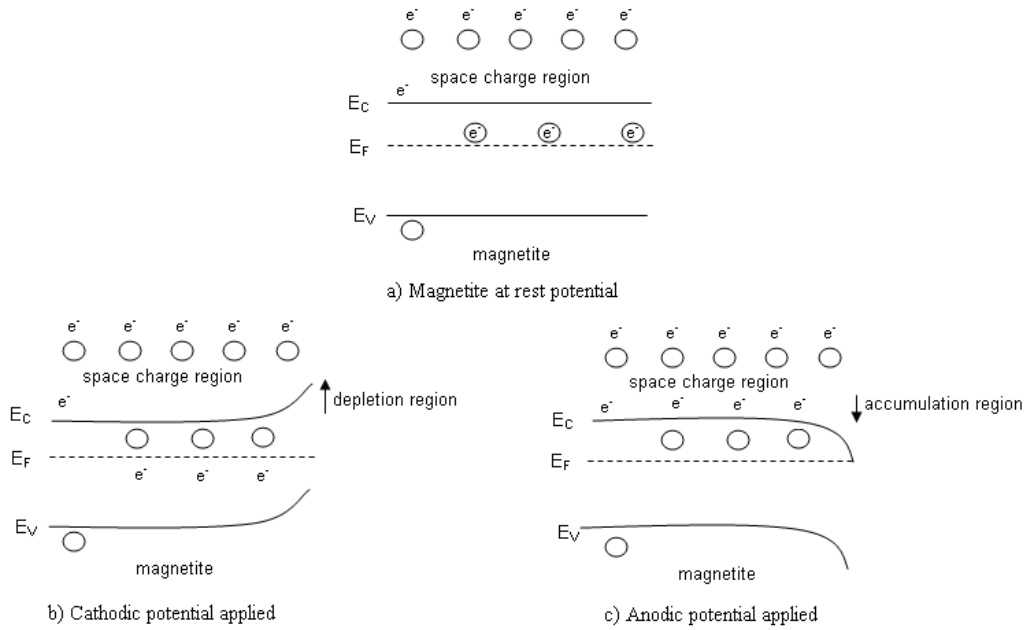


Figure 4-14 Band bending of magnetite a) at rest potential, b) cathodic potential applied and c) anodic potential applied.

A stable intrinsic or extrinsic semiconductor would have a linear curve with either positive or negative gradient. However, magnetite is not a stable semiconductor, especially since the crystalline structure at the octahedral sites contains both $Fe^{2+}$ and $Fe^{3+}$. The electrical neutrality in a crystal is maintained by either having excess electrons in the crystal or changing the charge on the metal ions. Either way will likely change the electronic state of the iron atoms and cause a stoichiometric change in the magnetite. Subsequent to the change, the physical, chemical and electrical

property can be altered significantly. When an extreme anodic overpotential is applied (beyond the oxidation potential of $Fe^{2+}/Fe^{3+}$) , it oxidizes $Fe^{2+}$ to $Fe^{3+}$ spontaneously, resulting in the conversion to hematite. On the contrary, a sufficient cathodic overpotential can reduce $Fe^{3+}$, one possible product being hydrated ferrous ions in an electrolyte solution. Hematite is an n-type semiconductor due to Frenkel defects (Clegg, 1998). Therefore, magnetite being an n-type semiconductor when is further polarized anodically, will continue to show the characteristic of an n-type semiconductor with a positive gradient. The oxidation of magnetite to hematite can easily be identified from the physical colour change from black to red. However, the identification of the reduced species of magnetite is quite challenging because the reduced species such as FeO and $Fe(OH)_2$ are less stable and they react readily with oxygen to transform to a thermodynamically stable ferric compound such as FeOOH, $Fe_3O_4$ or $Fe_2O_3$. Hence, an ex-situ analysis of the reduced magnetite could not accurately deduce the reduction reaction. Therefore, an in-situ analysis is needed to resolve the transformation. The occurrence of $Fe(OH)_2$ as a intermediate corrosion product has been reported in in-situ Raman analysis experiments, corrosion modeling and cation hydrolysis reaction. However, a careful review of literature related to $Fe(OH)_2$ dated from the 1950s till now showed many discrepancies on the thermodynamic data, solubility products, physical, electronic and chemical properties reported. To date, there is still no scientific data available on the electronic state of $Fe(OH)_2$. Therefore, the occurrence of this p-type semiconductor transition of magnetite could be due to the reduced species such as $Fe(OH)_2$ and not magnetite itself.

The results in the previous section showed that the reductive dissolution rate of magnetite at potential -0.25 V was affected by the solution pH. At potentials between -0.4 V to -0.9 V, another reduction event of the transformation to ferrous hydroxide was postulated. Since the potential range at the transition of the semiconductor type lies within the postulated potential range of the formation of ferrous hydroxide, thermodynamic calculation can be used to test the feasibility of the reaction. The calculated results are represented in a pH-potential diagram as shown in Figure 4-15. The pH and the potential at the inflexion points on the Mott-Schottky plots matched with the predicted pH and potential of the $Fe_3O_4$ to $Fe(OH)_2$ equilibrium line as indicated in the equilibrium diagram. The reduction potential estimated at pH 4.87

was -0.55 V and at pH 8.87 was -0.77 V. The difference in solution pH results in a shift in the equilibrium potential of the reaction. Overall, the experimental results and thermodynamics prediction are consistent with the hypothesis that magnetite reduces to ferrous hydroxide. This established that magnetite can be reduced to ferrous hydroxide and the semiconductor type changes from n-type to p-type.

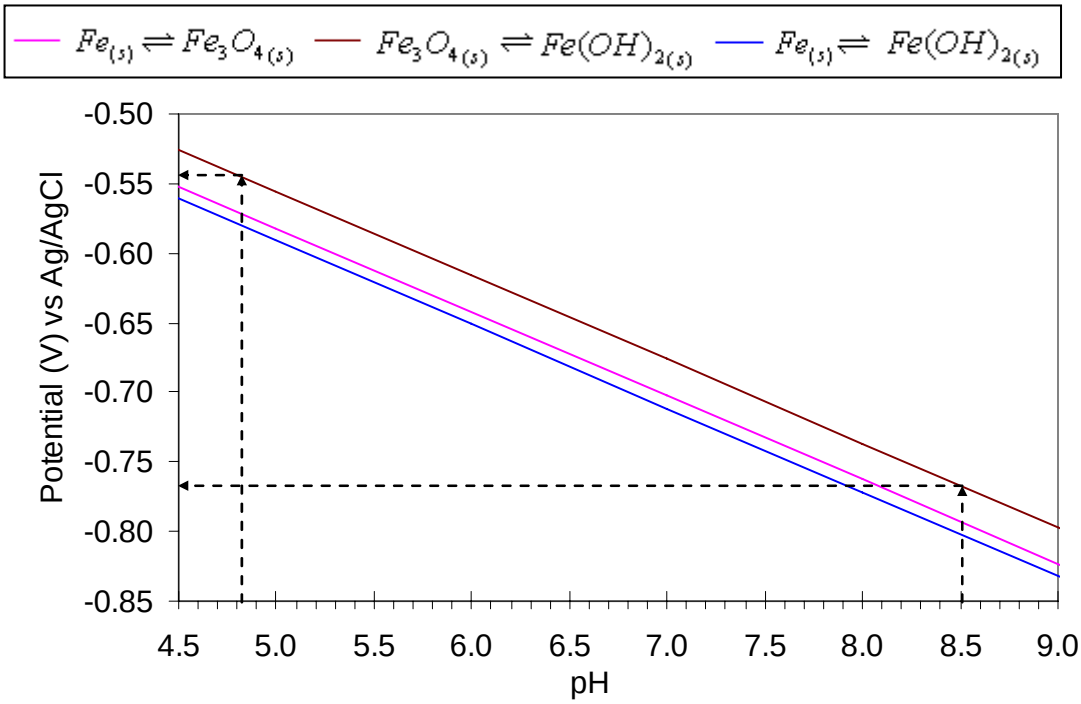


Figure 4-15 Potential-pH equilibrium of Fe-$H_2O$ at 30$^{o}$C.

### 4.3.3. In-situ study of magnetite reduction

Subsequent to the results from both cyclic voltammetry and Mott-Schottky analysis, which strongly indicate changes to the magnetite when it was cathodically polarised, an in-situ Raman technique was adopted to confirm the observed changes in-situ. A combined Raman spectroscopy / microscopy / electrochemical polarisation was performed to identify the reduced species on the magnetite and to image the changes on the magnetite surface in-situ. The Raman spectra at hourly intervals during the polarisation are presented in Figure 4-16. There was no new Raman peak observed in the spectra for the first three hours but the intensity of the magnetite stretch at 660 $cm^{-1}$ subsided but the peak at around 550 $cm^{-1}$ broadened and intensified towards the fourth hour. The band at 550 $cm^{-1}$ is claimed to be the $T_{2g}$ mode of the Fe-O asymmetric bend but this band is also associated with the Fe-OH bend (Simpson & Melendres, 1996). If this band denotes a $T_{2g}$ stretching mode, the intensity of this band should increase in parallel to the $E_g$ symmetric stretch of Fe-O at 660 $cm^{-1}$ but the results showed vice versa. Therefore, this band at 550 $cm^{-1}$ is most likely an $A_1$ symmetrical bend of Fe-OH. Normally, an appearance of a broad Raman peak denotes an amorphous or a poorly crystalline phase. Hence, the broadening and the intensification of this 550 $cm^{-1}$ band were related to an accumulation of an amorphous hydroxide phase. The cathodic polarisation of magnetite reduced the $Fe^{3+}$ to $Fe^{2+}$ which partially dissolved into solution and hydrolysed and formed poorly crystalline iron (II) hydroxide.

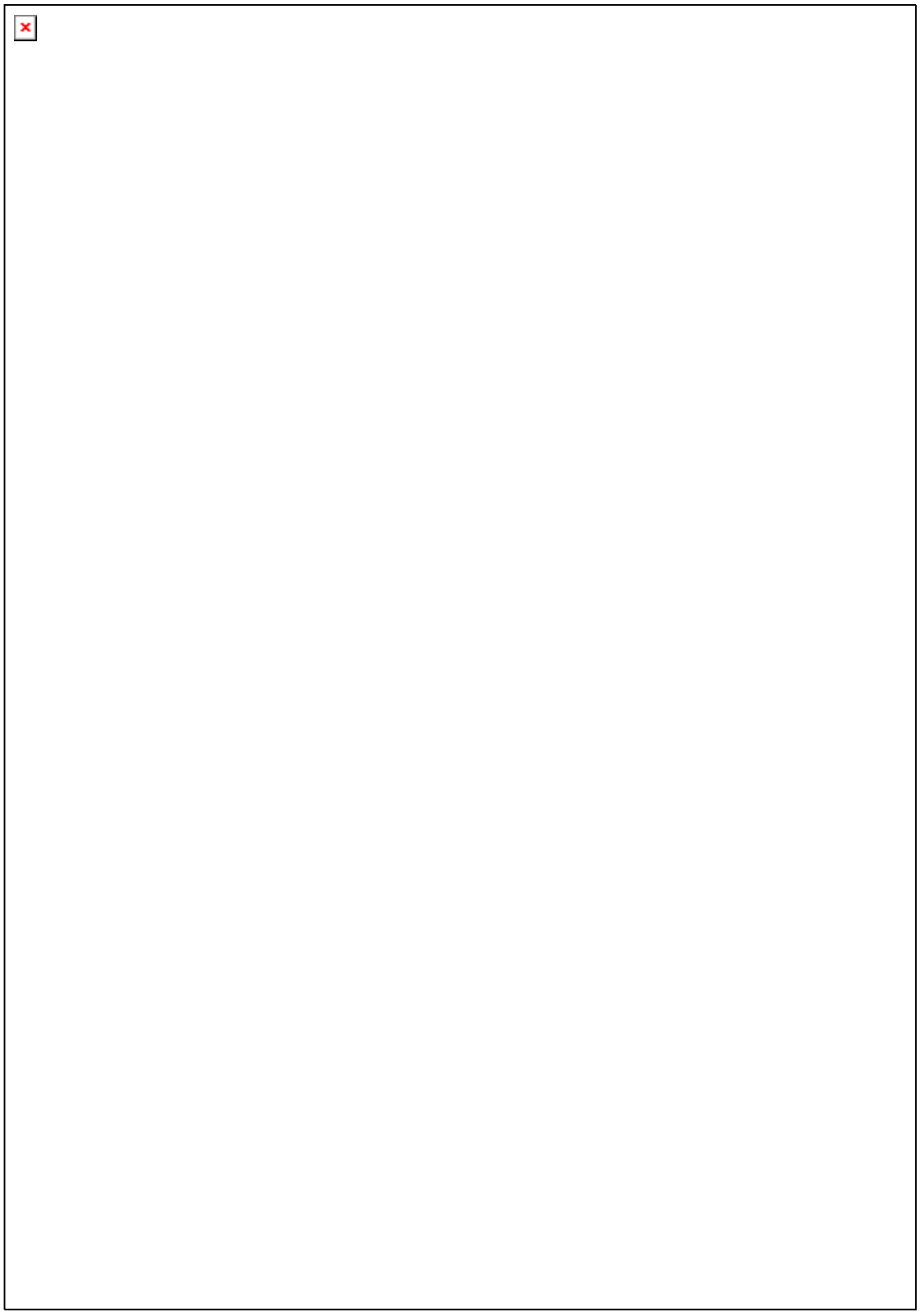

Figure 4-16 In-situ Raman spectra of magnetite electrode polarised at –0.65 V in standard brine solution containing 30 g/L of NaCl and 0.1 g/L of $NaHCO_3$ under carbon dioxide at 30$^{o}$C for 4 hours.

The hydroxyl iron compound is not stable and can be oxidised readily upon exposure to air. This was evident in the ex-situ Raman results on the polarised magnetite removed from the anaerobic system. Upon exposure to the atmosphere, the hydroxyl iron was oxidised almost instantaneously after being removed from the anaerobic system. An ex-situ Raman spectrum was acquired from the polarised magnetite immediately after the sample was removed from the Raman cell and is shown in Figure 4-17. Clearly, two new peaks were observed at approximately 320 $cm^{-1}$ and 471 $cm^{-1}$. The appearance of the 320 $cm^{-1}$ broad band was observed previously in Misawa and co-workers' work after the oxidation of Fe(II) solution. As many aquo-complexes of metals show a Raman peak in this region, this band was assigned to the symmetric stretching vibration of an Fe-O-Fe group in the complex in which one Fe(II) and three Fe(III) are linked by oxygen atoms (Misawa, Hashimoto, Suëtaka, & Shimodaira, 1973). The 471 $cm^{-1}$ band was assigned to magnon scattering (De Faria et al., 1997). It is clear that the ferrous ions on the reduced magnetite and in the solution transformed to a stable ferric compound almost instantaneously upon exposure to oxygen.

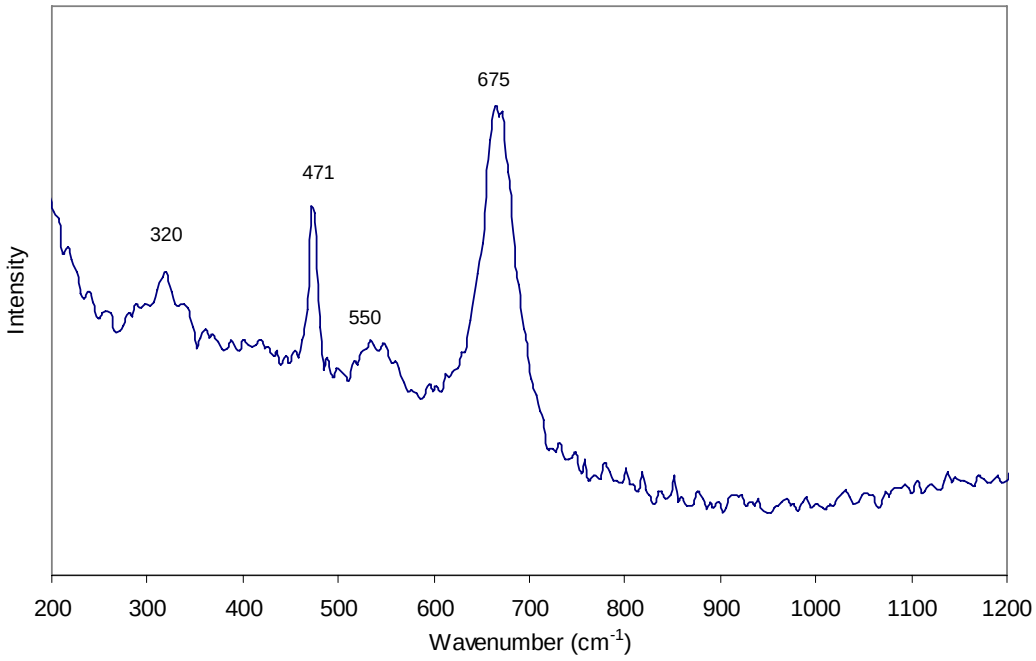


Figure 4-17: Raman spectra taken immediately after removal from the Raman cell of the polarised magnetite electrode, exposed briefly to air.

The surface appearance of the magnetite at every hour was captured through a Plan 20x Nikon objective lens mounted on the WiTec Raman/near-field scanning optical

microscope. The pictures in Figure 4-18 clearly show some changes on the surface as the polarisation went on. At the start of the polarisation, the magnetite surface was clear under the microscope with visible grinding marks. After one hour, the surface was blurring under the optical microscope. This blurring effect could be a result of reductive dissolution of magnetite that formed an amorphous coating on the surface. Therefore, an ex-situ surface analysis using the SEM would help to support the microscopy images of the event of reductive dissolution of the magnetite.

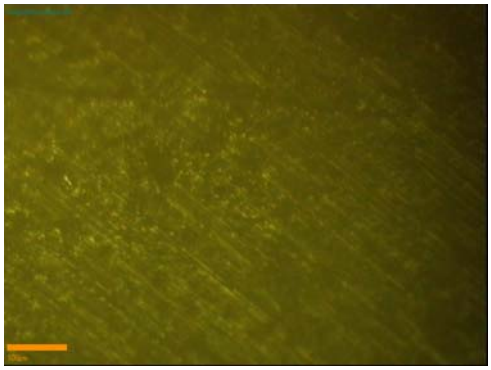

a) 0 hour (beginning of polarization)

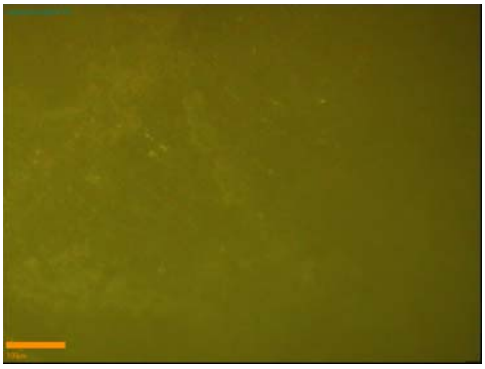

b) 1 hour

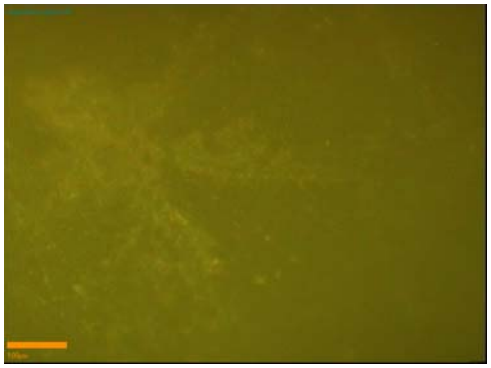

c) 2 hour

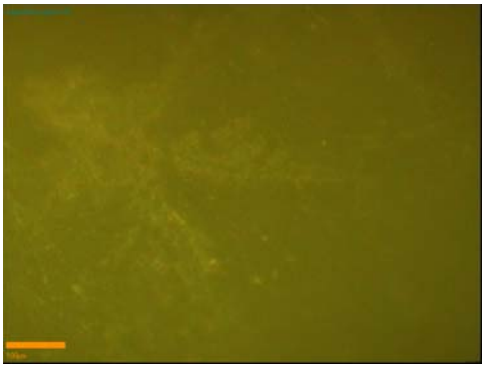

d) 3 hour

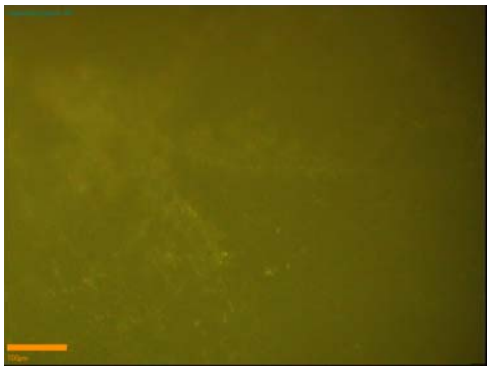

e) 4 hour

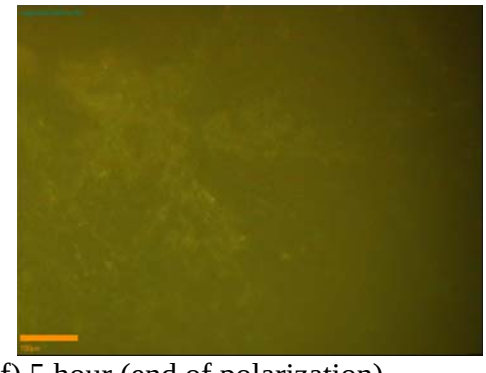

f) 5 hour (end of polarization)

Figure 4-18: Image of the magnetite surface polarised at –0.65 V vs Ag/AgCl in standard brine solution under carbon dioxide at 30$^{o}$C for 4 hours.

### 4.3.4. Ex-situ study of magnetite reduction

The low resolution microscopy images from the in-situ magnetite reduction could not clearly show the reductive dissolution event of magnetite. A normal SEM topography of a freshly polished magnetite sample without any electrochemical treatment is shown in Figure 4-19. If there was a nano scale structure present on the magnetite surface, it would not be resolved under SEM due to limitations of the instrument. Therefore, a refined surface analysis, using FESEM, was carried out to provide the finest detail of the surface morphology. The untreated magnetite surface is shown in Figure 4-20. The fine nanoscale structure of the surface was clearly projected under the FESEM. The surface morphology of magnetite was rough as seen under low magnification because of the geological defects of the mineral rock. Clearly, there is a difference in intensity of the backscattered electrons between the surface and the nano size needles, which were hardly noticeable under the conventional SEM because of the limitations of the instrument.

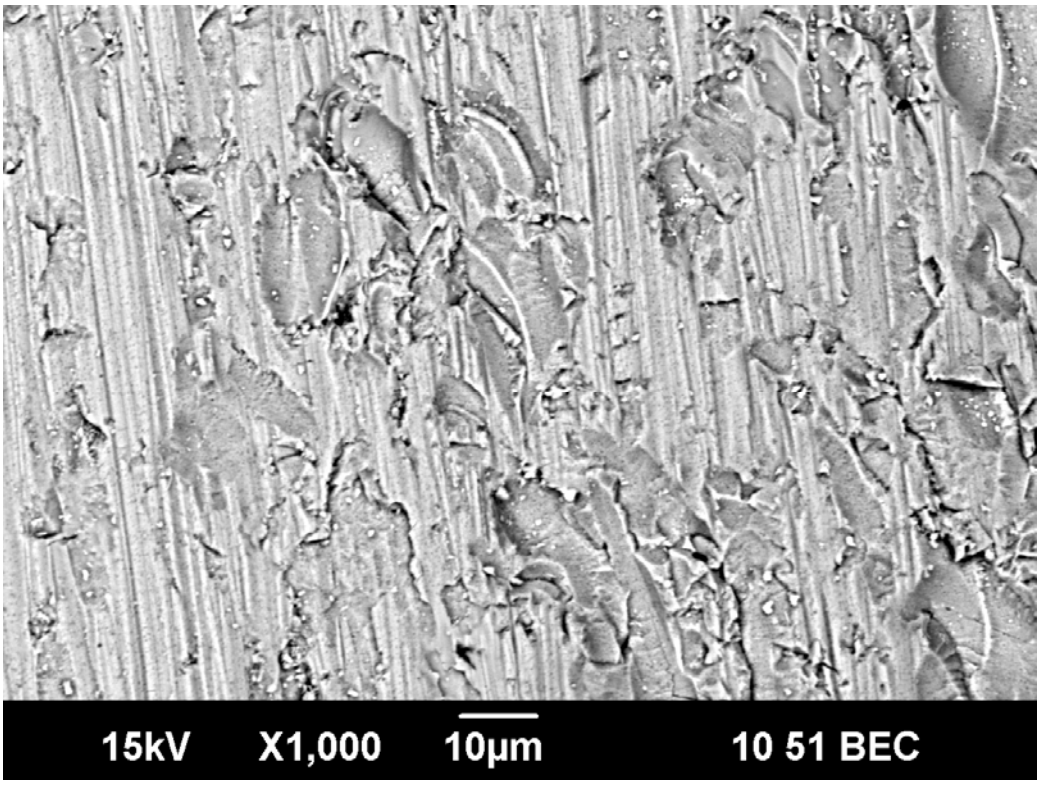


Figure 4-19 SEM image of unpolarised magnetite at 1000x magnification and EHT 15 kV.

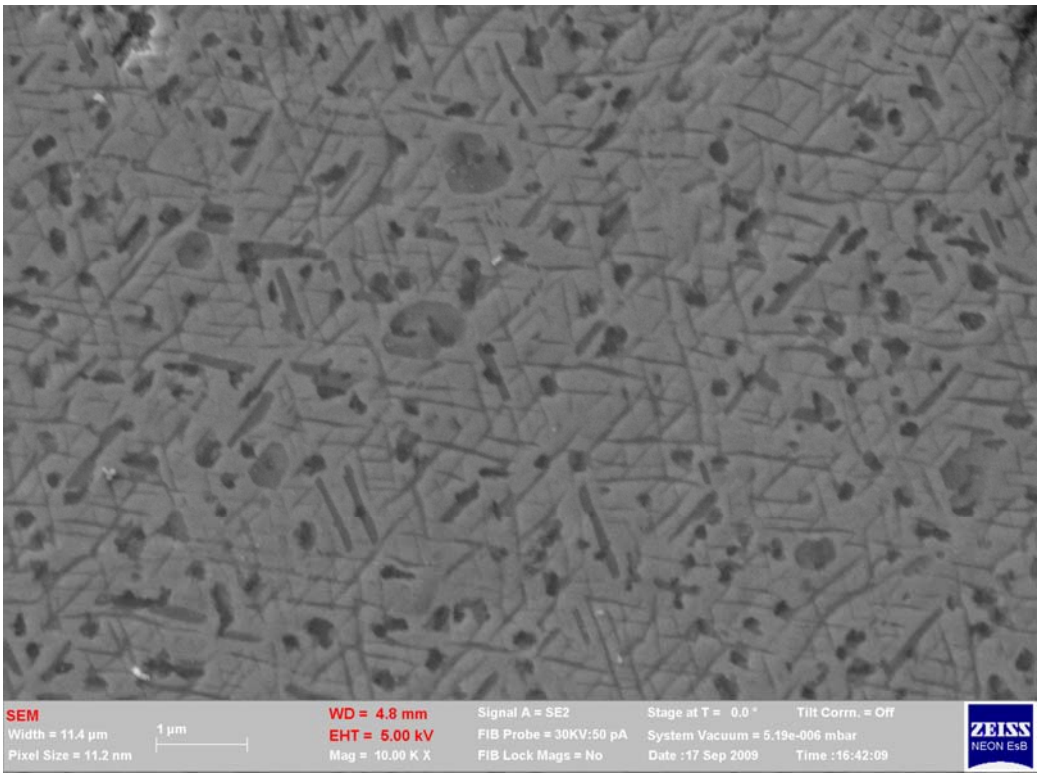


Figure 4-20 FESEM image of unpolarised magnetite polished at 10,000x magnification and EHT 5 kV.

In order to verify the earlier observation on dissolution of magnetite, a polarised magnetite sample prepared from the same conditions as the in-situ Raman test was analysed. A drastic morphology change of the polarised magnetite was apparent under the FESEM as shown in Figure 4-21. The dissolution of the iron components in magnetite left the mesh like structure and surface roughening. The iron intensity from the EDS analysis dropped significantly after being polarised. This is presumably because impurities enriched on the surface while iron was dissolved into the solution. The mesh like structure appears just like the needle shape phase as seen earlier in Figure 4-20 on the unpolarised magnetite. This mesh-like crystalline has a similar needle-like structure of the hydroxyl iron compound and could be an oxy/hydroxyl iron compound.

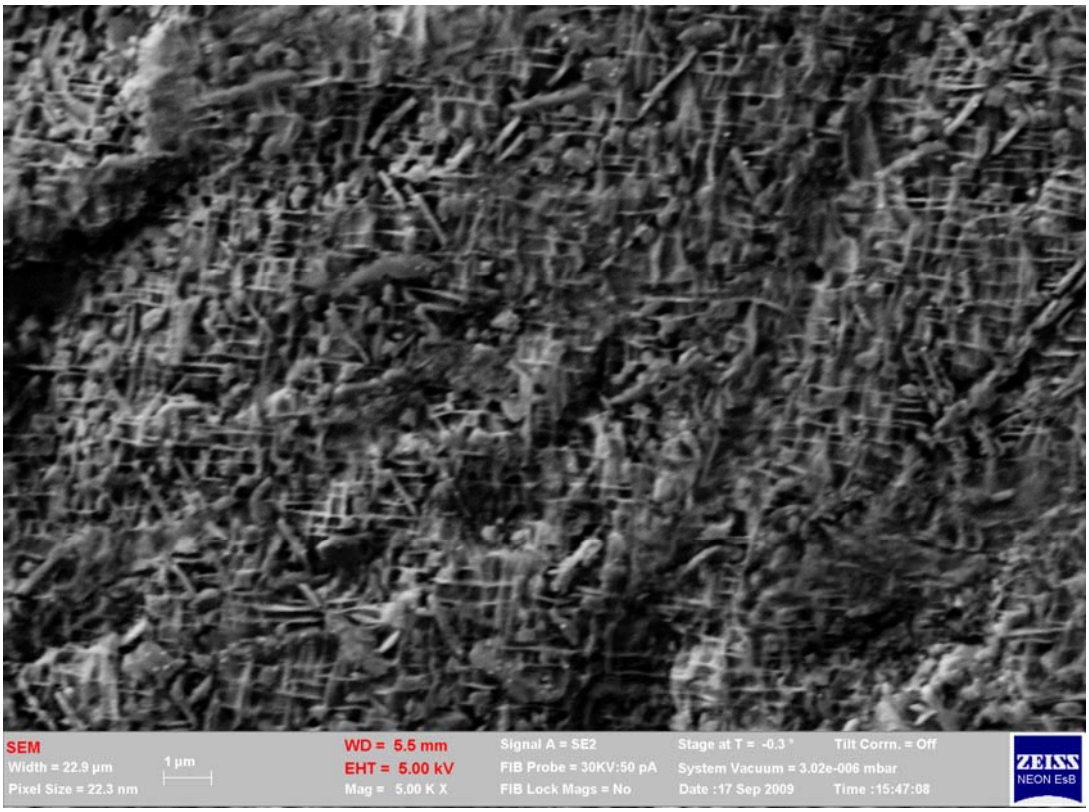


Figure 4-21 FESEM image at 5000x magnification and EHT 5 kV of magnetite after polarisation in $CO_2$ sparged standard brine solution.

The results of the FESEM clearly showed that magnetite undergoes reductive dissolution when it is polarized cathodically. The hypothesis, developed in Chapter 3, of magnetite partaking in the galvanic corrosion is valid from all the evidence found in the in-situ and ex-situ analysis.

## 4.4. CONCLUSIONS

The cyclic polarisation results confirmed that magnetite underwent reductive dissolution when it was polarised cathodically. The reductive dissolution reaction of magnetite appeared at around -0.25 V vs Ag/AgCl and depended strongly on the solution pH. The dissolution effect increased with the concentration of carbonic acid and also the presence of bicarbonate in the solution. The ferric ion in magnetite reduces to ferrous ion and is dissolved in acidic solution. When the cathodic sweep exceeded -1.1 V, magnetite was reduced to Fe. This reduction reaction was not a direct conversion of magnetite but via the intermediate $Fe^{2+}$ which was reduced at lower cathodic potential and remained on the surface of the magnetite lattice.

Furthermore, the ferrous ion can be hydrolysed and transform into ferrous hydroxide, according to pH and potential. Magnetite is an n-type semiconductor but the electronic state changes from an n-type to a p-type semiconductor as it reduces to ferrous hydroxide. This reductive transformation was verified from the observed broadening of the Fe-OH stretch at 550 $cm^{-1}$ and the suppression of the Fe-O band at 660 $cm^{-1}$ Raman bands in in-situ study of the magnetite reduction.

# CHAPTER 5 CONCLUSIONS

The discovery of the underlying chukanovite and magnetite scale in the order of nanometers has clearly showed that iron carbonate scale is not the primary corrosion product scale formed under carbon dioxide corrosion of carbon steel at low partial pressure of $CO_2$. The formation of corrosion product scales was found to be dependent on the pH, temperature and $CO_2$ partial pressure dependent. Individual products have unique structure that can be clearly identified using the FESEM. The development of chukanovite and magnetite scales caused a higher corrosion rate of the carbon steel before the steel is passivated by the combined corrosion product scales. Iron carbonate scale forms later in the corrosion process when its solubility product limit is exceeded and the iron carbonate then precipitates over the underlying scale of nanometer dimensions. In the absence of carbon dioxide, magnetite was the main corrosion product formed. The well defined magnetite crystal structure formed in the absence of carbonate species was found to produce a semiconductive scale on the carbon steel which had distinguishable double capacitive loops in the Nyquist plot compared to the scale formed under low partial pressure of $CO_2$.

The three reactions involved in the scale development are hydrolysis, oxidation and precipitation. Chukanovite is the preferred hydroxide phase formed via the hydrolysis reaction in the presence of carbon dioxide. Subsequent to the hydrolysis reaction, an oxidation reaction of the ferrous ion in the hydroxide phase takes place to form magnetite. As the iron and carbonate concentrations exceed the solubility limit of iron carbonate, iron carbonate will then precipitate rapidly over the underlying scale layer. Thermodynamic calculations can provide a reasonable estimation of the conditions in which magnetite and iron carbonate will form a thermodynamically stable product; but it fails to predict the formation of chukanovite as there is no thermodynamic data available for this new corrosion product.

The magnetite and carbon steel coupling result in galvanic corrosion of the carbon steel under carbon dioxide conditions. The carbon dioxide partial pressure, which influences the solution pH, affects not only the self corrosion rate but also the galvanic corrosion rate. At low pH, the self corrosion rate increases due to increase

carbonic acid attack; at pH close to neutral, the galvanic component from the magnetite reduction still results in a relatively high overall corrosion rate. In fact, it is mainly the additional reductive reaction which is the reductive dissolution of magnetite. The reductive dissolution reaction of magnetite increases with decreasing pH. Since the formation of magnetite is favoured at higher pH, pipelines operating at mildly acidic conditions will be risk of a high corrosion rate due to the galvanic coupling effect from the magnetite scale and the regeneration of the magnetite scale.

Corrosion inhibitors that work well in controlling self corrosion of carbon steel failed to inhibit the galvanic corrosion caused by magnetite. No definitive conclusion could be drawn to effectively control this galvanic corrosion. Furthermore, the formation and the existence of chukanovite scale and its influence in causing higher corrosion rates of carbon steel has not drawn global awareness. There is little recognition of its existence and influence in causing a higher corrosion rate of the carbon steel. It is important for more research to be driven into finding a solution to combat the accelerated corrosion caused by both magnetite and chukanovite scales.

## 5.1. SUGGESTIONS FOR FURTHER WORK

Discovery of the underlying chukanovite and magnetite scales and their association with the accelerated corrosion rate of carbon steel have given a preliminary insight into the cause of premature pipeline failure. Since the formation of these non-protective nanometer scales has been discovered using the appropriate detection techniques as outlined in this PhD thesis, it is highly recommended to kick off more research work to focus on chukanovite and magnetite scales, finding the right solutions to control and prevent corrosion.

As chukanovite scale is newly discovered as a corrosion product formed under carbon dioxide corrosion, there has been limited research in the literature to understand its formation, especially with respect to the conditions such as pH, temperature, pressure and solution species that will favour the formation of this nanometer scale. Furthermore, this chukanovite is brittle and its porous, nanometer thin lath-like structure can easily be destroyed and regenerated under dynamic

conditions of high flow velocity. Therefore, it is important to investigate this corrosion product scale further and to understand its influence on localized corrosion.

The brilliant results obtained from the synchrotron radiation facilities have clearly shown a tremendous potential of the synchrotron radiation in making more novel discoveries on the mechanism and inhibition of corrosion. Many other aspects of corrosion are yet to be explored using the synchrotron radiation and associated techniques. Though the preliminary results and test setup has successfully proven the capability of the combined electrochemical and synchrotron radiation techniques to elucidate the corrosion mechanism in-situ, there are still a lot of open questions on what causes the corrosion acceleration and how to resolve it. Perhaps, a longer beamtime and more research work using the synchrotron radiation will provide additional information to complete the mechanism of a corrosion cycle.

The extent of the factor of cathode to anode surface area ratio on the rate of galvanic corrosion needs to expand to a larger scale to determine if there is any limit of the ratio that will aggravate or plateau off the galvanic corrosion rate. As the method used in this research was based on samples from a block of pure magnetite, it will be very interesting to find out how the cycle of formation and reductive dissolution of the magnetite component in an actual corrosion product scale affects the galvanic corrosion mechanism.

The inhibition of galvanic corrosion caused by corrosion product scales needs further investigation. There are still no inhibitors that have been specially formulated to effectively target this type of corrosion. Therefore, a detailed inhibition study and design for this galvanic corrosion caused by magnetite coupling will be beneficial to the oil and gas industry to prevent premature pipeline failure.

# CHAPTER 6 REFERENCE LIST

Al-Mayouf, A. M. (2006). Dissolution of magnetite coupled galvanically with iron in environmentally friendly chelant solutions. *Corrosion Science, 48*(4), 898-912.

Al-Mayouf, A. M., Al-Mobarak, N. A., & Al-Swayih, A. A. (2007). Dissolution of magnetite coupled with iron of various surface areas. *Corrosion, 63*(10), 916.

Allen, P. D., Hampson, N. A., & Bignold, G. J. (1978). The effect of electrical potential on the dissolution of iron oxide crystals I. A review of selected relevant literature. *Surface Technology, 7*(4), 273-287.

Allen, P. D., Hampson, N. A., & Bignold, G. J. (1980). The electrodissolution of magnetite: Part II. The oxidation of bulk magnetite. *Journal of Electroanalytical Chemistry, 111*(2-3), 223-233.

Baboian, R. (1976a). Electrochemical techniques for predicting galvanic corrosion. In R. Baboian, W. D. France, L. C. Rowe & J. F. Rynewicz (Eds.), *Galvanic and pitting corrosion - Field and laboratory studies* (Vol. ASTM STP 576, pp. 5-19): American Society for Testing and Materials.

Baboian, R. (1976b). *Galvanic and pitting corrosion: field and laboratory studies : two symposia presented at the 1974 Materials Engineering Congress, American Society for Testing and Materials, Detroit, Mich., 22-23 Oct. 1974*. Philadelphia, Pa.: A.S.T.M.

Baes, C. F., & Mesmer, R. E. (1976). *The hydrolysis of cations*. New York: Wiley.

Baes, C. F., & Mesmer, R. E. (1981). The thermodynamics of cation hydrolysis. *American Journal of Science, 281*(7), 935-962.

Baumgartner, E., Blesa, M. A., & Maroto, A. J. G. (1982). Kinetics of the dissolution of magnetite in thioglycolic acid solutions. *Journal of Chemical Society, Dalton Transactions: Inorganic Chemistry, 9*, 1649-1654.

Bilkova, K., Hackerman, N., & Bartos, M. (2004). Inhibition effect of thioglycolic acid on carbon dioxide corrosion of carbon steel. *Corrosion, 60*(10), 965.

Bockris, J. O. M., Drazic, D., & Despic, A. R. (1961). The electrode kinetics of the deposition and dissolution of iron. *Electrochimica Acta, 4*(2-4), 325-361.

Borghi, E. B., Morando, P. J., & Blesa, M. A. (1991). Dissolution of magnetite by mercaptocarboxylic acids. *Langmuir, 7*(8), 1652-1659.

Bott, A. W. (1988). Electrochemistry of semiconductors. *Current Separations, 17*(3), 87-91.

Braun, R. D. (1991). Solubility of iron(II) carbonate at temperatures between 30 and 80[deg]. *Talanta, 38*(2), 205-211.

Cabrini, M., Hoxha, G., Kopliku, A., & Lazzari, L. (1998). *Prediction of $CO_2$ corrosion in oil and gas wells. Analysis of some case histories.* Paper presented at the NACE

Castle, J. E., & Mann, G. M. W. (1966). The mechanism of formation of a porous oxide film on steel. *Corrosion Science, 6*(6), 253-262.

Chan, E., John, D., Bailey, S., Kinsella, B., & Nesic, S. (2009). Formation of magnetite scale under anaerobic conditions at low temperatures. Paper presented at the Australasian Corrosion Association, Coffs Harbour.

Clegg, W. (1998). *Crystal structure determination*. Oxford: Oxford University Press.

Cornell, R. M., & Schwertmann, U. (1996). *The iron oxides - Structure, properties, reactions, occurence and uses*. Weinheim: VCH.

Crolet, J. L., Thevenot, N., & Nesic, S. (1998). Role of conductive corrosion products in the protectiveness of corrosion layers. *Corrosion, 54*(3), 194.

De Faria, D. L. A., Silva, S. V., & De Oliveira, M. T. (1997). Raman microspectroscopy of some iron oxides and oxyhydroxides. *Journal of Raman Spectroscopy, 28*(11), 873-878.

De Marco, R., Jiang, Z.-T., Pejcic, B., & Poinen, E. (2005). An in-situ synchrotron radiation grazing incidence X-Ray diffraction study of carbon dioxide corrosion. *Journal of the Electrochemical Society, 152*(10), B389-B392.

De Waard, C., & Milliams, D. E. (1975a). Carbonic acid corrosion of steel. *Corrosion, 31*(5), 177-181.

De Waard, C., & Milliams, D. E. (1975b). Prediction of Carbonic acid corrosion in natural gas pipelines. 506-510.

De Waard, C., Milliams, D. E., & Lotz, U. (1991). Predictive model for $CO_2$ corrosion engineering in wet natural gas pipelines. *Corrosion, 47*, 976-985.

Efird, K. D. (1988). Galvanic corrosion in oil and gas production. In H. P. Hack (Ed.), *STP 978 Galvanic corrosion* (pp. 260-282). Philadelphia: American Society for Testing and Materials.

Erdös, E., & Altorfer, H. (1976). Ein dem Malachit ähnliches basisches Eisenkarbonat als Korrosionsprodukt von Stahl. *Materials and Corrosion/Werkstoffe und Korrosion, 27*(5), 304-312.

Farshad, F. F., Garber, J. D., & Polaki, V. (2000). Comprehensive model for predicting corrosion rates in gas wells containing $CO_2$. *Society of Petroleum Engineers - Production and Facilities, 15*(3), 183-190.

Fitzgerald, B. (2008, 5 June). Gas plant blast has explosive impact on WA industry *The Age* [News].

Fushimi, K., Yamamuro, T., & Seo, M. (2002). Hydrogen generation from a single crystal magnetite coupled galvanically with a carbon steel in sulfate solution. *Corrosion Science, 44*(3), 611-623.

Gleeson, B., Hadavi, S. M. M., & Young, D. J. (2000). Isothermal transformation behavior of thermally-grown wustite. *Materials at High Temperatures, 17*(2), 311-319.

Gui, J., & Devine, T. M. (1991). Obtaining surface-enhanced Raman spectra from the passive film on iron. *Journal of the Electrochemical Society, 138*(5), 1376-1384.

Han, J., Yang, Y., Brown, B., & Nesic, S. (2008). Roles of passivation and galvanic effects in localized $CO_2$ corrosion of mild steel. In *NACE, Paper No. 08332*. New Orleans.

Haruyama, S., & Masamura, K. (1978). The dissolution of magnetite in acidic perchlorate solutions. *Corrosion Science, 18*(4), 263-274.

Harvey, P. H. (2005). *Corrosion tests and standards: Application and interpretation (2nd Edition): (MNL 20)*: ASTM International.

Hirnyi, S. I. (2001). Corrosion of iron in a carbonate-bicarbonate solution. Part 1. Crystallographic analysis of passive films. *Materials Science, 37*(1), 87-91.

John, D., Blom, A., Bailey, S., Nelson, A., Schulz, J., De Marco, R., et al. (2006). The application of neutron reflectometry and atomic force microscopy in the study of corrosion inhibitor films. *Physica B: Condensed Matter, 385-386*(Part 2), 924-926.

John, D., Kinsella, B., Bailey, S., & De Marco, R. (2003). *Evaluation of corrosion inhibitors using the jet impingement technique.* Paper presented at the Australasian Corrosion Association, Melbourne.

Jovanicevic, V., Ahn, Y. S., Dougherty, J., & Alink, B. (2000). *$CO_2$ corrosion inhibition by sulfur-containing organic compounds.* Paper presented at the NACE Paper No. 00007, Orlando.

Keddam, M., Mottos, O. R., & Takenouti, H. (1981a). Reaction model for iron dissolution studied by electrode impedance. I. Experimental results and reaction model. *Journal of the Electrochemical Society, 128*(2), 257-266.

Keddam, M., Mottos, O. R., & Takenouti, H. (1981b). Reaction model for iron dissolution studied by electrode impedance. II Determination of the reaction model. *Journal of the Electrochemical Society, 128*(2), 266-274.

Kittel, C. (2005). *Introduction to solid state physics* (8th ed.). Hoboken, N.J.: J. Wiley.

Kumai, C. S., & Devine, T. M. (2005). Oxidation of iron in 288°C, oxygen-containing water. *Corrosion, 61*(3), 201.

Lee, C. T., Odziemkowski, M. S., & Shoesmith, D. W. (2006). An in situ Raman-electrochemical investigation of carbon steel corrosion in $Na_2CO_3$/$NaHCO_3$, $Na_2SO_4$, and NaCl solutions. *Journal of the Electrochemical Society 153*(2), B33-B41.

Legodi, M. A., & de Waal, D. (2007). The preparation of magnetite, goethite, hematite and maghemite of pigment quality from mill scale iron waste. *Dyes and Pigments, 74*(1), 161-168.

Leussing, D. L., & Kolthoff, I. M. (1953). The Solubility Product of Ferrous Hydroxide and the Ionization of the Aquo-Ferrous Ion. *Journal of American Chemical Society, 75*(10), 2476–2479.

López, D. A., Pérez, T., & Simison, S. N. (2003). The influence of microstructure and chemical composition of carbon and low alloy steels in $CO_2$ corrosion. A state-of-the-art appraisal. *Materials & Design, 24*(8), 561-575.

López, D. A., Schreiner, W. H., De Sánchez, S. R., & Simison, S. N. (2004). The influence of inhibitors molecular structure and steel microstructure on corrosion layers in $CO_2$ corrosion: An XPS and SEM characterization. *Applied Surface Science, 236*(1-4), 77-97.

Macdonald, J. R. (1987). *Impedance spectroscopy : emphasizing solid materials and systems*. New York: Wiley.

McHardy, J., & Ludwig, F. (2002). *Electrochemistry of Semiconductors and Electronics - Processes and Devices*: William Andrew Publishing/Noyes.

Misawa, T., Hashimoto, K., Suëtaka, W., & Shimodaira, S. (1973). Formation of Fe(II)-Fe(III) green complex on oxidation of ferrous ion in perchloric acid solution. *Journal of Inorganic and Nuclear Chemistry, 35*(12), 4159-4166.

Moiseeva, L. S. (2005). Carbon dioxide corrosion of oil and gas field equipment. *Protection of Metals, 41*(1), 76-83.

Mora-Mendoza, J. L., & Turgoose, S. (2002). $Fe_3C$ influence on the corrosion rate of mild steel in aqueous $CO_2$ systems under turbulent flow conditions. *Corrosion Science, 44*(6), 1223-1246.

Nesic, S., & Lee, K.-L. J. (2003). A mechanistic model for carbon dioxide corrosion of mild steel in the presence of protective iron carbonate films - Part 3: Film growth model. *Corrosion, 59*(7), 616-628.

Nesic, S., Nordsveen, M., Nyborg, R., & Stangeland, A. (2003). A mechanistic model for carbon dioxide corrosion of mild steel in the presence of protective iron carbonate films - Part 2: A numerical experiment. *Corrosion, 59*(6), 489-497.

Odziemkowski, M., Flis, J., & Irish, D. E. (1994). Raman spectral and electrochemical studies of surface film formation on iron and its alloys with carbon in $Na_2CO_3/NaHCO_3$ solution with reference to stress corrosion cracking. *Electrochimica Acta, 39*(14), 2225-2236.

Oldfield, J. W. (1988). Electrochemical theory of galvanic corrosion. In H. P. Hack (Ed.), *STP 978 Galvanic corrosion* (pp. 5-22). Philadelphia: American Society for Testing and Materials.

Pandey, R. K., Sahu, S. N., & Chandra, S. (1996). *Handbook of semiconductor electrodeposition*. New York: Marcel Dekker.

Pekov, I. V., Perchiazzi, N., Merlino, S., Kalachev, V. N., Merlini, M., & Zadov, A. E. (2007). Chukanovite, $Fe_2(CO_3)(OH)_2$, a new mineral from the weathered iron meteorite Dronino. *Eur J Mineral, 19*(6), 891-898.

Peulon, S., Antony, H., Legrand, L., & Chausse, A. (2004). Thin layers of iron corrosion products electrochemically deposited on inert substrates: synthesis and behaviour. *Electrochimica Acta, 49*(17-18), 2891-2899.

Ramachandran, S., & Jovancicevic, V. (1999a). Molecular modeling of the inhibition of mild steel carbon dioxide corrosion by imidazolines. *Corrosion, 55*(3), 259-267.

Ramachandran, S., & Jovancicevic, V. (1999b). *Understanding interactions between corrosion inhibitors and iron carbonate films using molecular modeling*. Paper presented at the NACE, San Antonio.

Ramachandran, S., Jovancicevic, V., & Ward, M. B. *Understanding corrosion inhibition of iron carbonate films through molecular modeling*. Retrieved 20/6/08, from http://www.daycreative.com/trade/molecularmodel.htm

Ramachandran, S., Tsai, B. L., Blanco, M., Chen, H., Tang, Y., & Goddard, W. A. (1996). Self-assembled monolayer mechanism for corrosion inhibition of iron by imidazolines. *Langmuir, 12*(26), 6419-6428.

Ramachandran, S., Tsai, B. L., Blanco, M., Chen, H., Tang, Y., & Goddard, W. A. (1997). Atomistic simulations of oleic imidazolines bound to ferric clusters. *The Journal of Physical Chemistry A, 101*(1), 83-89.

Ray, L. F. (2006). A Raman spectroscopic study of selected minerals of the rosasite group. *Journal of Raman Spectroscopy, 37*(9), 910-921.

Rosenberg, H. M. (1988). *The solid state : an introduction to the physics of solids for students of physics, materials science, and engineering* (3rd ed.). Oxford ; New York: Oxford University Press.

Schoonen, M. A. A., Xu, Y. (2000). The abosulute energy positions of conduction and valence bands of selected semiconducting minerals. *American Mineralogist, 85*, 543-556.

Schwertmann, U., & Cornell, R. M. (1991). *Iron oxides in the laboratory: preparation and characterization*. Weinheim: VCH.

Simard, S., Odziemkowski, M., Irish, D. E., Brossard, L., & Ménard, H. (2001). In situ micro-Raman spectroscopy to investigate pitting corrosion product of 1024 mild steel in phosphate and bicarbonate solutions containing chloride and sulfate ions *Journal of Applied Electrochemistry, 31*(8), 913-920.

Simpson, L. J., & Melendres, C. A. (1996). Surface-enhanced Raman spectroelectrochemical studies of corrosion films on iron in aqueous carbonate solution. *Journal of the Electrochemical Society, 143*(7), 2146-2152.

Sweeton, F. H., & Baes, C. F. (1970). The solubility of magnetite and hydrolysis of ferrous ion in aqueous solutions at elevated temperatures. *The Journal of Chemical Thermodynamics, 2*(4), 479-500.

Thanos, I. C. G. (1986). In situ Raman and other studies of electrochemically oxidized iron and iron-9% chromium alloy. *Electrochimica Acta, 31*(7), 811-820.

Tremaine, P. R., Masscow, R. V., & Shierman, G. R. (1977). A calculation of gibbs free energies for ferrous ions and the solubility of magnetite in $H_2O$ and $D_2O$ to 300°C. *Thermochimica Acta, 19*(3), 287-300.

Turgoose, S., & Cottis, R. (1993). The impedance response of film-covered metals. In J. R. Scully, D. C. Silverman & M. W. Kendig (Eds.), *Electrochemical impedance: Analysis and interpretation* (pp. 173-191). Philadelphia: American Society for Testing and Materials.

Veder, J. P., Nafady, A., Clarke, G., Williams, R. P., De-Marco, R., & Bond, A. M. (2010). A versatile flow cell for in situ grazing incidence X-ray diffraction studies of electrocrystallised materials. *Electrochimica Acta, Submitted*.

Videm, K., & Dugstad, A. (1989). Corrosion of carbon steel in aqueous carbon dioxide environment. Part 2: Film formation. *Materials Performance, 28*(4), 46-50.

Weir, M. (2002, 18 Aug). Rust problem in Shelf platform. *The West Australian* [News].

Weller, M. T. (1994). *Inorganic materials chemistry*. Oxford: Oxford University Press.

Wenzel, M. J., & Steinle-Neumann, G. (2007). Nonequivalence of the octahedral sites of cubic $Fe_3O_4$ magnetite. *Physical Review B: Condensed Matter and Materials Physics 75*(21).

Wielant, J., Goossens, V., Hausbrand, R., & Terryn, H. (2007). Electronic properties of thermally formed thin iron oxide films. *Electrochimica Acta, 52*(27), 7617-7625.

Wilhelm, S. M. (1988). Galvanic corrosion caused by corrosion products. In H. P. Hack (Ed.), *STP 978 Galvanic corrosion* (pp. 23-34). Philadelphia: American Society for Testing and Materials.

Wu, N. L., Hwang, J. Y., Liu, P. Y., Han, C. Y., Kuo, S. L., Laio, K. H., et al. (2001). Synthesis and characterization of Sb-doped $SnO_2$ xerogel electrochemical capacitor. *Journal of the Electrochemical Society, 148*(6), A550-A553.

Yang, Y., Brown, B., & Nesic, S. (2008). *Application of EQCM to the study of $CO_2$ corrosion.* Paper presented at the 17th International Corrosion Congress, Paper No 4071, Las Vegas, NV.

Zhang, X. G. (2000). *Uhlig's Corrosion Handbook* (Second ed.). Ontario: John Wiley & Sons.